GEORGIA DOT RESEARCH PROJECT 16-34

FINAL REPORT

Bird-Long Island Management Study Phase 1B: Hydrodynamic Characterizations for Bird/Long Island

Georgia Department of Transportation

OFFICE OF PERFORMANCE-BASED MANAGEMENT AND RESEARCH

15 KENNEDY DRIVE
FOREST PARK, GA 30297-2534

TECHNICAL REPORT STANDARD TITLE PAGE

1.Report No.: FHWA-GA-19-1634	2. Government Accession No.:	3. Recipient's Catalog No.:
4. Title and Subtitle: Bird-Long Island Management Study Phase 1B: Hydrodynamic Characterizations for Bird/Long Island	5. Report Date: March 2019 6. Performing Organization Code:	
7. Author(s): Kevin A. Haas; Alexandra C. Muscalus	8. Performing Organ. Report No.: 16-34	
9. Performing Organization Name and Address: Georgia Institute of Technology 790 Atlantic Drive Atlanta, GA 31411	10. Work Unit No.: 11. Contract or Grant No.: PI# 0015304	
12. Sponsoring Agency Name and Address: Georgia Department of Transportation Office of Research 15 Kennedy Drive Forest Park, GA 30332-0355	13. Type of Report and Period Covered: Final: December 2016 – March 2019 14. Sponsoring Agency Code:	
15. Supplementary Notes: Prepared in cooperation with the U.S. Department of Transportation, Federal Highway Administration.		

16. Abstract:
Bird-Long Island, located between two channels in the Savannah River, contains cultural resources that are threatened by erosion. This study characterizes the hydrodynamics in the vicinity of the island with field measurements including velocity profiles of the river, long-term current wave profiling measured with Aquadopp current profilers, and short-term water level time series. Numerical simulations are performed using the Coupled-Ocean-Atmosphere-Wave-Sediment Transport (COAWST) model system for the Savannah estuary. The Aquadopp deployments record waves and currents in the Main Channel, the larger and deeper shipping channel north of the island, and the South Channel, the shallower channel south of the island. All data show a significant and consistent response to large vessel traffic. Measured vessel wake reaches up to 2.01 m height in the Main Channel and 0.32 m height in the South Channel. Wake propagates into the South Channel from both ends of the island such that the southwestern shore of Bird-Long Island is impacted by similar waves twice for each vessel passage. An energy contribution analysis is performed to estimate the relative significance to potential shoreline impacts of tidal currents, wind waves, and mid-band frequencies. A water level threshold is applied to isolate energy contributions to periods of time when the eroding scarp is vulnerable to hydrodynamic processes. At the Main Channel site, the percentage energy contributions of tidal currents, wind waves, and mid-band frequencies are 6%, 26%, and 68%, respectively. At the South Channel site, the percentage energy contributions of tidal currents, wind waves, and mid-band frequencies are 38%, < 1%, and 61%, respectively. The mid-band energy is mainly produced by large vessel wake and the seiching it induces. Thus, large vessels are the main source of energy; however, tidal currents have a significant role in the South Channel, and wind waves have a role in the Main Channel.

17. Key Words: Bird-Long Island; hydrodynamic characterization; tidal currents; wind waves; ship wake		18. Distribution Statement:	
19. Security Classification (of this report): Unclassified	20.Security classification (of this page): Unclassified	21. Number of Pages: 98	22. Price:

Form DOT 1700.7 (8-69)

GDOT Research Project No. 16-34

Final Report

BIRD-LONG ISLAND MANAGEMENT STUDY PHASE 1B: HYDRODYNAMIC CHARACTERIZATIONS FOR BIRD/LONG ISLAND

By

Dr. Kevin A. Haas
Associate Professor

Alexandra C. Muscalus
Graduate Research Assistant

Georgia Institute of Technology
Civil and Environmental Engineering

Contract with

Georgia Department of Transportation

In cooperation with

U.S. Department of Transportation Federal Highway Administration

February 2019

TABLE OF CONTENTS

LIST OF TABLES

Table Page

LIST OF FIGURES

Figure Page

EXECUTIVE SUMMARY

Bird-Long Island in the Savannah River provides valuable natural and cultural resources which are threatened by erosion. This study characterizes the hydrodynamics in the vicinity of the eroding shorelines through the collection and analysis of multiple sets of field measurements including twenty-six velocity profiles of the river obtained with a boat-mounted acoustic Doppler current profiler, six long-term current profiling and wave burst time series obtained with three Aquadopps, and twelve short-term water level time series obtained with arrays of three pressure transducers. Numerical simulations are performed using the Coupled-Ocean-Atmosphere-Wave-Sediment Transport (COAWST) model system for the full Savannah estuary. Tidal currents, tidal water level, and wind waves in the model output generally agree well with field measurements.

For each of long-term Aquadopp deployment, waves and currents are measured in the Main Channel, the larger and deeper channel north of the island which contains the shipping channel, and the South Channel, the shallower channel south of the island. All Aquadopp data sets show a significant and consistent response to large vessel traffic. Measured vessel wake reaches as high as 2.01 m height in the Main Channel and 0.32 m height in the South Channel. Wake in the South Channel propagates from both ends of the islands such that the South Channel shore of Bird-Long Island is impacted by two waves for each vessel passage; the waves are of similar height and peak energy flux.

An energy contribution analysis is performed using the Aquadopp data in the Main and South Channels to estimate the relative significance to potential shoreline impacts of tidal currents, wind waves, and mid-band frequencies. The eroding scarp along the Main Channel site is above the mean water level, so a water level threshold is

applied to isolate energy contributions to periods of time when the scarp is vulnerable to hydrodynamic processes. At the Main Channel site, the percentage energy contributions with potential scarp impacts of tidal currents, wind waves, and mid-band frequencies are 6%, 26%, and 68%, respectively. The eroding scarp at the South Channel site is continuously exposed to hydrodynamic processes, so no threshold is applied. At the South Channel site, the percentage energy contributions of tidal currents, wind waves, and mid-band frequencies are 38%, < 1%, and 61%, respectively. The energy in the mid-band frequencies is primarily produced by large vessel wake and the seiching that it induces in both the Main and South Channels. Therefore, large vessels are the primary source of energy generated; however, tidal currents have a significant role in the South Channel, and wind waves have a role in the Main Channel.

ACKNOWLEDGMENTS

The authors acknowledge Skidaway Institute small boat operators for their assistance with the field data collection of this project. Andy Udell and Blake Baklini with Georgia Tech CEE Facilities are also acknowledged for their assistance with preparing field equipment.

1. INTRODUCTION

Bird-Long Island is a dredge-spoil island located between the north and south channels near the inlet of the Savannah River at the border of Georgia and South Carolina, as shown in Figure 1. The island is in a tidally dominant environment and contains cultural and natural resources, including remnants of Battery Hamilton, a Civil War era artillery battery. As a wetland mitigation bank, it is particularly important to the state of Georgia. However, these resources are under threat from documented and ongoing sea level rise, shoreline change (i.e., erosion and accretion) from natural and anthropogenic causes, and land subsidence. In addition to substantial tidal and freshwater flows, the island is subject to locally-generated wind waves primarily from northeast winds, as well as wake from the large vessels, including container ships and tankers, transiting to and from the Port of Savannah.

A previous study examined the effects of wind and vessel-generated waves on shoreline retreat for the Fort Pulaski National Monument on nearby Cockspur Island (Houser 2010). The study concluded that while the vessel-generated waves account for nearly 25% of the energy, the wind waves during storm events with increased water levels accounted for the majority of the marsh retreat. Although the proximity of this previous study site to Bird-Long Island is relevant, the different orientations of the islands and the narrowing of the channel create a different hydrodynamic environment.

The present study uses field data to characterize the hydrodynamic processes affecting Bird-Long Island and inform a numerical hydrodynamic model of the waves and currents of the region.

The major objectives of this project are articulated as follows:

Objective (1) This study aims to deploy three velocity profilers to measure the waves and currents. Two will be in the Main Channel offshore of Bird and Long Island, whereas the third instrument will be deployed in the South Channel. The instruments will be deployed for two separate one month long deployments. These data will be supplemented with additional measurements of the cross-channel spatial structure of the currents using a boat-based velocity profiler.

Objective (2) The numerical model simulations will be performed using the COAWST model system which consists of the wave model Simulating Waves Nearshore (SWAN) and the ocean circulation model Regional Ocean Modeling System (ROMS). The objective will be to model the full Savannah estuary with a coarse regional grid in conjunction with a nested high resolution grid surrounding the project site with updated bathymetric data. In addition, SWAN simulations will be incorporated and coupled to the circulation model to simulate the wave driven forces directly impacting the project site.

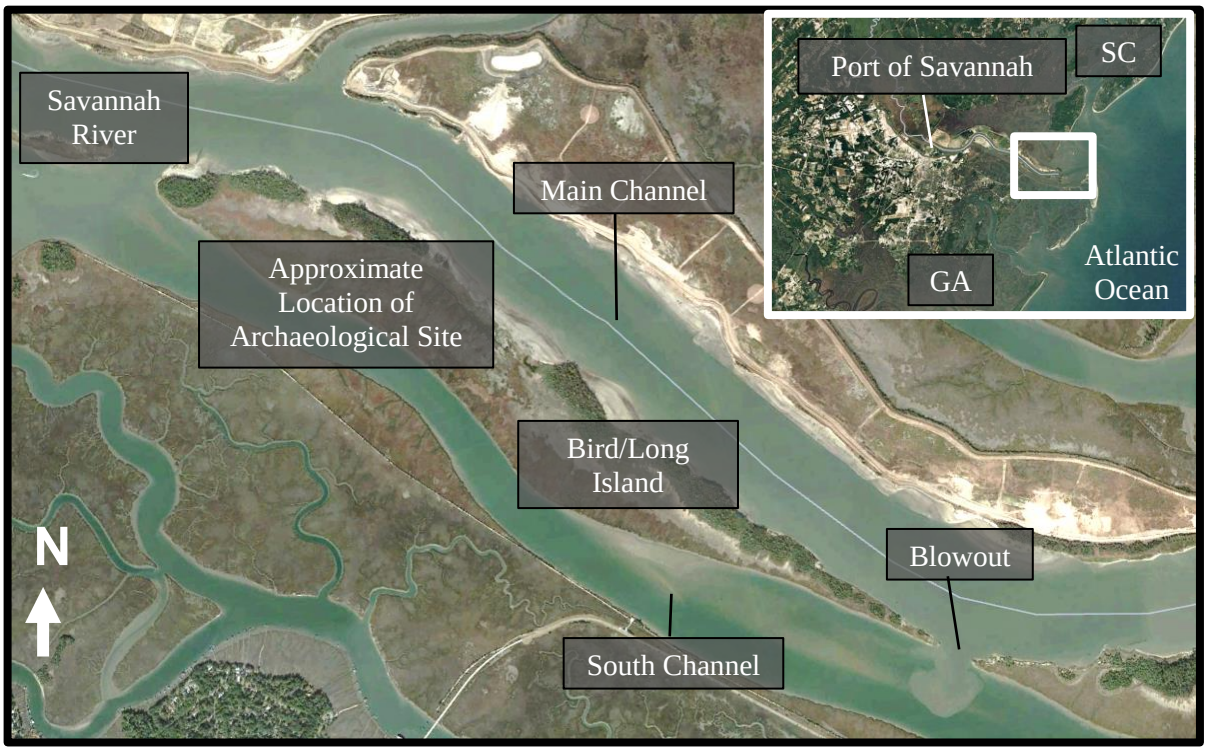

Figure 1: Map of Bird-Long Island, located between the Main Channel and South Channel of the Savannah River, GA**.**

2. METHODS

2.1 Overview of Field Data Collection:

Data was collected over five separate trips to the site spanning March 2017 to November 2017. Month-long velocity profiler deployments took place during the months of March and October, with additional short-term data collection primarily taking place during the trips arranged for the deployment and recovery of the profilers. Hereafter, the March and October long-term deployments are referred to as the "spring" and "fall" deployments, respectively.

Three Aquadopp velocity profilers were deployed for two separate month-long periods, providing current profile data every ten minutes. Two of these instruments also recorded waves in bursts of high frequency data collection. The three deployment sites – Main Channel East, Main Channel West, and South Channel, are labeled in Figure 2. Their coordinates are listed in Table 1. During both deployments, an instrument was placed at each of these three sites.

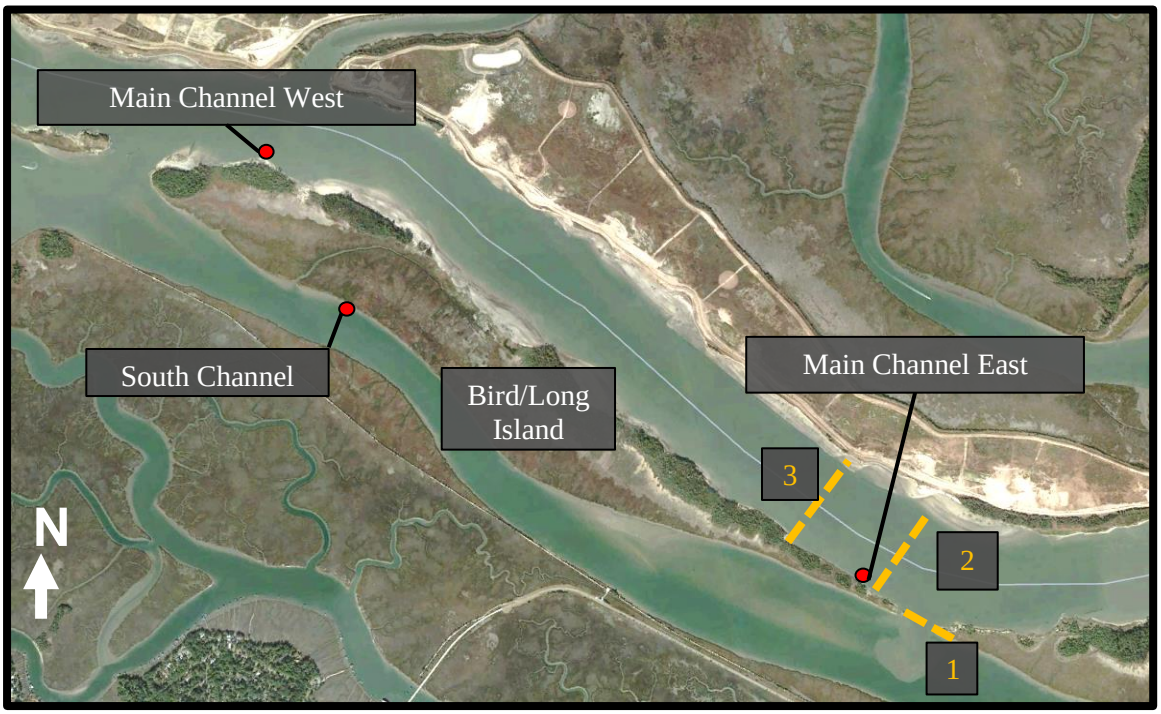

Figure 2: Map of instrument deployment locations with red filled circles indicating the locations of Aquadopp and pressure transducer sites and orange dashed lines indicating the locations of the boat-mounted acoustic Doppler current profiler (ADCP) transects.

Table 1: GPS Coordinates of the Deployment Sites

Site	GPS Coordinates
Main Channel East	32.03991 N, 80.92841 W
Main Channel West	32.06987 N, 80.96413 W
South Channel	32.05957 N, 80.95943 W

A boat-mounted acoustic Doppler current profiler was used to collect 26 current profiles distributed over three transects, shown in Figure 2. These transects captured the spatial distribution of the across-channel and along-channel current velocity over a duration of 4 hours.

Three pressure transducers collected pressure data at 3-second logging intervals during three separate deployments ranging from 23 to 48 hours in length. These instruments were placed just shoreward of the three Aquadopp deployment locations.

A GoPro camera was placed facing the Main Channel during the three PT deployments to

capture images of the Main Channel ship traffic at preprogrammed 5 or 30 second intervals.

Bathymetric surveys were conducted to collect bathymetric data in the vicinity of the three deployment sites. The regions surveyed are indicated by bathymetric data points in Figure 3.

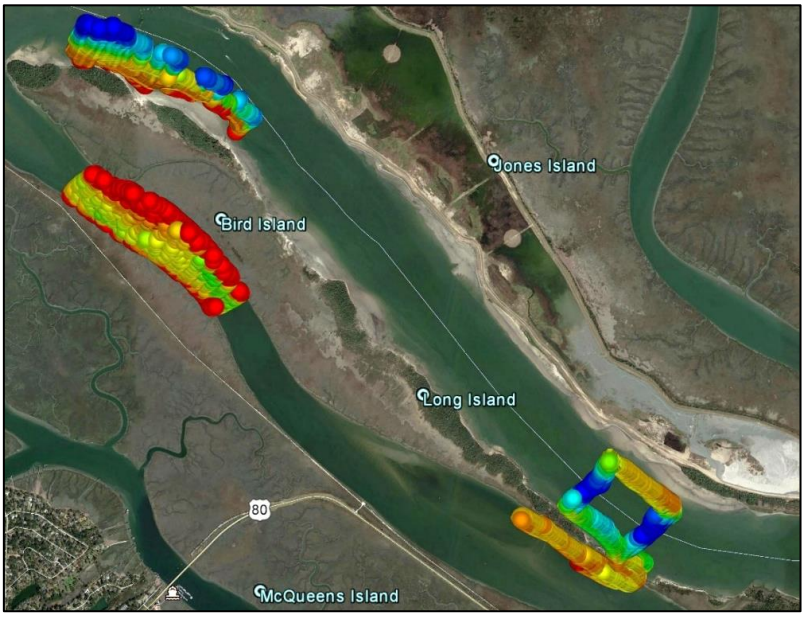

Figure 3: Regions where bathymetric surveying was conducted.

2.1.1 Deployment Sites

The Main Channel East site, shown in Figure 4, has a narrow alongshore strip of deep, soft mud bordered shoreward by dense marsh grass. The Main Channel West site, shown in Figure 5, is characterized shoreward by a dense line of trees with a wall of vegetation debris, primarily downed trees. A sandy beach is interspersed with rocky patches transitions into a muddy bottom with small oyster reefs. The South Channel site, shown in Figure 6, is dominated by mud and marsh grass. It is generally sheltered from large waves by the island.

Figure 4: Main Channel East deployment site.

Figure 5: Main Channel West deployment site.

Figure 6: South Channel deployment site.

2.1.2 Boats

Three boats were used throughout the field data collection. The RV Sandpiper, a 20’ Carolina skiff chartered from Skidaway Institute of Oceanography was used primarily for Aquadopp deployment and recovery. The 16’ Zodiac, owned by Georgia Tech, was used for surveying, camera deployment, and pressure transducer deployment. Lastly, a 24’ pontoon, also belonging to Georgia Tech, was used for ADCP measurements, Aquadopp recovery, and surveying. The three boats are shown in Figure 7.

Figure 7: Boats used throughout field data collections activities: (upper left) the RV Sandpiper, (upper right) the Zodiac, and (lower) the pontoon**.**

2.1.3 Chronological Summary

Table 2 chronologically summarizes the data collection throughout the five field trips.

Table 2: Chronological Summary of Field Data Collection

Trip	Date	Boat	Description
1	3/22	RV Sandpiper	Reconnaissance and site selection AQD 9331 deployed at South Channel
	3/22	RV Sandpiper	AQD 6204 deployed at Main Channel West AQD 2015 deployed at Main Channel East
2	5/8	Pontoon	AQD 2015 recovered from Main Channel East AQD 6204 picked up from marina
	5/9	Pontoon	Surveying in eastern South Channel and at ADCP transects Boat-mounted ADCP measurements in Main Channel AQD 9331 recovered from South Channel
3	8/26	Zodiac	Camera deployed at Main Channel East Pressure transducers (PTs) deployed at all sites
	8/27	Zodiac	Camera recovered from Main Channel East PTs recovered from all sites
4	10/6	RV Sandpiper	Camera deployed at Main Channel West PT and AQD 9331 deployed at South Channel PT and AQD 2015 deployed at Main Channel West PT and AQD 6204 deployed at Main Channel East
	10/7	Zodiac	Surveying in South Channel near archaeological site PTs recovered for data download and redeployed at all sites
	10/8	Zodiac	Camera recovered from Main Channel West PTs recovered from all sites
5	11/3	RV Sandpiper	AQD 9331 recovered from South Channel PT deployed at South Channel AQD 6204 recovered from Main Channel East PT deployed at Main Channel East AQD 2015 recovered from Main Channel West PT deployed at Main Channel West
	11/4	Zodiac	Surveying in Main Channel PTs recovered for data download and redeployed at all sites
	11/5	Zodiac	PTs recovered from all sites

2.2 Deployment and Data Details by Instrument

2.2.1 Aquadopp

Three sidelooking Nortek Aquadopp Current Profilers, “Aquadopps”, were used in month-long deployments. They are furthered described in Table 3 in which they are referenced by their Serial Numbers (SN): AQD 6204, AQD 2015, and AQD 9331. These instruments, shown in Figure 8, use acoustic Doppler technology to measure the three-dimensional current velocity. The current is averaged in each of multiple preprogrammed cells which span the vertical extent of the water column above the instrument’s blanking distance. This provides a vertical profile of the velocity with a resolution corresponding to the number and width of the cells, as shown in Figure 8. In addition to an internal solid-state recorder and battery, the Aquadopps contain temperature, pressure, and tilt sensors, and a compass.

Burst mode requires more memory and battery capacity, which was supported by AQD 2015 and AQD 9331, but not AQD 6204. Thus, waves were measured with AQD 2015 and AQD 9331. AQD 6204 was programmed to record profiles are higher frequency than the other Aquadopps. The spring and fall Aquadopp deployment configurations are provided in Table 2.

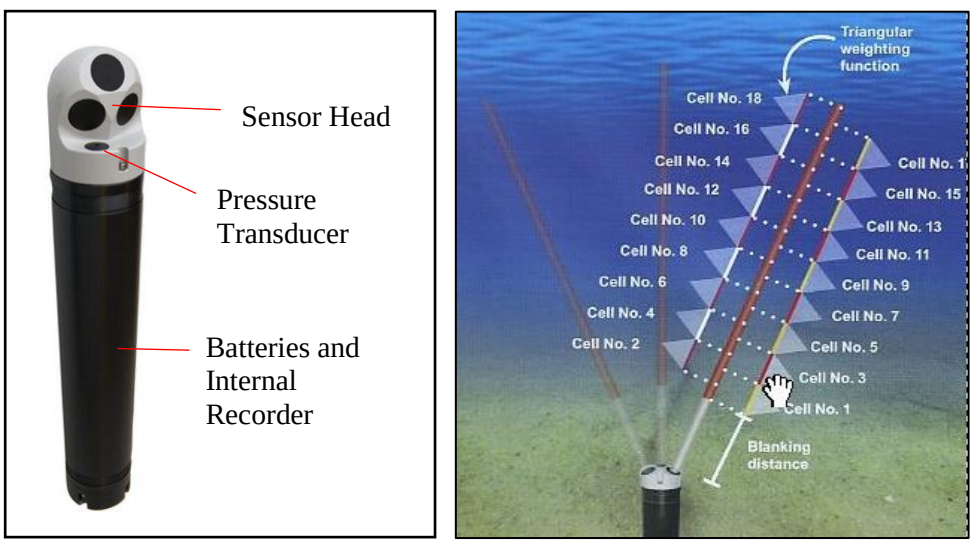

Figure 8: (Left) Nortek Aquadopp Current Profiler and (right) illustration of sound beams and current profiling cells (images adapted from nortekgroup.com).

Table 3: Aquadopp Hardware and Deployment Parameters for Each Deployment

Parameter	AQD 6204	AQD 2015	AQD 9331
Instrument Information			
Instrument Owner/Source	Blanton, UGA	Haas, GT	Edwards, UGA
Recorder Size	9 MB	89 MB	361 MB
Firmware Version	3.32	1.15	3.39
Hardware Revision	3(D)	60	4 (E)
Acoustic Frequency	2 MHz	2 MHz	2 MHz
Blanking Distance	0.20 m	0.20 m	0.20 m
Spring Deployment Settings			
Deployment Site	Main Channel West	Main Channel East	South Channel
Wave Burst Sampling Rate	Waves Disabled	2 Hz	2 Hz
Wave Burst Interval	Waves Disabled	1800 sec	1800 sec
Wave Burst Number of Samples	Waves Disabled	1024	1024
Wave Cell Size	Waves Disabled	1.00 m	1.00 m
Velocity Profiling Interval	300 sec	600 sec	600 sec
Velocity Profiling Duration	60 sec	60 sec	60 sec
Velocity Profiling Cell Size	0.20 m	0.20 m	0.20 m
Number of Cells	25	25	25
Mean Depth At Deployment (mean of first 48 hours)	2.39 m	2.08 m	2.55 m
First Good Burst	Mar-23 12:00	Mar-23 12:00	Mar-22 12:00
Last Good Burst	Apr-15 14:05	May-8 17:55	May-9 16:00
Fall Deployment Settings			
Deployment Site	Main Channel East	Main Channel West	South Channel
Wave Burst Sampling Rate	Waves Disabled	1 Hz	1 Hz
Wave Burst Interval	Waves Disabled	1200 sec	1200 sec
Wave Burst Number of Samples	Waves Disabled	1024	1024
Wave Cell Size	Waves Disabled	0.90 m	0.90 m
Velocity Profiling Interval	300 s	600 s	600 s
Velocity Profiling Duration	60 s	60 s	60 s
Velocity Profiling Cell Size	0.20 m	0.25 m	0.25 m
Number of Cells	25	20	20
Mean Depth At Deployment (mean of first 48 hours)	3.76 m	3.30 m	2.33 m
First Good Burst	Oct-6 16:00	Oct-6 14:00	Oct-6 14:09
Last Good Burst	Nov-3 12:10	Oct-28 12:33	Nov-3 11:00

The Aquadopps were deployed in aluminum frames weighted with lead, as shown in Figure 9. Small lead blocks were attached to the frame itself, while a chain attached the frame to a larger anchor block of lead. The anchor was also attached to a line with a marker buoy. Less weight was attached to the frame deployed in the South Channel owing to the sheltered conditions. For the spring deployment, the South Channel assembly was approximately 50 lbs, and the two Main Channel assemblies were approximately 60 lbs. Due to movement of the assemblies in the Main Channel during the spring deployment, weight was added for the second deployment. The South Channel assembly was increased to approximately 60 lbs with a doubling of the anchor weight, and the Main Channel assemblies were increased to approximately 100 lbs with additional of lead blocks on the aluminum frames and a doubling of the anchor weights.

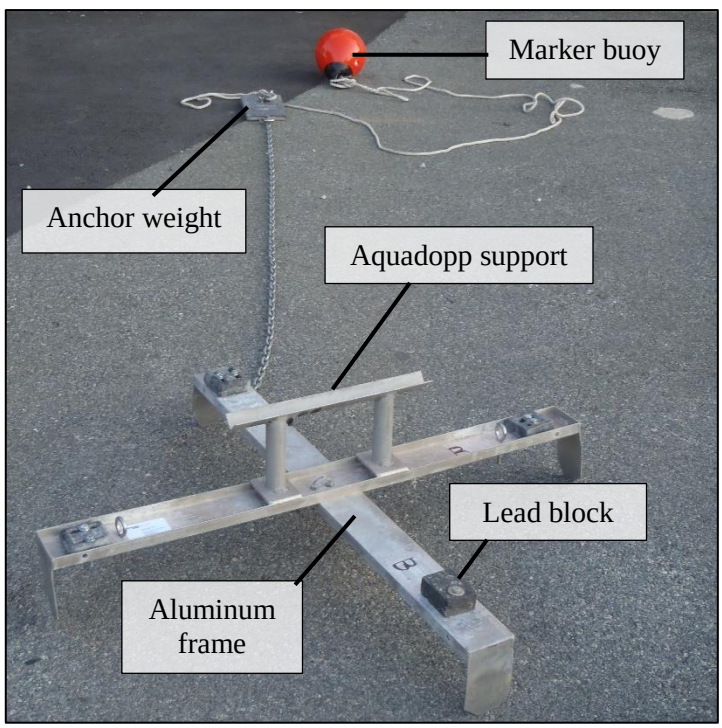

Figure 9: Aquadopp frame assembly used in the spring deployment.

After recovery, raw data was downloaded from the Aquadopps using 1.125 Nortek AquaPro v1.125 software and converted into ASCII files with Nortek Aquadopp v1.40.16. Data processing was conducted in MATLAB. Quality control was performed on the velocity profile

data by eliminating data for cells within 0.20 m of the surface and/or for beam amplitudes less than 50, which indicates a weak return acoustic signal. A low pass filter with a 33 hour cutoff was also applied to the water level data to obtain the de-tided conditions. Tidal constituents were computed by performing harmonic analysis with the MATLAB function *T_Tide* (Pawlowicz et al., 2002) on the time series of water level and depth-averaged velocities. The processed data contents are listed in Table 4.

Table 4: Processed Aquadopp Data Contents

Profile/Position Data	
a1	time series of beam 1 amplitude for each cell
a2	time series of beam 2 amplitude for each cell
a3	time series of beam 3 amplitude for each cell
cellz	vertical coordinate of each cell
he	time series of heading
pit	time series of pitch
ro	time series of roll
t	time of profile measurements
Te	time series of temperature
Ve	time series of east velocity for each cell
Vebar	time series of depth-averaged east velocity
vmag	time series of velocity magnitude
Vn	time series of north velocity for each cell
Vnbar	time series of depth-averaged north velocity
Vu	time series of upward velocity for each cell
z	time series of water surface elevation
zlp	time series of water surface elevation with low pass filter
Burst Data	
tburst	mean time of burst measurements
uburst	time series of u velocity during burst
vburst	time series of v velocity during burst
zburst	time series of water surface elevation during burst
Constituent Data	
fu	frequency of velocity constituents
fz	frequency of water level constituents
tcon	names of tidal constituents
tidecon	water level tidal constituents
tideconu	velocity tidal constituents

2.2.2 Acoustic Doppler Current Profiler

A Teledyne RD Instruments (TDRI) Workhorse Monitor Acoustic Doppler Current

Profiler (ADCP) was mounted to a boat which navigated three transects, labeled in Figure 2, to provide velocity profiles for cross-sections in the river. Much like the Aquadopps, the boat-mounted ADCP uses the reflection of emitted sound beams to measure three-dimensional velocity profiles. While the boat moves steadily across a transect, the instrument averages velocities spatially over cells of preprogrammed sizes at a frequency of 1200 kHz. The ADCP is also equipped with an internal compass and has bottom-tracking capability. It was programmed with the WinRiver II software distributed by Teledyne RDI. During data collection, the instrument was powered by an external battery connected with a cable. It recorded data to a laptop running WinRiver II, which was also connected via cable. The laptop was also synced to a GPS system to improve data quality for the boat position and heading, as well as the bottom-tracked velocity.

The instrument was secured in an aluminum frame mounted to a wooden instrument mount, which also supported a transducer frame. The ADCP frame was lowered into the water off the bow of the pontoon boat and clamped to the edge of the moon pool, as shown in Figure 10. The external battery was secured with loading straps near the bow of the boat, and laptop recording data with WinRiver II was located near the center of the boat.

Raw profile data was recorded in WinRiver II during collection and later exported into ASCII format using this same software. The velocity recorded in a coordinate system relative to the ADCP itself was used in further data processing, all of which was performed in MATLAB. Data from two GPS antennas placed on the roof of the boat were used to calculate the motion of the ADCP instrument. The actual current velocity was calculated by removing the instrument velocity, as measured by the GPS, from the total velocity recorded by the ADCP. The current velocity was rotated into an along-transect and across-transect components for each of the three transects. Lastly, the velocities were passed through a median filter to reduce instrument noise. The processed data are listed in Table 5.

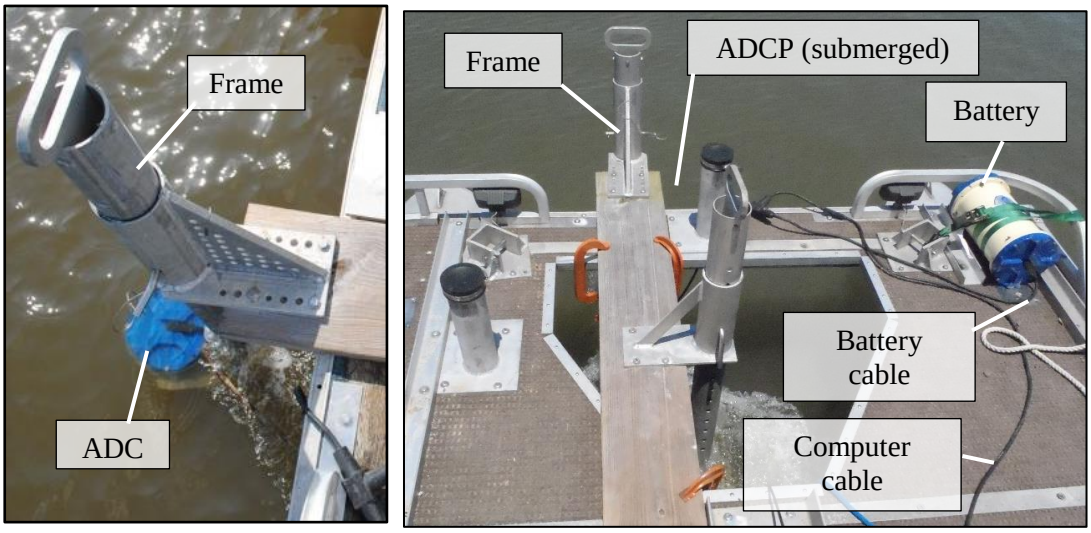

Figure 10: Images of (left) the ADCP secured in the frame and (right) the full ADCP assembly clamped to the edge of the Pontoon moonpool.

Table 5: Descriptions of Processed ADCP Data

Variable	Description
tranID	transect number for each velocity profile
Tcoord	transect coordinates along each transect
htran	depth profile of each transect
trantime	mean time of profile data collection
UtranIF	interpolated and filtered cross-transect velocity
VtranIF	interpolated and filtered along-transect velocity
ztran	vertical coordinate of the interpolated velocity

2.2.3 Pressure Transducers

Three ONSET HOBO Titanium Water Level Loggers were submerged near the Aquadopp deployment locations for three separate deployments of 1 to 2 days. These pressure transducers (PTs), shown in Figure 11, contain a pressure sensor, internal battery, internal data storage, and optical port was used for programming and data transfer. Each pressure transducer was programmed with ONSET HOBOware to record pressure readings at 3 second intervals. At this frequency, the internal memory was sufficient to record data for approximately 24 hours, so halfway through each deployment, the instrument was retrieved to download data to a laptop and erase the internal recorder; the data from these interrupted deployments are concatenated. The times of initial and last recordings, as well as the durations of the pressure transducer deployments, are given in Table 6. The November deployment of the pressure transducer at the South Channel is shorter than the others due to instrument failure of the first day of deployment.

Figure 11: ONSET Hobo Water Level Logger (adapted from onsetcomp.com).

Table 6: Pressure Transducer Recording Start and End Times and Durations

Month	Site	Time of First Good Record	Time of Last Good Record	Duration (hrs)
August	Main Channel East	Aug-26 08:03:03	Aug-27 11:11:39	27
	Main Channel West	Aug-26 09:19:03	Aug-27 11:36:12	26
	South Channel	Aug-26 08:43:12	Aug-27 11:28:00	27
October	Main Channel East	Oct-06 14:46:57	Oct-08 12:46:33	46
	Main Channel West	Oct-06 13:39:15	Oct-08 12:12:42	47
	South Channel	Oct-06 13:04:15	Oct-08 12:24:21	47
November	Main Channel East	Nov-03 12:48:57	Nov-05 13:18:57	48
	Main Channel West	Nov-03 13:21:27	Nov-05 12:48:44	47
	South Channel	Nov-04 13:24:43	Nov-05 12:40:22	23

The pressure transducers were mounted to a small, heavy frame consisting of aluminum channel bolted to two large lead blocks. The instruments were housed in a PVC casing, which was attached to the channel using multiple plastic zip ties. A line with a marker buoy was attached to the frame to aid recovery. The frame assembly is shown in Figure 12.

After recovery, the pressure data was downloaded with HOBOware Pro v.3.7.12 software. The data were imported into MATLAB, and water level fluctuations were calculated from the pressure variation. For the October and November deployments, both data sets were concatenated and treated as one deployment with a short time discontinuity.

Figure 12: Pressure Transducer in PVC casing and secured to a weighted frame.

2.2.4 Mounted Camera

A GoPro Hero2 camera was used during the three pressure transducer deployments to regularly record images of the shipping channel. In the first of the three deployments, the camera was mounted to a tree near the Main Channel East site with loading straps. The camera was housed in a plastic bag, which also contained a small external battery capable of powering the camera for approximately 8 hours. An internal SD card recorded images at 30 second intervals. In the second and third deployments, the setup was improved by security camera housing, a tripod, and a large external battery. The second deployment recorded images at 30 second intervals, but the SD card was upgraded for the third deployment such that images were recorded every 5

seconds. Images of the original and improved camera setups are shown in Figure 13.

After recovery, photographs containing container ships were manually identified. The time and direction of boat passages were recorded; boats traveling northwest towards the boat are referred to as “inbound,” while those traveling southeast are “outbound.” These records paired measured water level fluctuations with times of known ship passage. The direction of ship travel has implications for the time delay of water level fluctuations between the pressure transducers. For example; for a ship traveling eastward out of the port, water level fluctuations caused by the ship’s wake will be observed by the pressure transducers at Main Channel West and South Channel before they will be observed at Main Channel East. The reverse is true for a ship traveling westward to the port.

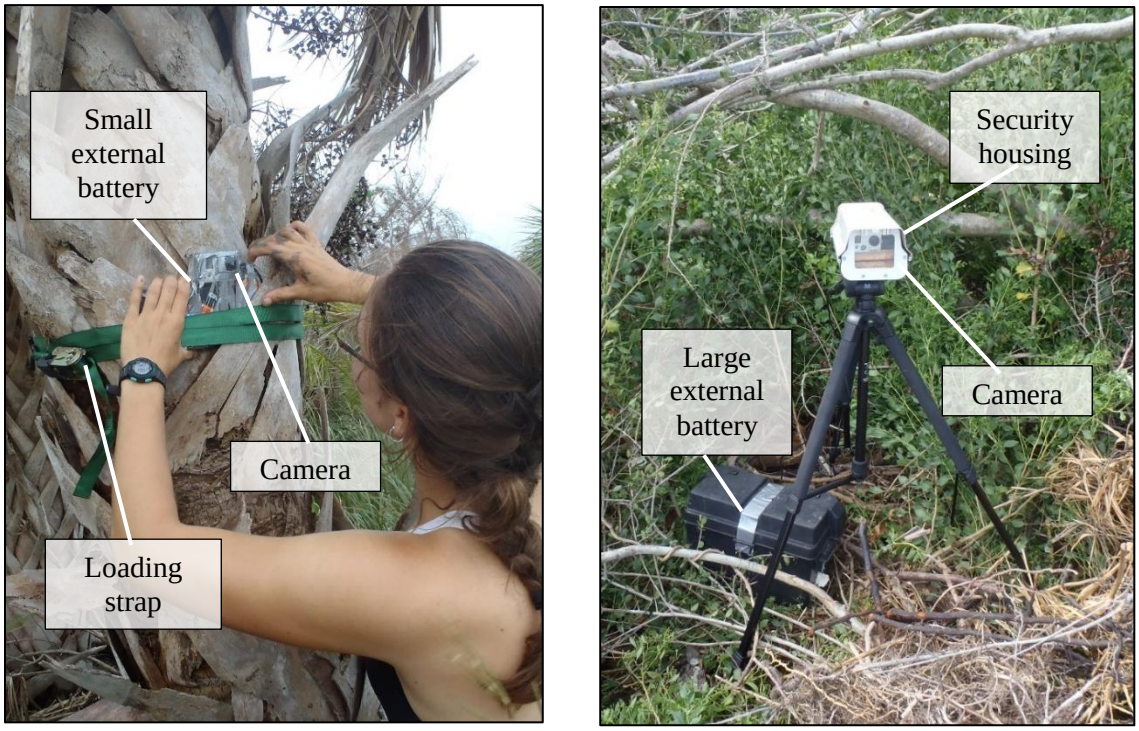

Figure 13: (Left) Initial camera setup used in the August deployment and the (right) improved camera setup used in the October and November 2017 deployments.

2.2.5 GPS & Survey

A GPS system was used for the boat-mounted ADCP measurements and bathymetric surveying. For the ADCP measurements, two dual-frequency Ashtech ProFlex 500 GNSS rovers were placed on the Pontoon boat. Each receiver was connected to an Ashtech GPS antenna; as shown in Figure 14, one was placed on the aft end of the roof, and the other was placed on the forward end of the roof. A base station was set up at the Lazaretto Creek Boat Launch and with a tripod-mounted antenna and an Ashtech Z-12 surveyor, which recorded data every 10 seconds.

Figure 14: Ashtech GPS antennas on the pontoon boat roof for ADCP measurements and bathymetric surveying.

Figure 15: Ashtech GPS antenna mounted to the rear of the Zodiac for surveying.

Bathymetric surveying was conducted on three separate field trips which each utilized a slightly different GPS setup. The first day of surveying coincided with the ADCP measurements, and thus the setup was the same as that described above. The second survey used a single rover, a ProFlex 500, and an antenna mounted to the rear of the Zodiac, as shown in Figure 15; the GASA Continuously Operating Reference Station (CORS) was used as the base station. The third survey also used a ProFlex 500 with an antenna mounted to the rear of the Zodiac, but a base station was set up with a ProFlex 500 recording at 1 Hz. These setups are summarized in Table 7.

Table 7: GPS Receivers and Recording Rates/Intervals

ADCP (May-9)	2 dual-frequency Ashtech ProFlex 500s	2 Hz	Z-12 Surveyor	10 sec
Survey 1 (May-9)	2 dual-frequency Ashtech ProFlex 500s	2 Hz	Z-12 Surveyor	10 sec
Survey 2 (Oct-7)	1 dual-frequency Ashtech ProFlex 500	2 Hz	NA (CORS data)	NA (CORS data)
Survey 3 (Nov-4)	1 dual-frequency Ashtech ProFlex 500	2 Hz	1 dual-frequency Ashtech ProFlex 500	1 sec

For surveying, a transducer was pinned on an aluminum mount and submerged either in the moon pool or off the rear of the boat for the pontoon and Zodiac, respectively. The transducer was connected to a CEESTAR fathometer with a cable, which was in turn connected to a computer running Hypack 2013 surveying software and powered by an external battery. As discussed above, a GPS antenna and receiver were also used in the setup; the receiver was connected to Hypack so that GPS data and bathymetry data were synced by the software. A water-resistant box contained the computer, battery, fathometer, and GPS receiver, while a small monitor, mouse, and keyboard were left outside the box but underneath a splash guard.

For the GPS data collected in May and November, the Online Position User Service (OPUS), accessed at https://www.ngs.noaa.gov/OPUS, was used to find the base station coordinates. In October, the CORS GASA station was used as the base station, and its coordinates

were obtained at https://geodesy.noaa.gov/CORS/. The coordinates are provided in Table 8.

Table 8: GPS Base Station Coordinates

May-09	32 0 57.27991	80 53 25.81447	-27.661
Oct-07	32 01 25.49276	81 03 36.76167	-21.296
Nov-04	32 0 57.26671	80 53 25.83118	-27.698

The rover data was post-processed using the Rinex Converter v.4.2.5 and GravNav v.7.80.2315 software. The UTM zone 17 coordinates, along with the NAVD88 heights, were output from the software as ASCII files. MATLAB was used for data analysis; data with poor quality control values (> 1) from the GravNav output were removed, and the data was interpolated. The depth and time data from the bathymetric surveying were exported out of Hypack, and GPS data was interpolated to the same time stamps as the depth data in MATLAB.

2.3 Meteorological

Wind, air temperature, and air pressure data for the duration of each Aquadopp deployment were downloaded for the NOAA Fort Pulaski Monitoring Station 8670870 from *https://tidesandcurrents.noaa.gov/met.html?id=8670870.*

2.4 Ship Records

Vessel traffic data, or Automatic Identification System (AIS) data, were downloaded from https://marinecadastre.gov/ais/. This data comes from navigation safety devices onboard large vessels that transmit vessel location and characteristics. For the data analyzed here, the mean time between transmissions for a ship was about three minutes. Data was downloaded for transmissions within a region around the Savannah River for 2015 through 2017. The data obtained from each transmission for a ship include

the time, latitude and longitude coordinates, International Maritime Organization (IMO) number, Maritime Mobile Service Identity (MMSI), vessel type, course over ground, draft, length, width, speed, and status (“moored”, “under way using engine,” etc.).

To filter this large amount of data, a smaller region surrounding Bird-Long Island was defined with a box, and points lying outside it were discarded. An example of the region is given in Figure 16, which shows all 12,632 points in the month of October 2017 that are within the defined region. To group the data by ships, the data were then sorted by MMSI. Since many ships pass the island multiple times during the period of data download, the data points for a particular ship were split into different passages past the island by identifying time gaps in transmissions from the ship greater than two hours. Ultimately, this provided a set of data points for each transit of the ship past the island.

Figure 16: Example from October 2017 of AIS data points that are within the defined region and retained for analysis.

Passages were assigned an “inbound” or “outbound” direction based on their course over ground, or heading. The relative velocity of the boat, with respect to the current velocity, was calculated from the transmitted speed data and river current data from a numerical model. For large vessel passages, the time record of the ship’s position was interpolated onto a continuous line tracing the shipping channel, providing an estimated time series of its position with finer resolution than the transmitted data.

2.5 Model Setup

To further characterize the site, numerical models simulating the waves, currents, and tides are established for the region. The numerical model domain was created (Figure 17) encompassing the Savannah River, Wassaw Sound, and Ossabaw Sound. The tidal and wind driven flows are simulated using the Regional Ocean Modeling System (ROMS), embedded in the Coupled-Ocean-Atmosphere-Wave-Sediment Transport (COAWST) Modeling System. ROMS is a member of a general class of three-dimensional, free surface, terrain following numerical models that solve three dimensional Reynolds-averaged Navier-Stokes equations using the hydrostatic and Boussinesq assumptions. ROMS is configured to simulate the fall Aquadopp deployment. Simulation results for the first 2 days are neglected to eliminate the spin up effect of the model. The ROMS tidal forcing is generated by interpolating the ADCIRC tidal database model at the open boundary nodes of the ROMS grid for 9 harmonic constituents, including K1, O1, Q1, M2, S2, N2, K2, M4, M6. The wind data from the NOAA Fort Pulaski Monitoring Station is applied uniformly throughout the domain. Time series of the discharge from the USGS gage station 02198500 on the Savannah River near Clyo, Georgia is input on the northern boundary. The model output includes hourly water level

and currents throughout the domain.

Numerical wave modeling is done with SWAN, a third-generation spectral wave model (Booij et al., 1999) that computes wave propagation in time and space by taking shoaling, refraction, nonlinear wave interactions, whitecapping, breaking, and generation by wind into account. The wave model uses the same grid and includes the water level and current data from the ROMS simulation. As with the circulation model, wind input is from the NOAA Fort Pulaski Monitoring Station and is applied uniformly throughout the domain. The offshore boundary conditions are generated from hourly wave data from the NOAA NDBC buoy 41008 at Gray's Reef, Georgia. Wave parameters are computed throughout the domain, including the wave height, peak period, and mean wave direction.

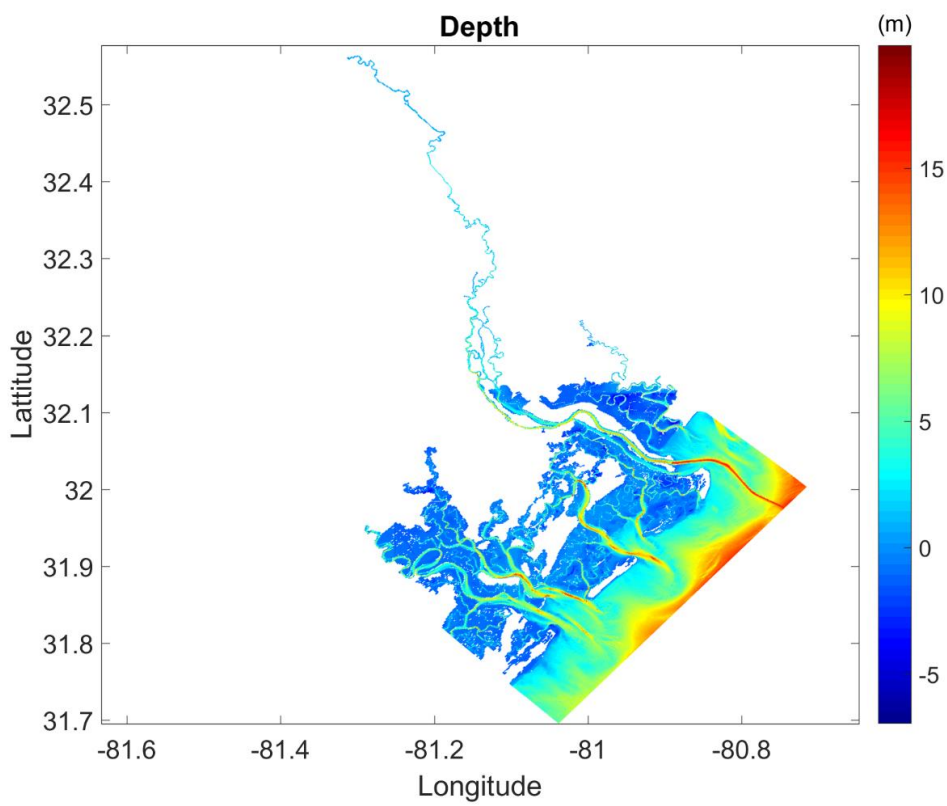

Figure 17: Numerical model domain showing color contours of the bathymetry.

2.6 Supplemental South Channel Field Data Collection

In November, 2018, an additional set of field data was collected to record the propagation of ship wake along the South Channel. An instrument array consistent of three pressure transducers and an Aquadopp was deployed for three days spanning the South Channel along Bird-Long Island. Ship records corresponding to the deployment time period were downloaded from an online AIS database. The methods and results of this study are discussed further in Section 3.7.2.

3. RESULTS AND ANALYSIS

3.1 Tidal Hydrodynamics

3.1.1 Spatial Structure

The boat-mounted ADCP velocity profiles of the Main Channel and blowout demonstrate the spatial variability of the flow in these locations. A total of 26 profiles were measured along 3 three transects on May 5th, 2017 over a duration of about six hours as the tide transitioned from ebb to flood. Transect 1 spans the blowout between Bird-Long Island and Cockspur Island, while Transects 2 and 3 span the Main Channel at the southeastern end of Bird-Long Island, as shown in Figure 18. The full set of velocity profiles for Transects 1, 2, and 3 are shown in Figures 19-21 respectively. Figures 22-24 show depth-averaged velocities across all three transects for specific profiles representing conditions at three stages of the tidal cycle. In these figures, the "total mean" is the velocity averaged over the full water column, the "surface mean" is the average of the top third of the water column, and the "bottom mean" is the average of the bottom third. The time at which each profile was recorded is listed at the top of the figures.

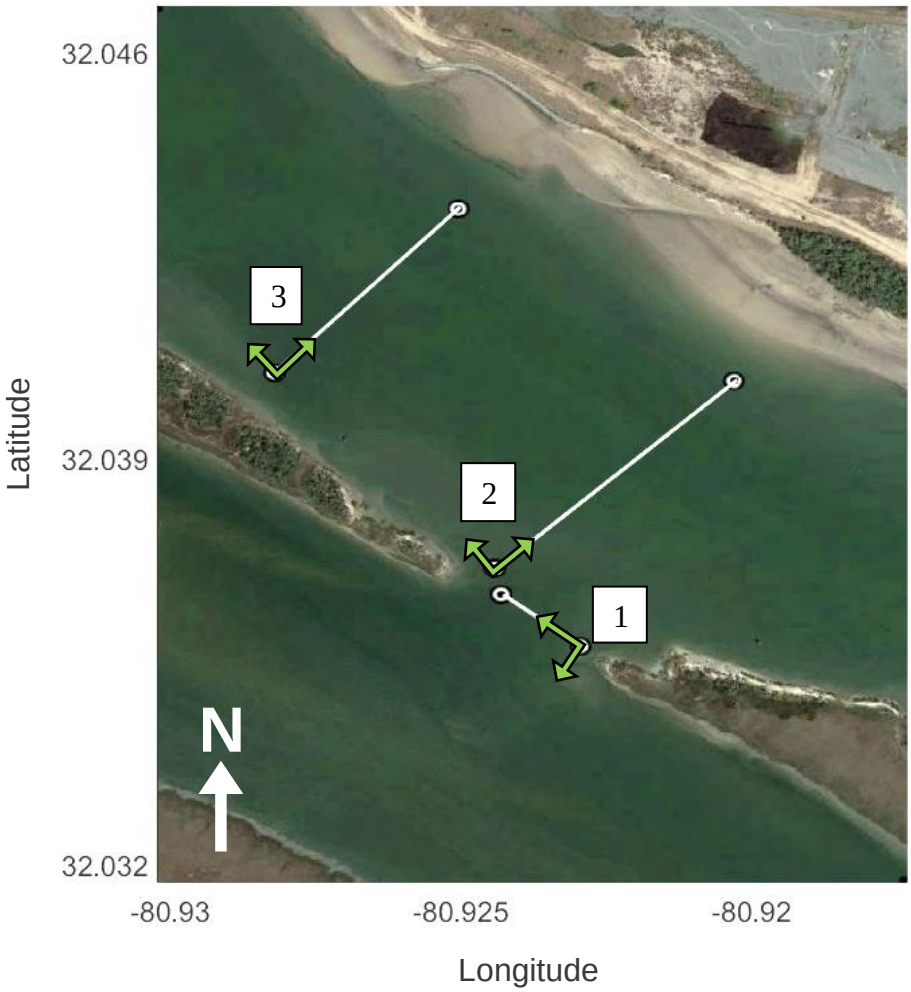

Figure 18: Boat-mounted ADCP Transects 1 - 3 at the southeastern end of Bird-Long Island with positive directions labeled for the transect velocity coordinate system. For Transect 1, the positive along-blowout component is in the northwest direction, and the positive through-blowout component is in the southeast direction. For Transects 2 and 3, the positive along-channel component is in the northwest direction, and the positive across-channel component is in the northeast direction.

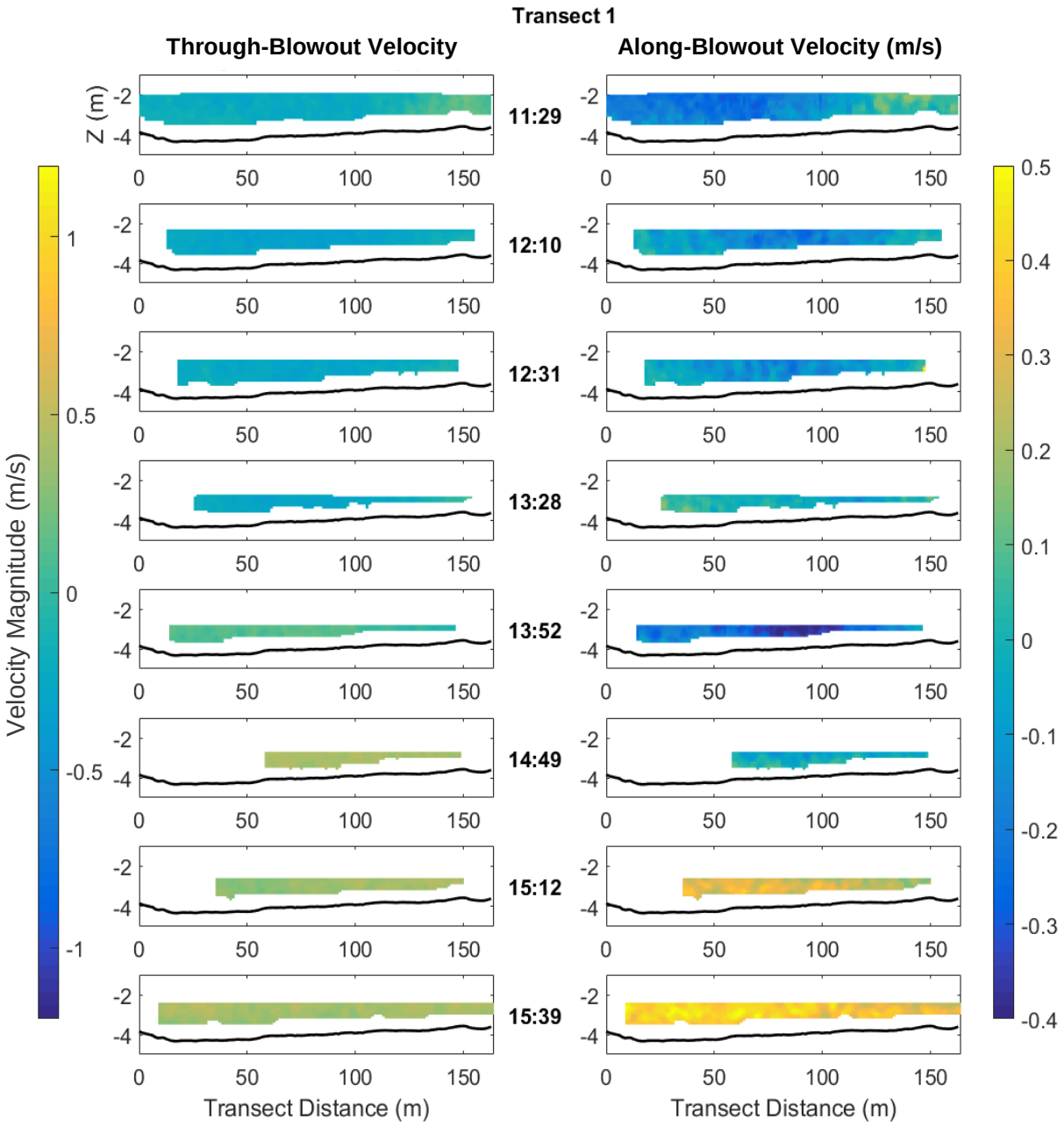

Figure 19: (Left) Through-blowout velocity profiles and (right) corresponding along-channel velocity profiles for Transect 1, with the time of each profile centered between the plots. Sign conventions are defined in Figure 18.

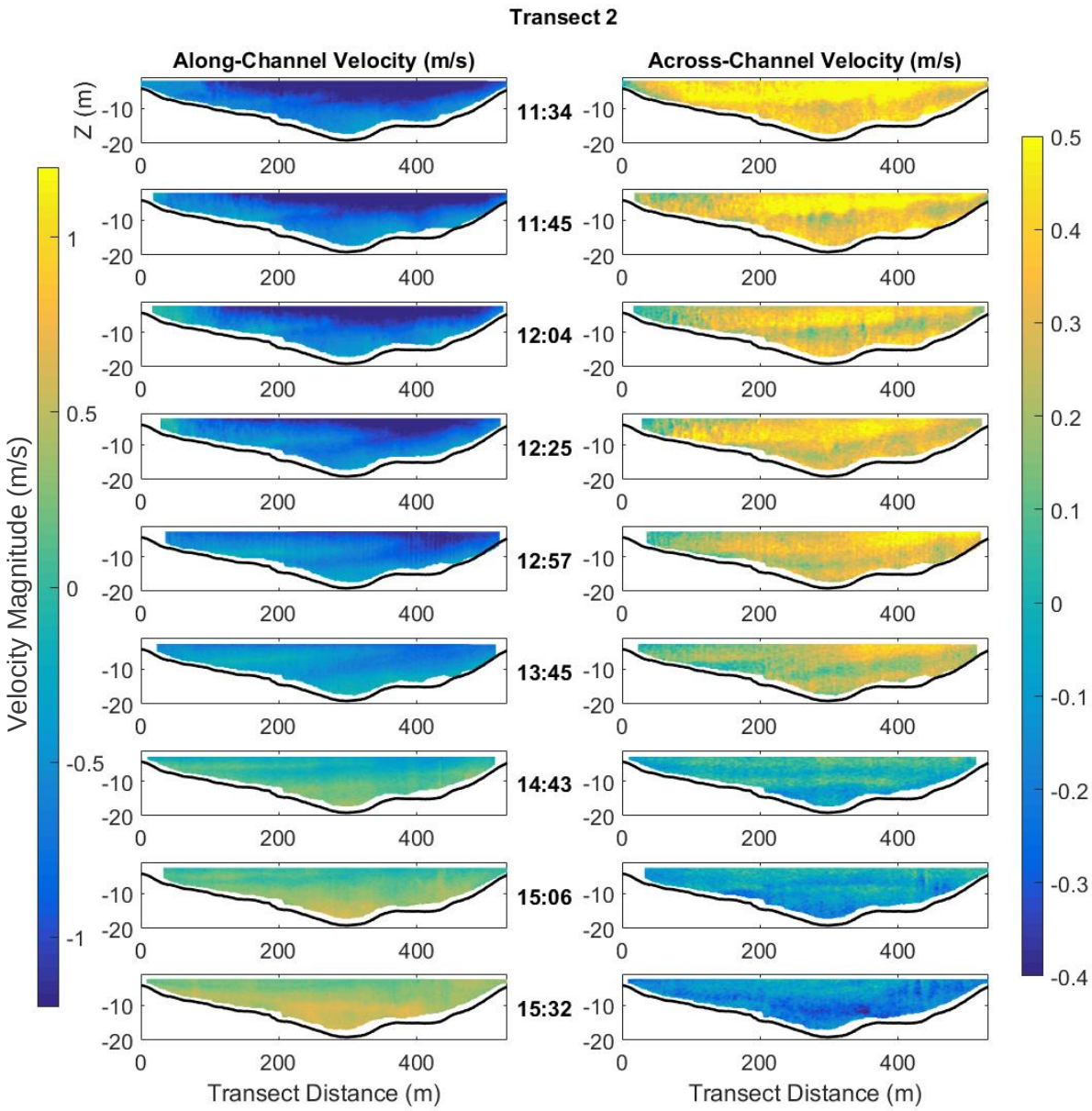

Figure 20: (Left) Along-channel velocity profiles and (right) corresponding across-channel velocity profiles for Transect 2, with the time of each profile centered between the plots. Sign conventions are defined in Figure 18.

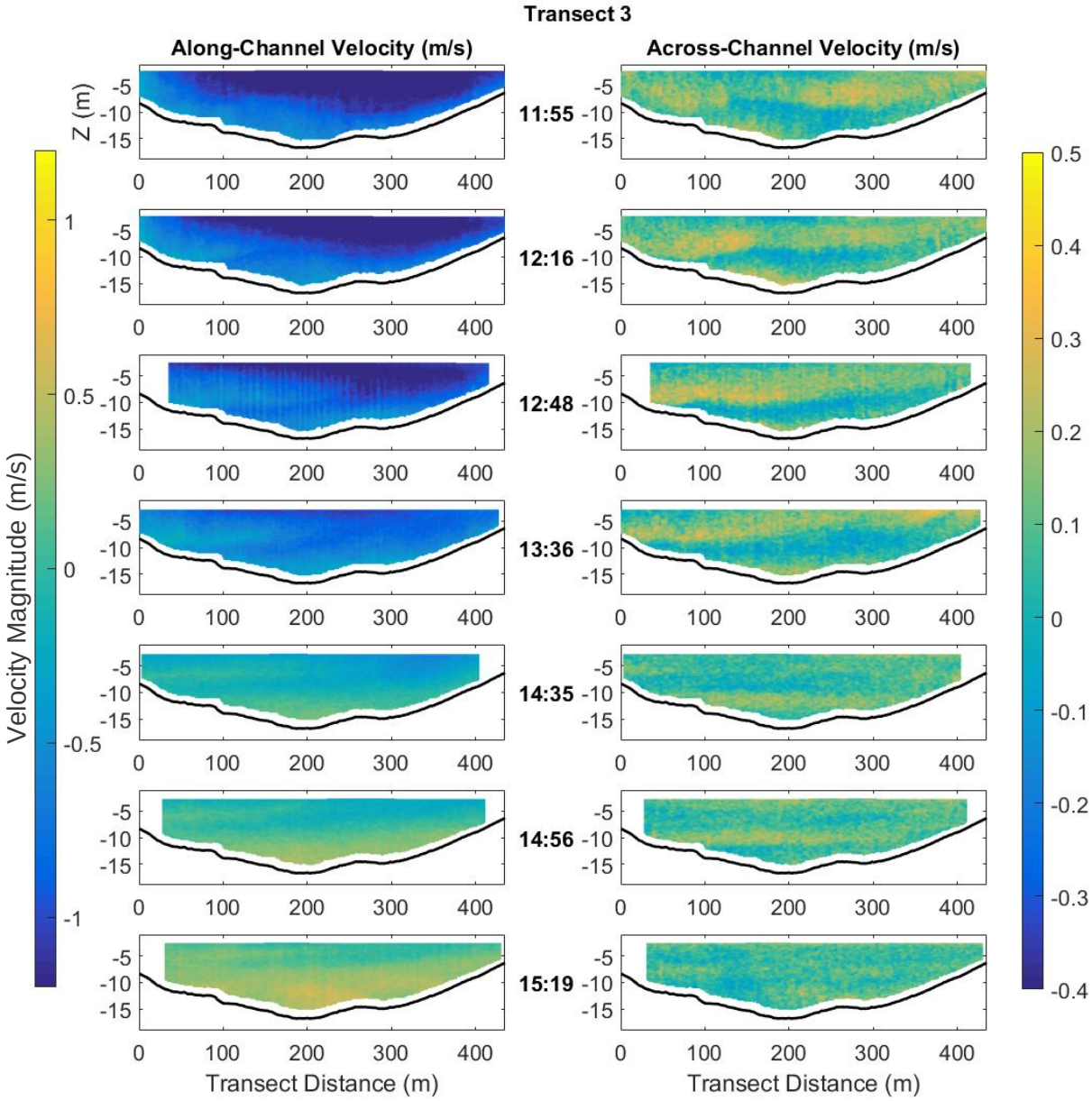

Figure 21: (Left) Along-channel velocity profiles and (right) corresponding across-channel velocity profiles for Transect 3, with the time for each profile centered between the plots. Sign conventions are defined in Figure 18.

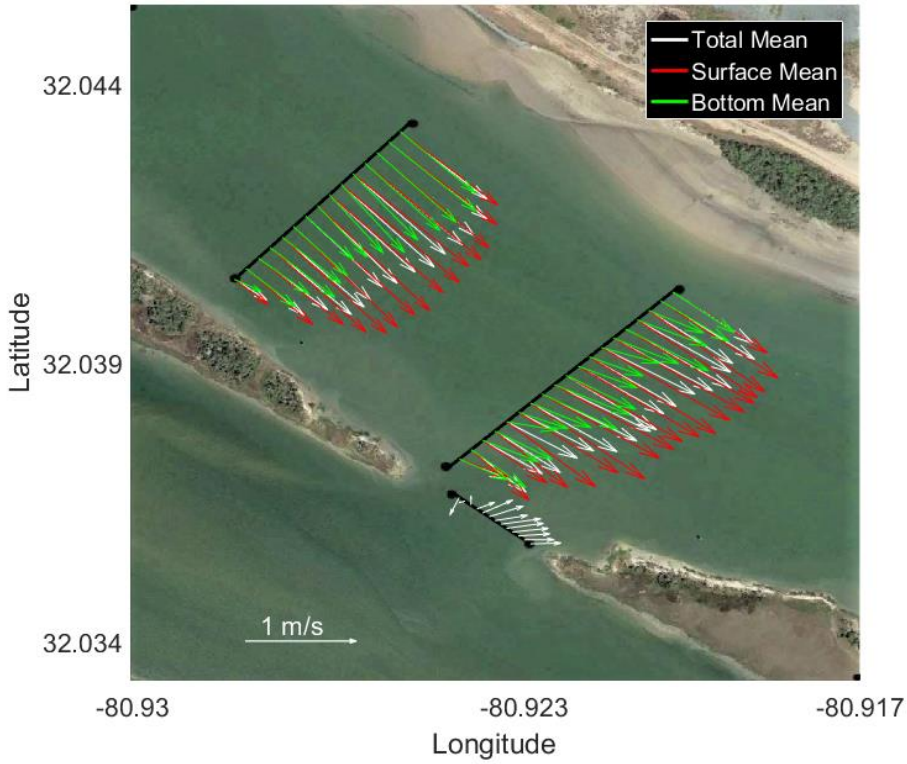

Figure 22: Mean total, surface, and bottom velocities during ebb tide.

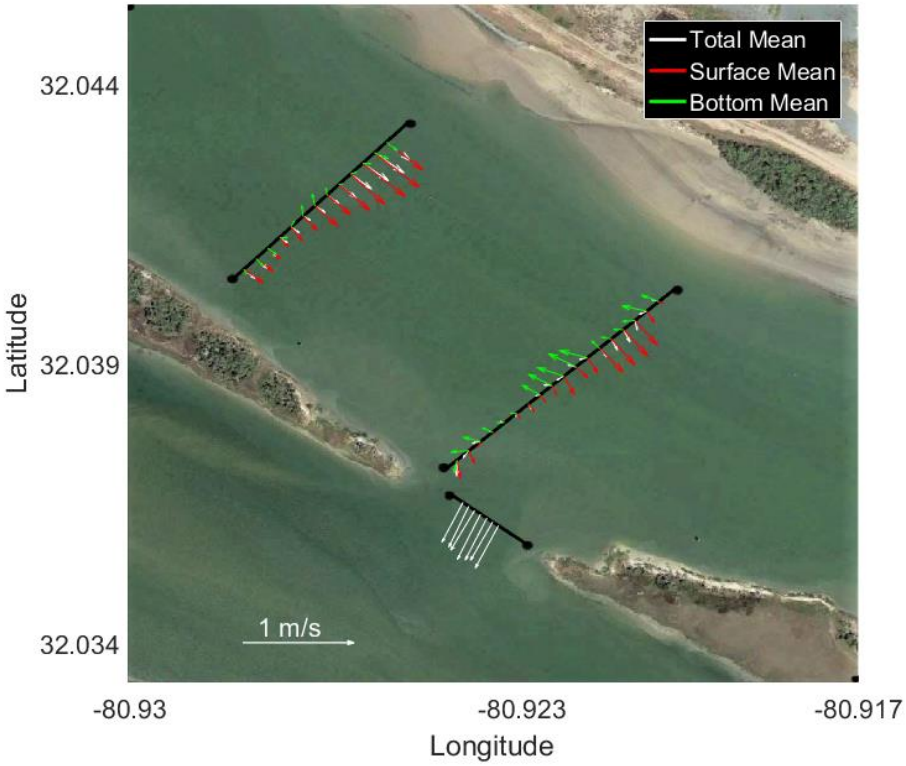

Figure 23: Mean total, surface, and bottom velocities during an ebb to flood transition.

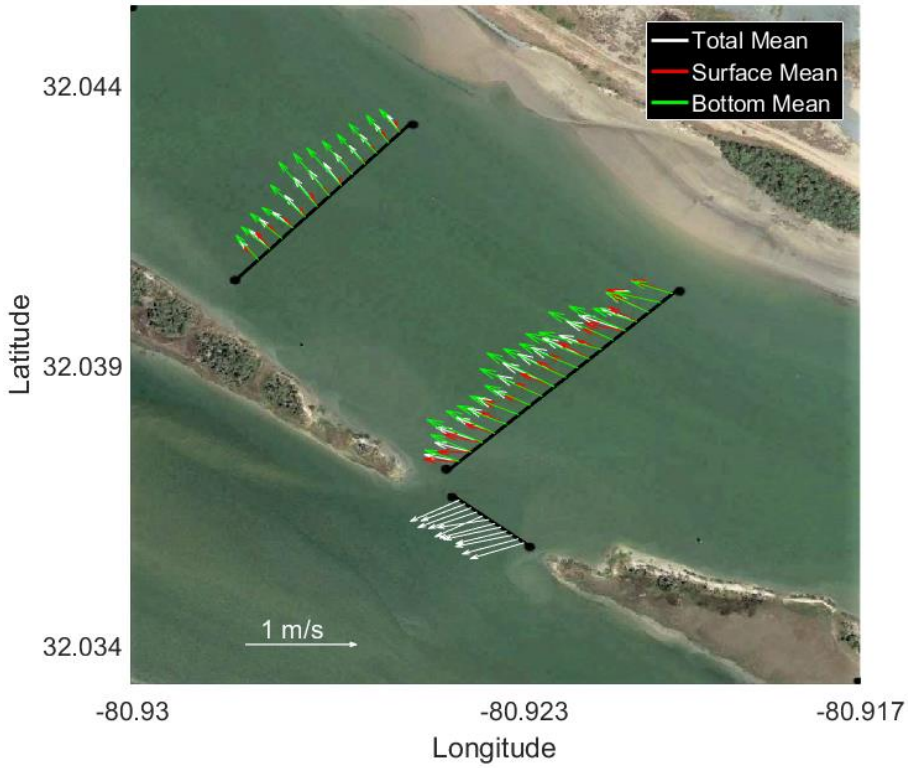

Figure 24: Mean total, surface, and bottom velocities at the beginning of flood tide.

At Transect 1, the blowout, velocities reach nearly 0.5 m/s with through-blowout flows generally exceeding along-blowout flows. Figure 22 shows that during ebb tide, flow in the blowout is primarily from the South Channel to the Main Channel, with a small region of flow reversal at the end of the transect. As the currents in the Main Channel transition from ebb to flood, the blowout velocities are stronger than the Main Channel flows, and they rotate clockwise from the northeastern direction, to the downriver direction, and finally to the southwestern direction at flood tide. This implies that the exchange between the two channels is “South to Main” at ebb tide, and “Main to South” at flood tide. The blowout is too shallow for the observation of significant vertical flow structures. Considering the horizontal flow structure, velocities are often relatively consistent along the transect but tend to be slightly stronger at the center of the blowout.

Except for the small flow reversal shown in Figure 22, the velocities are also consistent in direction across the transect.

Transects 2 and 3, spanning the Main Channel, have similar flow characteristics. Peak velocities reach 2 m/s and occur near the surface and center of the transects. Flows at the bottom of the Main Channel are weaker than surface flows, and are thus the first to reverse direction during the transition from ebb to flood tide, as evident in the along-channel profiles and emphasized in Figure 23. During the ebb-to-flood transition, the bottom velocities may be fully reversed from the surface velocities, which is particularly prominent in Transect 2 at 14:43. The vertical structure exists until the surface current slows to slack tide and then reverses direction to flood tide conditions. The across-channel profiles also demonstrate spatial variability, with flows up to 0.4 m/s and of opposite cross-channel directions occurring simultaneously, indicating cross-channel circulation cells. Lastly, the slowest velocities in the profiles generally occur along the boundaries of the channel.

3.1.2 Temporal Characteristics

Temporal hydrodynamics characteristics, particularly those pertaining to tidal cycles, are described in the data obtained from the two long-term Aquadopp deployments. Figures 25 and 26 provide the full water level and the one-minute time-and depth-averaged velocity time series from the Aquadopp profiling data for both deployments.

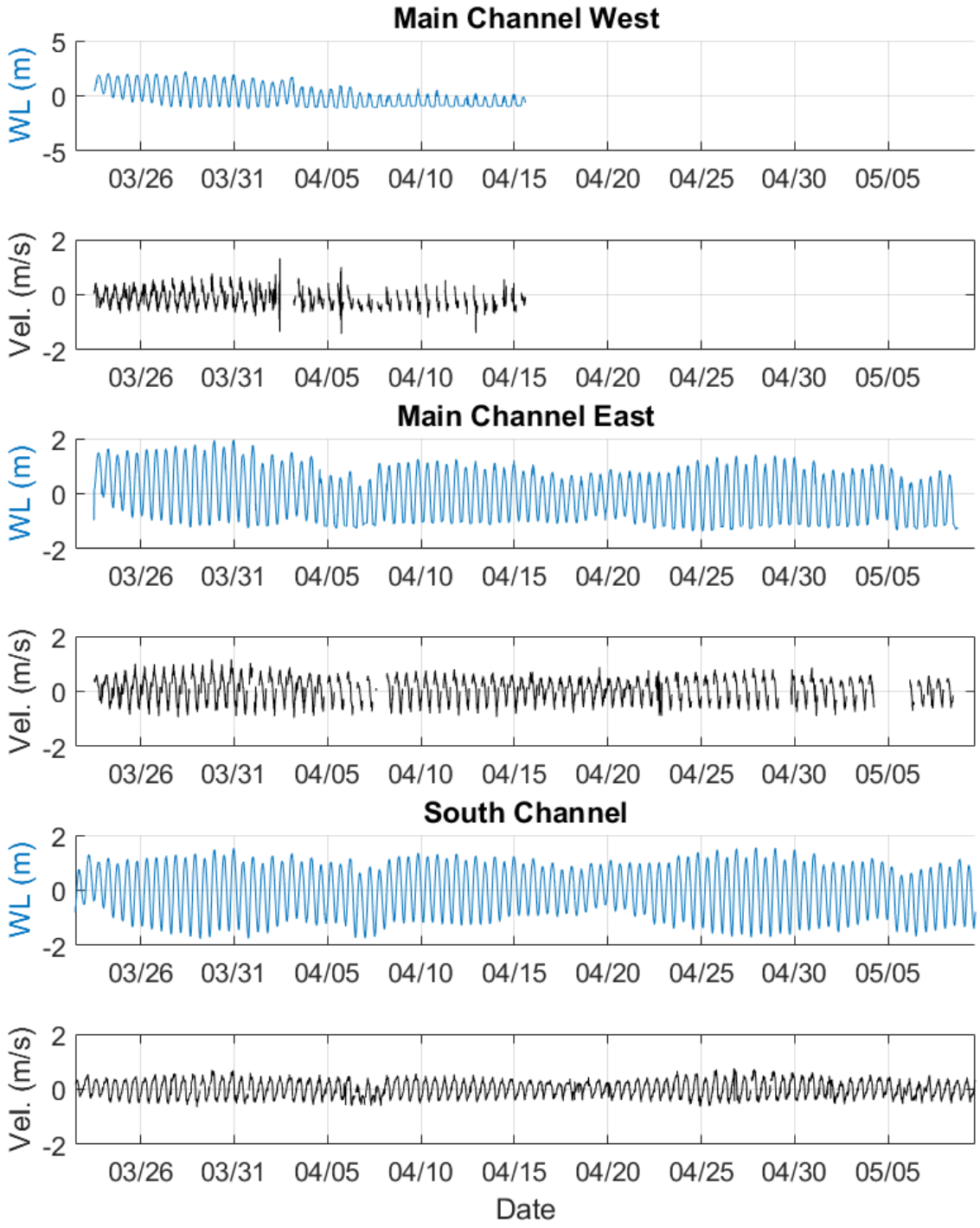

Figure 25: Water level (WL) and velocity (Vel.) time series from all three sites measured in the spring 2017 Aquadopp deployment. The mean water level has been removed, and positive velocity corresponds to flood tide.

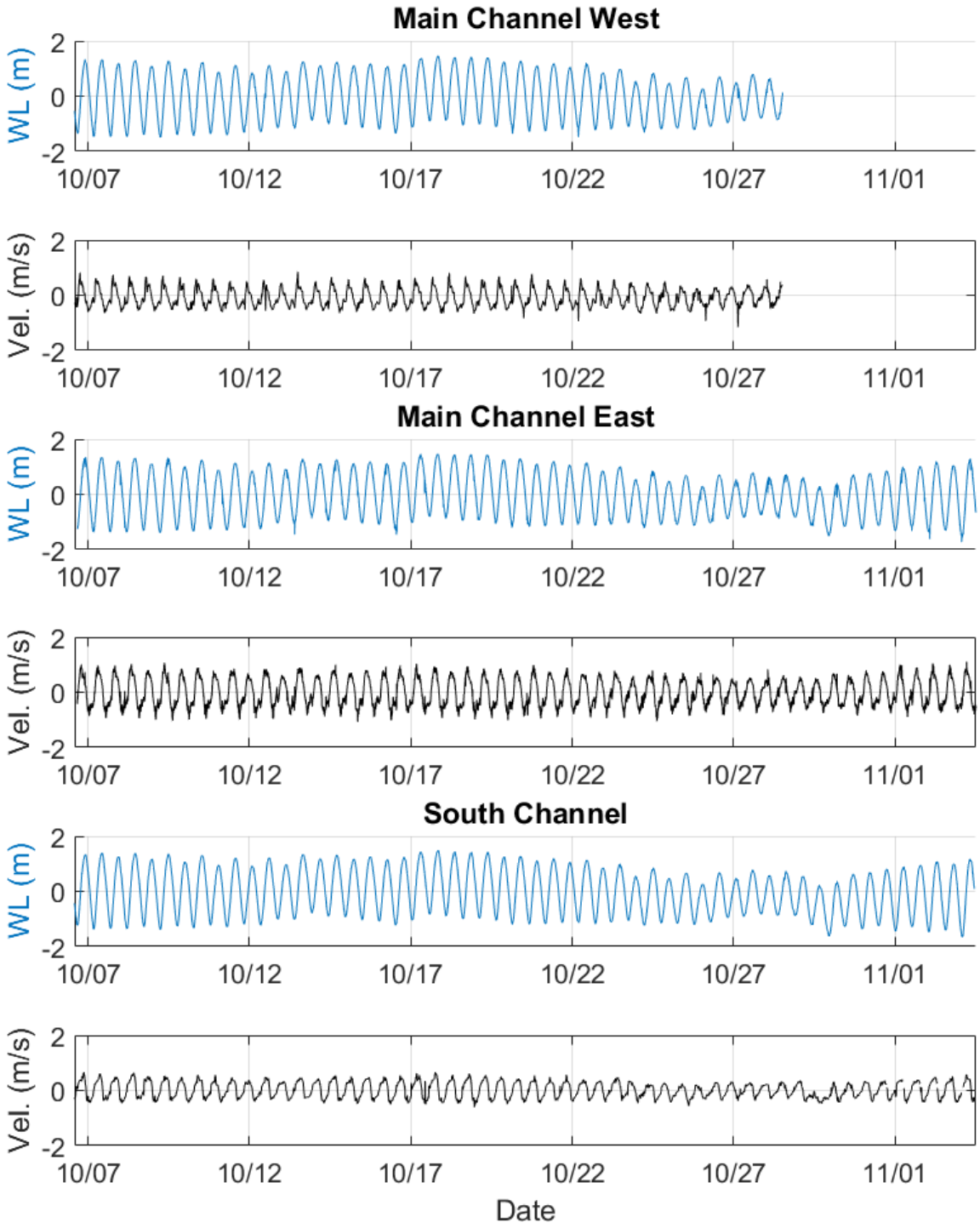

Figure 26: Water level (WL) and velocity (Vel.) time series from all three sites measured in the fall 2017 Aquadopp deployment. The mean water level has been removed, and positive velocity corresponds to flood tide.

During the spring deployment, the instruments in the Main Channel were moved shoreward by ship wake, and the corresponding time series show significant loss of data quality once the instruments are no longer submerged throughout the full tidal cycle. The Aquadopp at Main Channel West washed completely onto the beach and was exposed to air continuously, whereas the instrument at Main Channel East was washed to shallower water and was exposed to air intermittently for the remainder of the deployment. There was no movement of the Aquadopp in the South Channel. The Aquadopp frames were modified for the fall deployment, and none of the Aquadopps moved significantly during this second deployment. However, due to battery failure, the instrument at Main Channel West stopped recording data one week prior to recovery.

Both sets of time series demonstrate that tidal ranges are as great as 2.8 m at spring tide, and as small as 1.3 m at neap tide, with no significant variation between the three sites. Velocities are more variable between locations, but this is in part a result of the flow spatial distribution discussed previously and the varying deployment depths of the instruments; the peak velocities measured are provided in Table 9. Overall, velocities in the South Channel are significantly lower than peak velocities measured in the Main Channel.

Table 9 also provides the mean durations of flood and ebb tide at each location, as well as the standard deviation (STD) of the duration. Histograms of the durations are given in Figure 27. Overall, flood conditions persist longer in the South Channel, and ebb conditions persist longer in the Main Channel. The mean flood tide at the South Channel site is 38 minutes longer than the mean flood tide at Main Channel West and 29 minutes longer than the mean flood tide at Main Channel East. Similarly, the mean ebb tide at

Main Channel West is 31 minutes longer than the mean South Channel ebb tide; at Main Channel East, the ebb tide is 40 minutes longer than the mean South Channel ebb tide. This is also apparent in the histograms: the distribution of flood tides in the Main Channel are skewed downwards of 6 hours, while the South Channel flood tides are skewed just above 6 hours. It is also clear that the Main Channel West has the greatest discrepancy between flood and ebb tide durations.

Table 9: Fall 2017 Tidal Current Peak Velocities and Durations

Site	Mean Depth (m)	Peak Flood Velocity (m/s)	Mean Flood Duration (hr)	STD of Flood Duration (hr)	Peak Ebb Velocity (m/s)	Mean Ebb Duration (hr)	STD of Ebb Duration (hr)
Main Channel East	3.64	1.11	5.85	0.40	1.08	6.56	0.33
Main Channel West	3.27	0.86	5.69	0.65	1.16	6.71	0.64
South	2.20	0.66	6.33	0.57	0.60	6.05	0.53

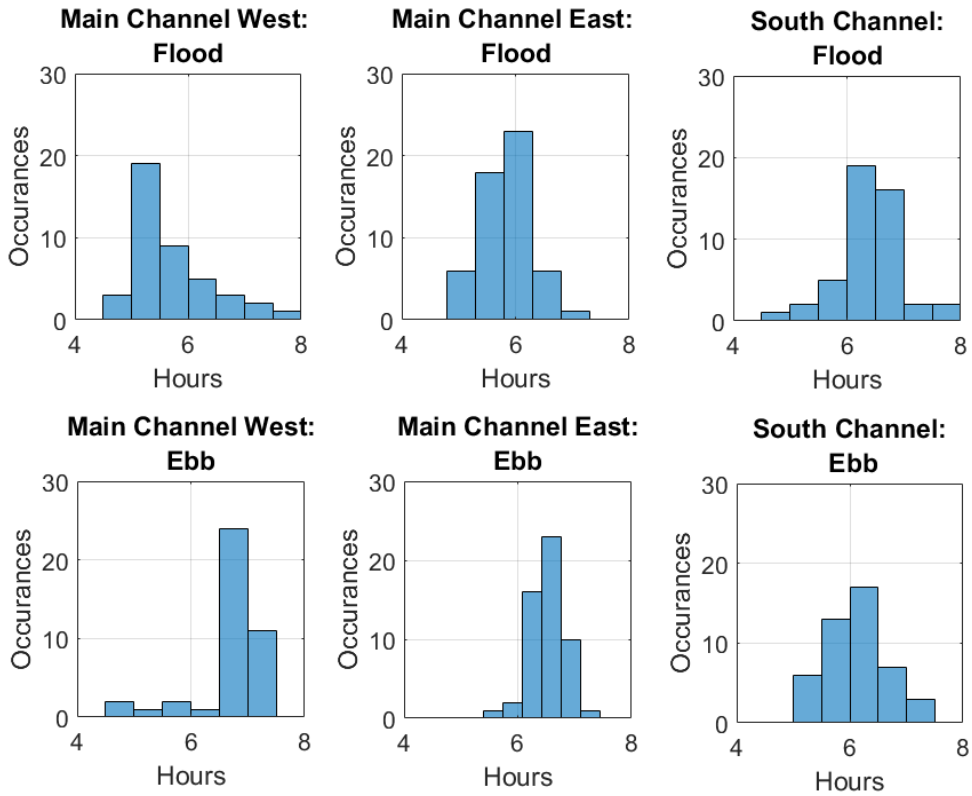

Figure 27: Histograms of tidal current durations in the fall deployment.

Stage-velocity diagrams of band-pass filtered Aquadopp water level and velocity data (Figure 28) demonstrate differences in the tidal characteristics; data was filtered with cutoff frequencies of 3 and 33 hours to isolate tidal frequencies. The diagrams on the left-hand side of the figure are from spring Aquadopp data and include only the data recorded before the instruments were washed shoreward. The diagrams on the right-hand side represent the fall deployments, which captured the full spring-neap cycle.

At Main Channel West, the spring tide behaves like a standing wave where the water levels and velocities are out of phase. The phase-velocity diagram is largely aligned with the vertical axes, and currents are stronger at the water level zero-crossings than at high and low tide. The site is flood-dominant at spring tide, as the strongest currents

occur during flood tide just before the zero-crossing on a rising tide. On a falling tide, currents decrease after the zero-crossing, but then remain constant or even increase slightly around the -1 m water level before reversing at low tide. This creates a point in the phase-velocity diagram at low tide that contrasts the roundness of the diagrams at high tide, which implies a smoother transition from flood to ebb currents at high tide than the ebb to flood transition at low tide.

The Main Channel West neap tide has more progressive wave behavior, with the strongest ebb current just after high tide, and the strongest flood current just after low tide. Compared to the spring tide at this site, flood currents are decreased from 0.65 m/s to 0.35 m/s, but maximum ebb currents remain at about 0.50 m/s and occur at the same water level. Thus, the tide is flood-dominant at spring tide, but ebb-dominant at neap tide. Also, the pointed feature at the low spring tide is not present at neap tide, indicating overall smoother transitions from neap tide ebb to flood.

The stage-velocity diagram for the Main Channel East spring tide is larger than that of Main Channel West, tilted approximately 30 degrees clockwise from the vertical, and exhibits the same pointed feature at low tide observed at Main Channel West. Both spring and neap tidal currents peak near the water level zero-crossings and therefore exhibit standing wave behavior. Maximum flood currents reach 0.90 m/s at spring tide, and 0.44 m/s at neap tide while maximum ebb currents reach 0.81 m/s at spring tide and 0.52 m/s at neap tide. This indicates that Main Channel East is also flood-dominant at spring tide and ebb dominant at neap tide, though the asymmetry is not as strong as that at Main Channel West.

The South Channel tide exhibits standing wave behavior at both spring and neap

tide, as seen in the general alignment of the stage-velocity diagram with the vertical axis. There is a slight tilt difference between spring and neap high tides. This means that at spring tide, the maximum flood current occurs just before high tide, and the maximum ebb current occurs near the water level zero-crossing. In contrast, at neap tide, the maximum flood tide occurs at the water level zero-crossing, and the maximum ebb tide occurs just after high tide. Maximum flood currents reach 0.53 m/s at spring tide, and.26 m/s at neap tide while maximum ebb currents reach 0.50 m/s at spring tide and 0.21 m/s at neap tide. This indicates that, in contrast to the Main Channel sites, the South Channel site exhibits relatively symmetric spring and neap tides.

Data obtained from the Aquadopp vertical profiles are used to further illustrate the tidal asymmetry with additional details about the vertical flow structure. Figure 29 presents the velocity profiles for the three sites during four tidal cycles at the beginning of the spring deployment. The profiles are plotted as a function of elevation, the vertical distance above the instrument at which the velocity was measured, over a duration of 48 hours. These profiles show that velocities were strongest as measured at Main Channel East; however, the velocities may be influenced by the cross-channel position of the instrument. The more important trend is that flood velocities persist longer at the South Channel site than the Main Channel sites, though the velocities themselves are weaker than Main Channel flood velocities. Main Channel West velocities are also weak; this may be due to the location of the instrument, or a sheltering effect of the island.

Tidal constituents for the Main Channel East and South Channel sites were determined with harmonic analysis (Pawlowicz et al., 2002) of the Aquadopp water level and velocity time series. The constituents are listed in Tables 10-13.

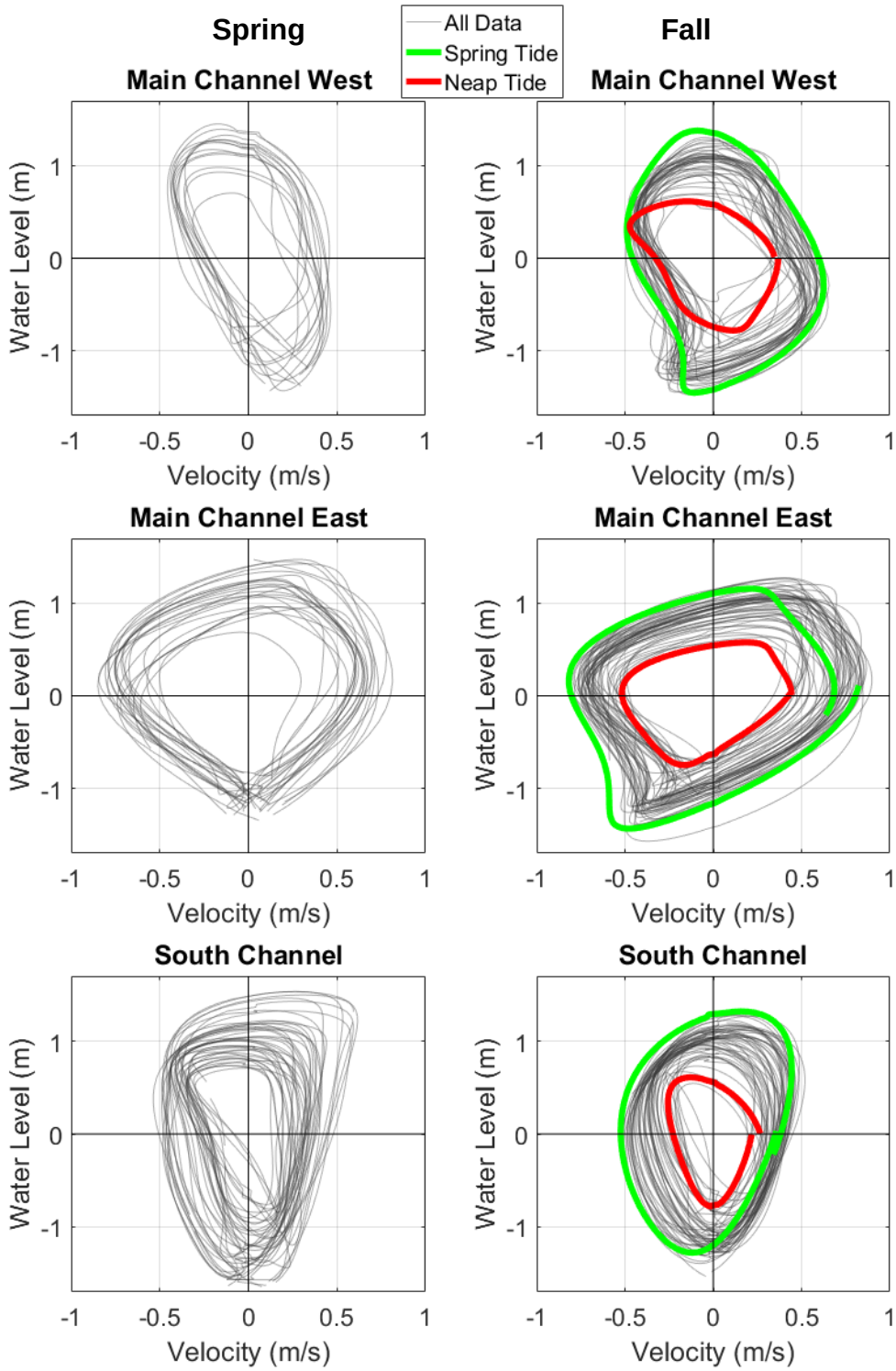

Figure 28: Stage-velocity diagrams from the (left) spring and (right) fall Aquadopp deployments with sample spring and neap tides identified in the fall data. Temporal progressive is counterclockwise, and velocity is positive at flood tide.

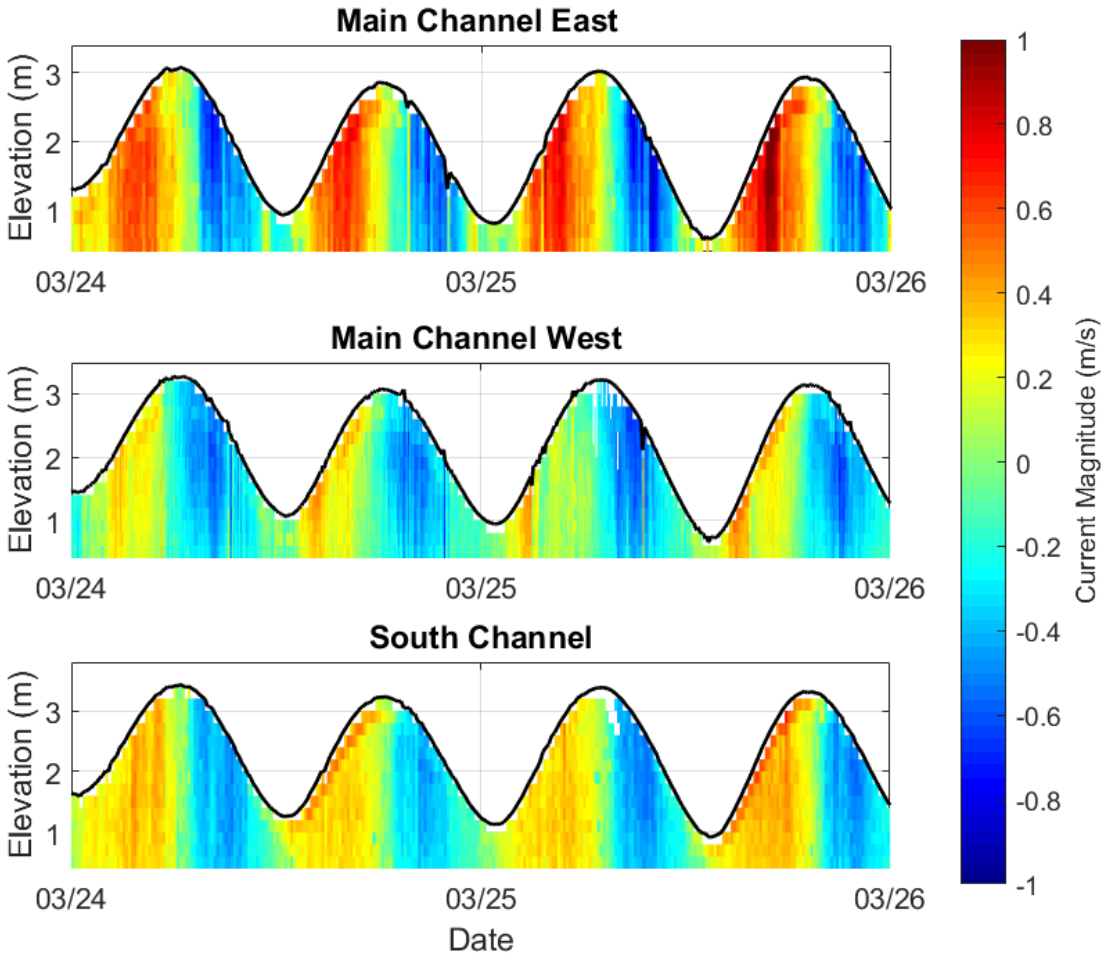

Figure 29: Asymmetric tidal flow measured during the spring deployment. The flow at Main Channel East and South Channel exhibits long periods of high velocity flow on the flood tide (red), and shorter periods of similarly high-speed flow on the ebb tide (blue). The flow at Main Channel West, in contrast, exhibits longer periods of high speed ebb velocity and shorter periods of flood velocity.

Table 10: Main Channel Velocity Tidal Constituents

Name	Frequency (1/hr)	Major (m/s)	Major error (m/s)	Minor (m/s)	Minor Error (m/s)	Inc (deg)	Inc Error (deg)	Phase (deg)	Phase Error (deg)	Signal to Noise
O1	0.038731	0.043	0.016	0	0.01	130.8	22.9	104.7	26.7	6.7
P1	0.041553	0.032	0.014	0.005	0.01	131.0	25.7	52.6	25.6	5.2
K1	0.041781	0.062	0.016	0.003	0.02	132.0	14.6	104.8	15.4	15
N2	0.078999	0.154	0.037	-0.001	0.04	132.9	16.3	203.6	14.3	17
M2	0.080511	0.605	0.042	-0.004	0.04	132.0	3.6	198.0	3.8	210
S2	0.083333	0.177	0.038	-0.001	0.04	129.9	11.9	240.5	12.9	22
K2	0.083562	0.101	0.043	0.002	0.04	126.8	29.0	136.2	29.2	5.5
M4	0.161023	0.081	0.017	0.003	0.02	128.5	12.4	78.9	11.4	22
M6	0.241534	0.075	0.039	-0.001	0.04	129.2	31.5	121.5	30.9	3.6

Table 11: Main Channel Water Level Tidal Constituents

Name	Frequency (1/hr)	Amplitude (m)	Amplitude Error (m)	Phase (deg)	Phrase Error (deg)	Signal to Noise
O1	0.0387307	0.079	0.019	157.7	14.8	17
P1	0.0415526	0.061	0.015	150.9	17.8	17
K1	0.0417807	0.127	0.018	161.5	9.5	50
N2	0.0789992	0.235	0.043	266.5	10.5	29
M2	0.0805114	0.979	0.041	266.2	2.4	570
S2	0.0833333	0.204	0.046	307.6	14.0	20
K2	0.0835615	0.097	0.054	243.7	33.8	3.2
M4	0.1610228	0.049	0.032	23.2	37.8	2.4

Table 12: South Channel Velocity Tidal Constituents

Name	Frequency (1/hr)	Major (m/s)	Major error (m/s)	Minor (m/s)	Minor Error (m/s)	Inc (deg)	Inc Error (deg)	Phase (deg)	Phase Error (deg)	Signal to Noise
P1	0.0415526	0.026	0.016	0.001	0.01	109.4	19.0	126.9	36.2	2.6
K1	0.0417807	0.036	0.018	-0.002	0.01	109.0	14.2	70.6	29.5	4
N2	0.0789992	0.078	0.03	0.003	0.02	115.39	14.1	198.0	20.5	6.9
M2	0.0805114	0.329	0.032	0.003	0.02	113.0	3.3	173.5	5.5	110
S2	0.0833333	0.063	0.032	0.003	0.02	114.8	15.9	204.1	22.7	3.9
M4	0.1610228	0.071	0.017	0.001	0.01	111.0	8.2	91.9	14.7	18
M6	0.2415342	0.032	0.011	0.002	0.01	115.9	18.2	14.2	24.0	8

Table 13: South Channel Water Level Tidal Constituents

Name	Frequency (1/hr)	Amplitude (m)	Amplitude Error (m)	Phase (deg)	Phrase Error (deg)	Signal to Noise
O1	0.0387307	0.079	0.013	157.3	11.1	36
P1	0.0415526	0.059	0.012	124.3	12.2	22
K1	0.0417807	0.143	0.014	135.6	4.8	110
N2	0.0789992	0.224	0.04	263.9	11.2	32
M2	0.0805114	1.064	0.043	267.4	2.1	610
S2	0.0833333	0.151	0.047	301.5	16.7	10
M4	0.1610228	0.073	0.025	22.7	22.4	8.3
M6	0.2415342	0.016	0.008	123.2	29.2	4.5

3.2 Meteorological Conditions

In Figures 30 and 31, low-pass filtered South Channel water level ("Low-Pass") and water temperature data is paired with meteorological conditions measured at the NOAA Fort Pulaski Monitoring Station.

The impact of wind on the water level is demonstrated by the wind and water level time series. Periods of strong northwesterly winds force water out of the channel and correspond to decreases in the low-pass filtered water level. Conversely, strong southeasterly winds push water up into the river and cause increases in the low-pass filtered water level. The periods of increased wind speed also coincide with strong variations in the air pressure. Strong northwesterly winds are associated with drops in air pressure, while strong southeasterly winds are associated with increased air pressure.

Water temperature follows seasonal and daily trends, increasing steadily in the spring and decreasing steadily in the fall, with regular daily fluctuations due to solar heating. Both the seasonal and daily trends follow those of the air temperature data, but fluctuations are much smaller in magnitude in the water than in the air.

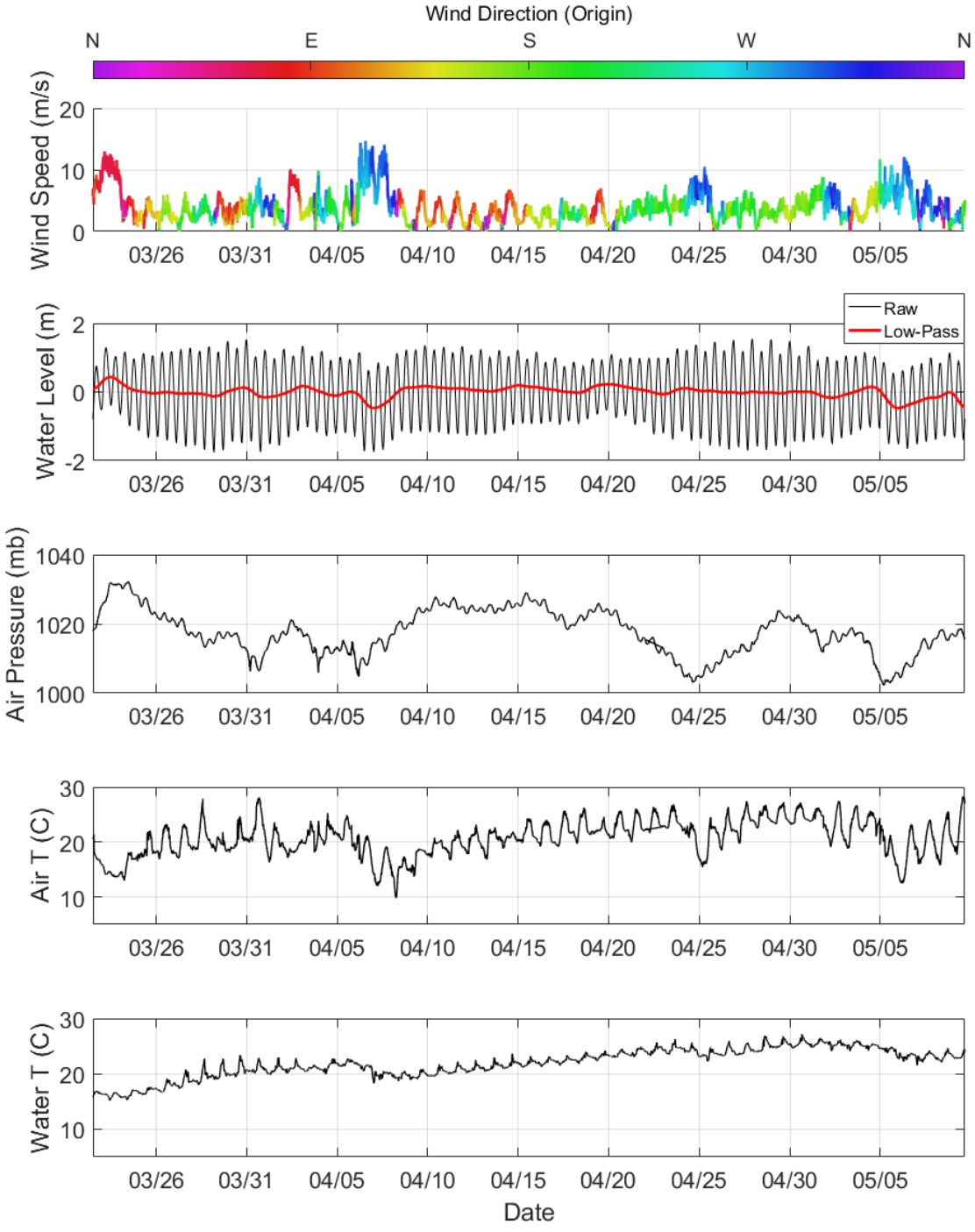

Figure 30: Spring deployment time series of meteorological conditions and the South Channel water level and water temperature. Wind conditions, air pressure, and air temperature were obtained from the NOAA Fort Pulaski observation station.

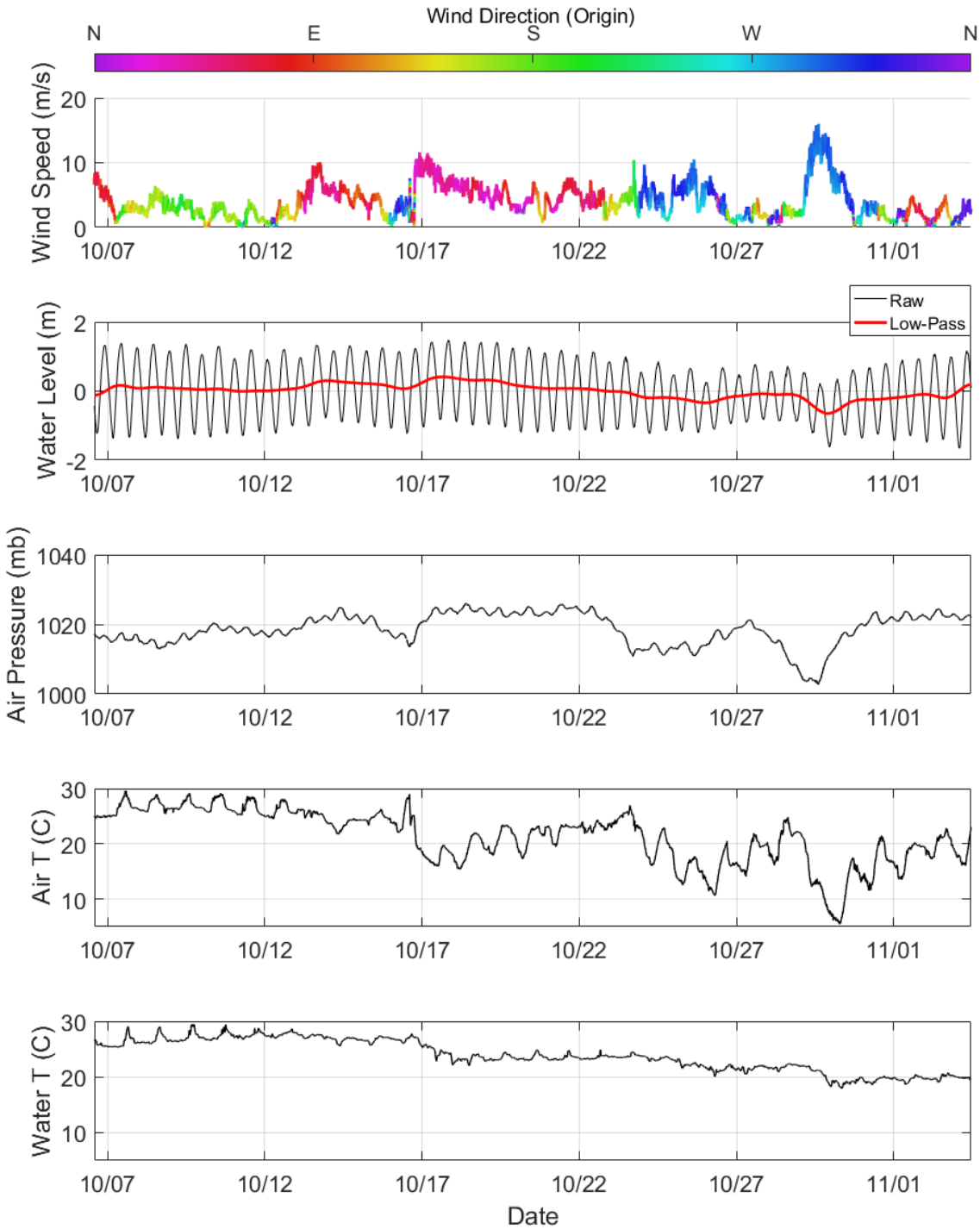

Figure 31: Fall deployment time series of meteorological conditions and the South Channel water level and water temperature. Wind conditions, air pressure, and air temperature were obtained from the NOAA Fort Pulaski observation station.

3.3 Hydrodynamic Model

The Regional Ocean Modeling System (ROMS) model was run for the period from October 1 through November 4, 2017. The model validation includes comparisons with the water level measured by the Aquadopps at Main Channel West, East, and the South Channel as shown in Figure 32. In general, the tidal signal is captured well in both phase and amplitude. The wind effects such as the drop or rise in mean water level during strong offshore or onshore winds are not totally captured. This may be due to the fact that the model domain does not extend far offshore. This may be alleviated in the future by extending the model domain or coupling to a larger scale ocean model.

The time series of the depth-averaged current from the model and measurements are shown in Figure 33. The overall magnitude of the current is captured reasonably well. The spring neap variability in magnitude and phase is well represented. The measurements do show some spikes in current velocity that is not seen in the model; however, this may be due to ship wake events occurring during the profiling period. This is only seen in Main Channel West where the ship wake is most prevalent.

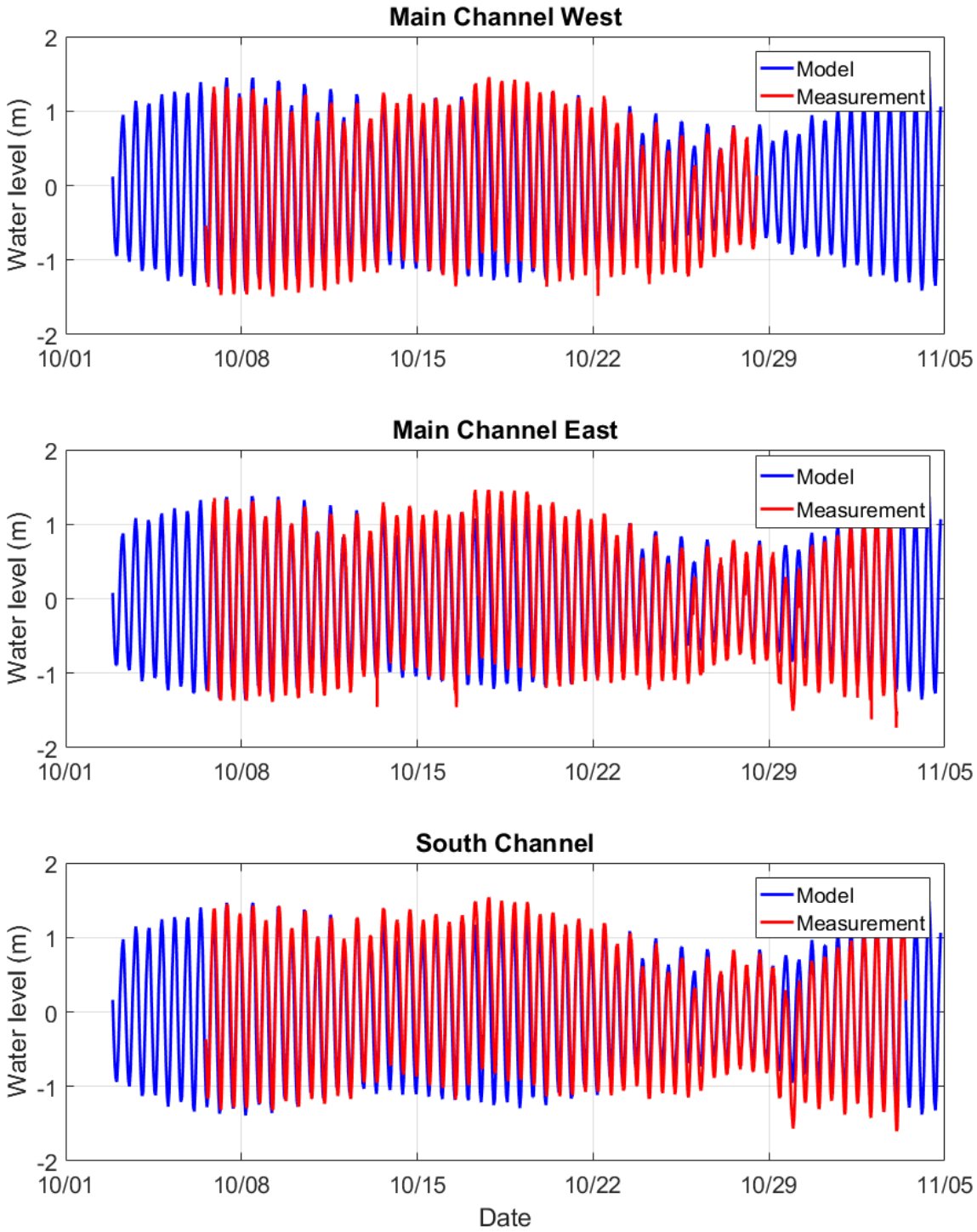

Figure 32: Water level data from the numerical model (blue) and Aquadopp (red) from the fall deployment in Main Channel West (top), Main Channel East (middle), and South Channel (bottom).

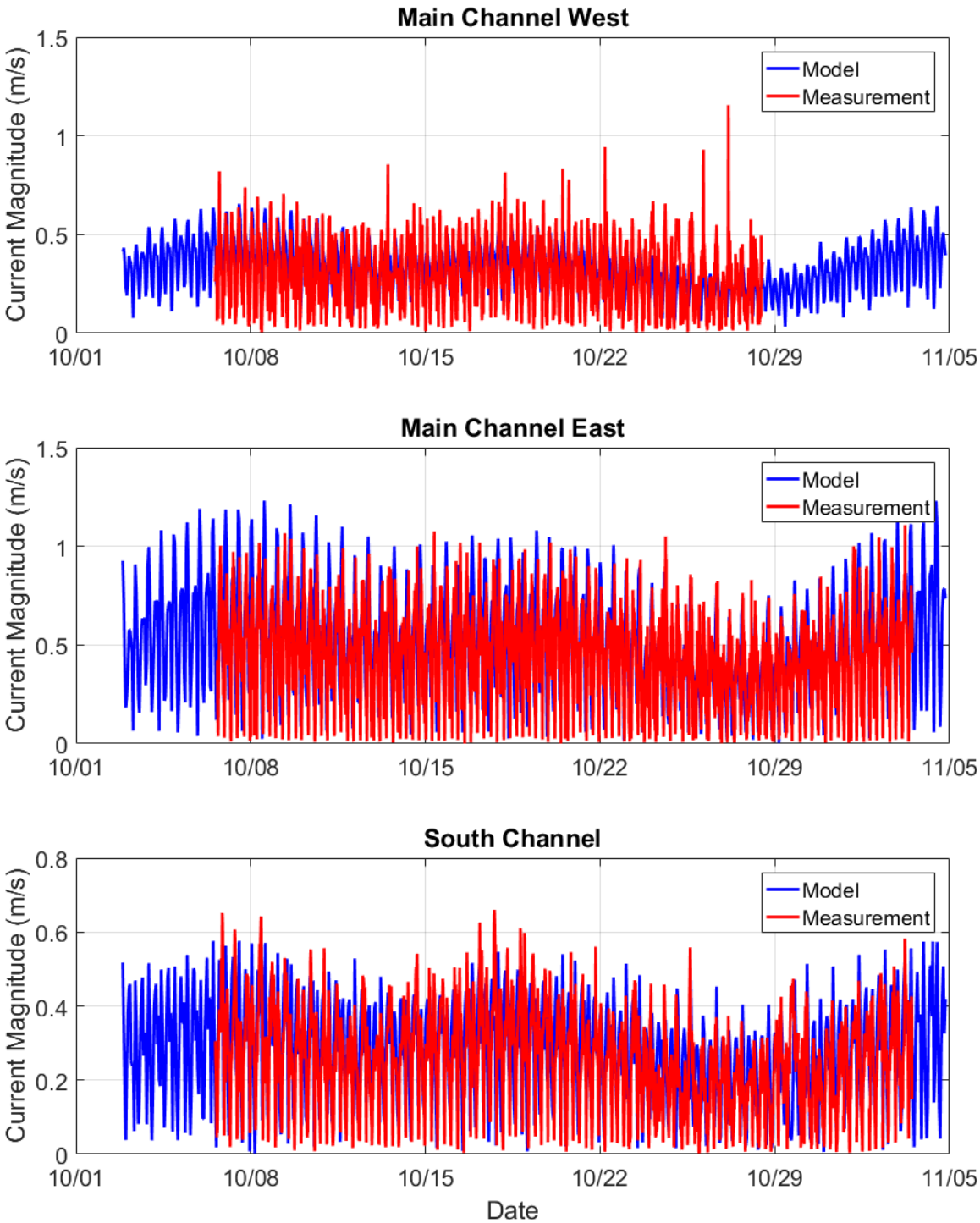

Figure 33: Depth-averaged current data from the numerical model (blue) and Aquadopp (red) from the fall deployment in Main Channel West (top), Main Channel East (middle), and South Channel (bottom).

3.4 Wind Waves

The significant wave height, $H_{mo,}$ and peak period, T_p, of the wind waves is determined for each wave burst in the Aquadopp. The duration and sampling schemes of the burst vary between deployments; the deployment parameters are detailed in Table 2 of *METHODS*. The histograms of $H_{mo,}$ and T_p from the spring data at Main Channel East and South Channel are provided in Figure 34; likewise, the histograms of the fall wind wave data from Main Channel East and South Channel are provided in Figure 35.

Overall, it is observed that wind waves were larger during the fall deployment than the spring deployment. Spring conditions typically have stronger winds, but no storm events occurred during the spring deployment. The maximum H_{mo} measured in the spring was 0.28 m at Main Channel East, while the mean at that location was 0.04 m, and the mean T_p was 2.2s. The maximum H_{mo} measured during that time at the South Channel site was 0.19 m, while the mean H_{mo} was 0.014 m, and the mean T_p was 2.1 s.

In the fall, the maximum H_{mo} in the Main Channel was 0.48 m, measured at Main Channel West. The mean H_{mo} for this site was 0.09 m, and the mean T_p was 2.1 s. Waves were smaller in the South Channel, with a maximum H_{mo} of 0.16 m, a mean H_{mo} of 0.015 m, and a mean T_p of 2.1 s.

Figures 36 and 37 show the time series of significant wave height along with the meteorological wind data for Fort Pulaski for the spring and fall deployments. These figures demonstrate that the increases in H_{mo} correspond very well to increased wind speed. When wind speeds are low, wind waves are lower as well, but the South Channel wind waves are particularly decreased.

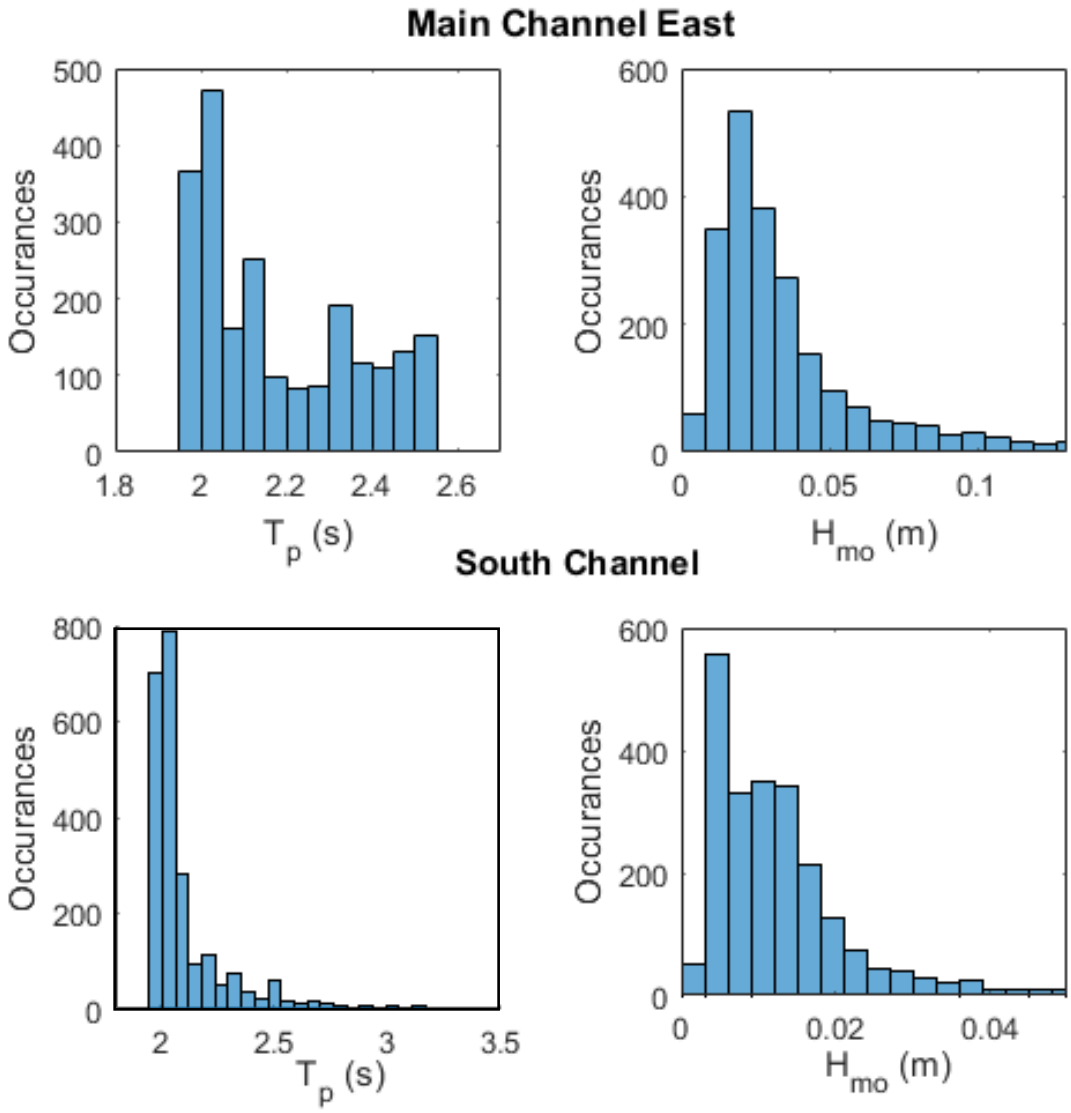

Figure 34: Peak period and significant wind wave height histograms from the spring deployments at Main Channel East and South Channel.

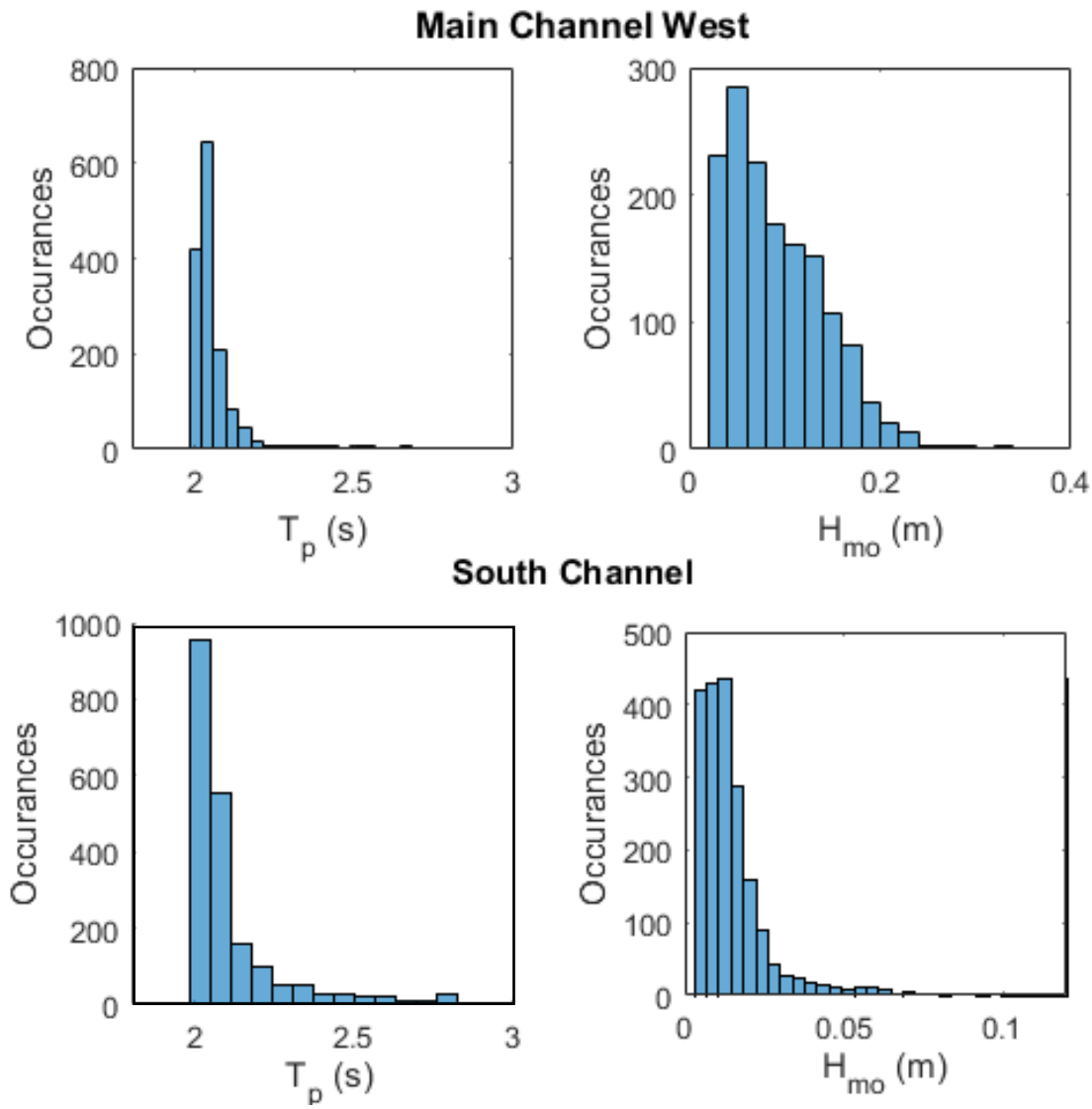

Figure 35: Peak period and significant wind wave height histograms from the fall deployments at Main Channel West and South Channel.

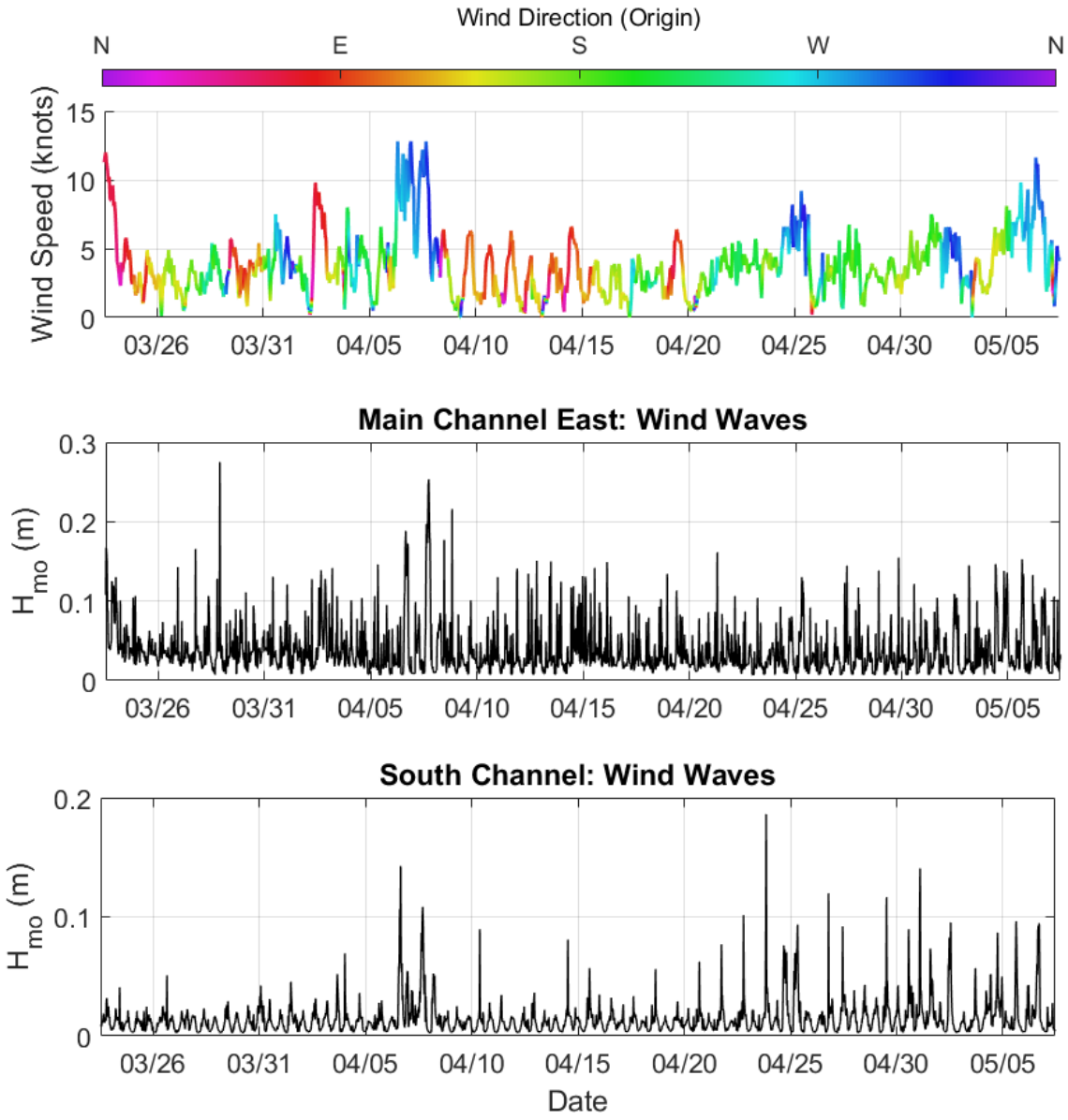

Figure 36: Time series of wind conditions and significant wave height at Main Channel East and South Channel during the spring Aquadopp deployment.

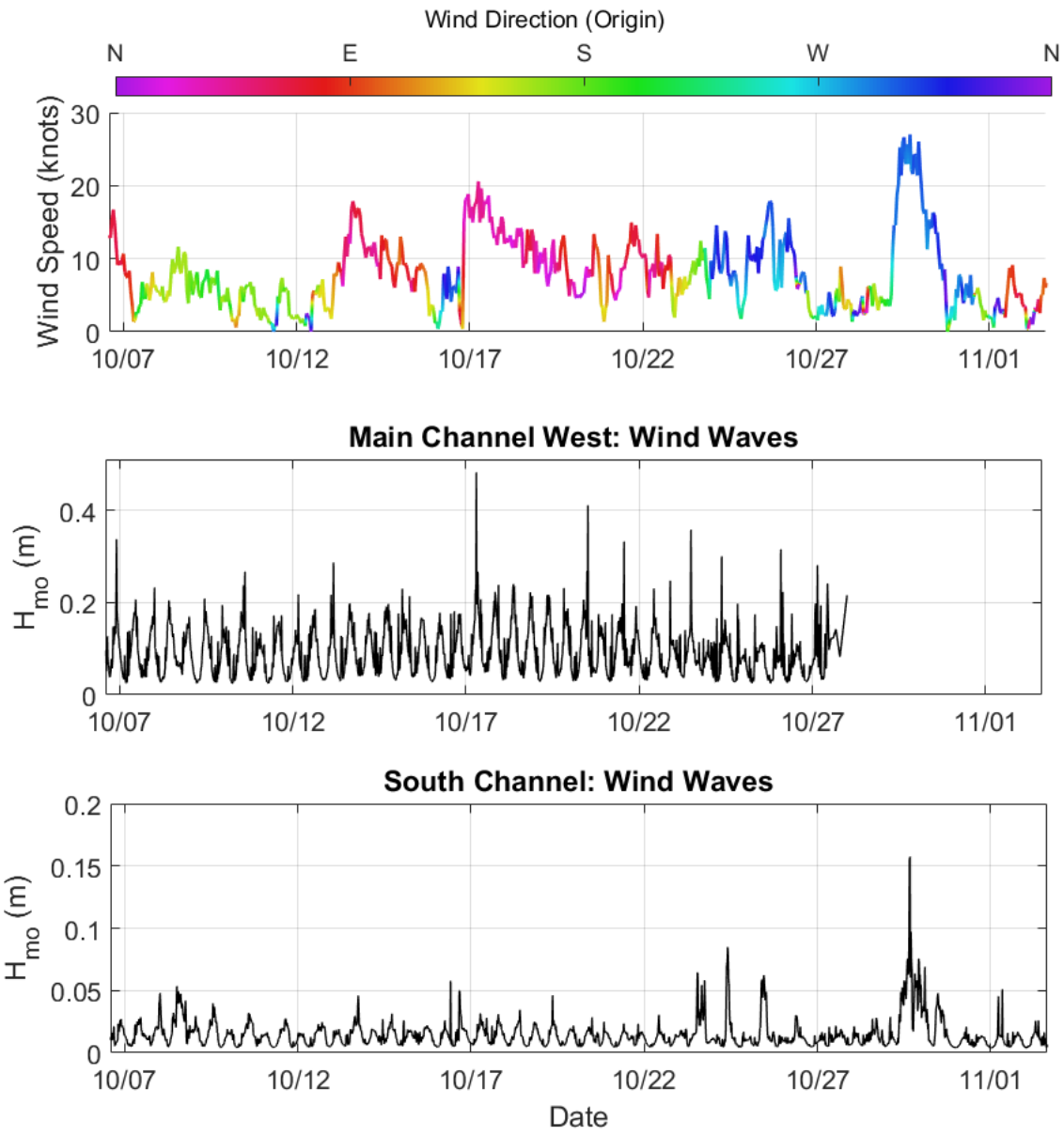

Figure 37: Time series of wind conditions and significant wave height at Main Channel West and South Channel during the fall Aquadopp deployment.

3.5 Wave Model

The Simulating Waves Nearshore (SWAN) model was run for the time span from October 1 through November 4, 2017. The significant wave height time series from the Main Channel West and South Channel locations are shown in Figure 38. Similar to the measurements, the waves are larger in the Main Channel than in the South Channel. However, the wave heights from the model tend to be larger than the observations indicate. This may be partially due to the fact that the locally generated waves are fairly high frequency waves and the attenuation over depth decrease the pressure signal observed by the Aquadopps.

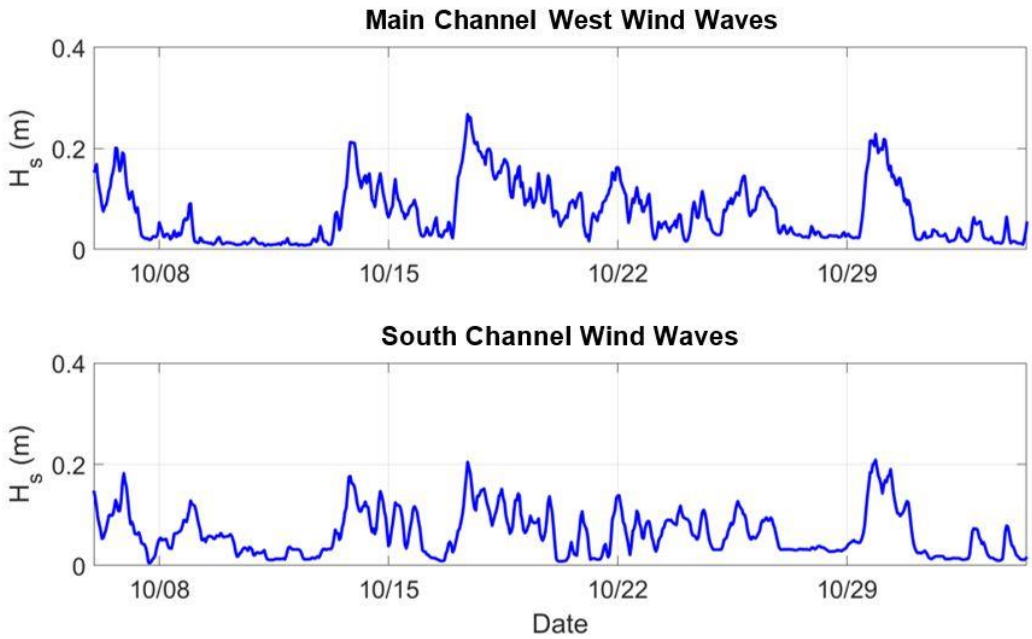

Figure 38: Time series of significant wave height from the SWAN model at Main West and South Channel during the fall Aquadopp deployment.

Figure 39 shows the spatial distribution of significant wave height during two different strong wind events on October 17 and 29. October 17 corresponds to wind coming from the northeast whereas October 29 corresponds to wind coming from the northwest. The larger waves coming from offshore are unable to enter the Savannah

River; therefore, the waves around Bird-Long Island are all locally generated by the wind. This results in much smaller wave heights relative to the waves in the vicinity of Tybee Island. However, for the northeast wind, larger waves are able to penetrate just inside the Savannah River entrance to impact Cockspur Island, partially illustrating the difference between the hydrodynamic environments around Cockspur versus Bird-Long Islands.

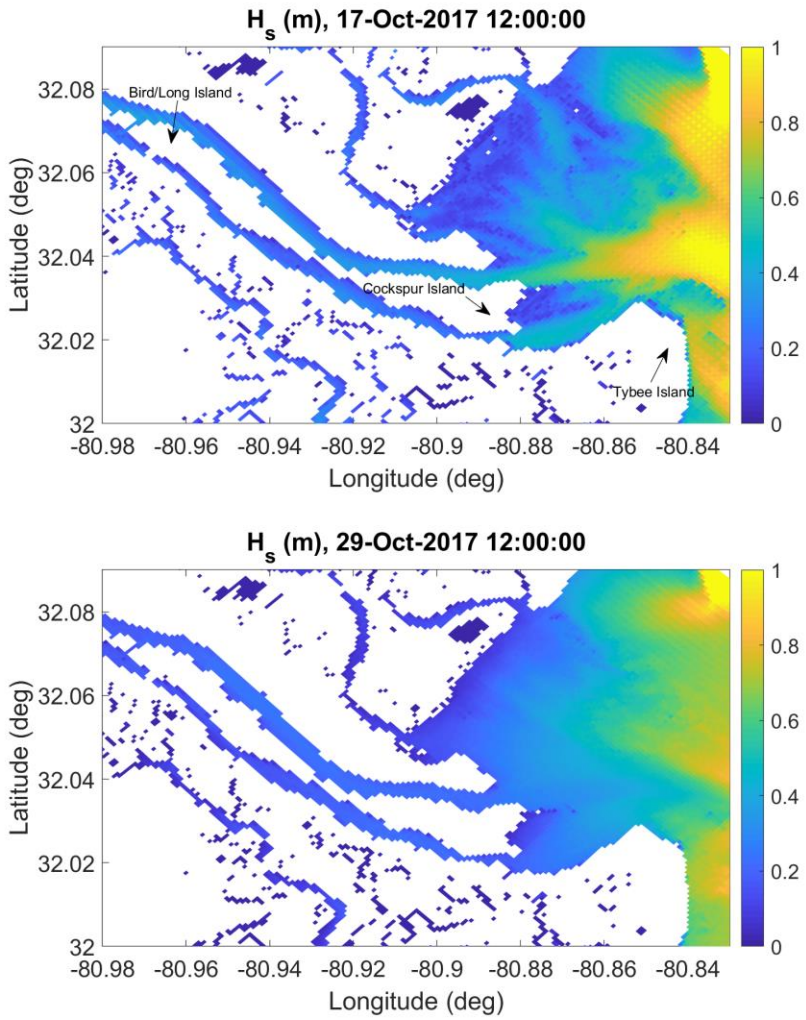

Figure 39: Snapshot of significant wave height on October 17, 2017 at 12:00 during a strong NE wind event (top) and October 29, 2017 at 12:00 during a strong NW wind event (bottom).

3.6 Large Vessel Traffic

Shipping traffic plays an important role in the hydrodynamics around Bird-Long Island as the Main Channel serves as a shipping channel for large commercial vessels transiting to and from the Port of Savannah. The region of the route near the island is passed by a wide variety of vessels, including container ships, cargo vessels, tugs, and pleasure craft. AIS data provides information for most large vessels that pass the island.

In the full year of 2016 AIS data, there were 6,470 vessel passages at Bird-Long Island; containerships account for 65% of these passages. The breakdown of total traffic by vessel type for vessels accounting for over 0.5% of the passages is given in Figure 40. The vessel types individually accounting for less than 0.5% of the traffic are sailboats, offshore supply vessels, commercial fishing vessels, and research vessels.

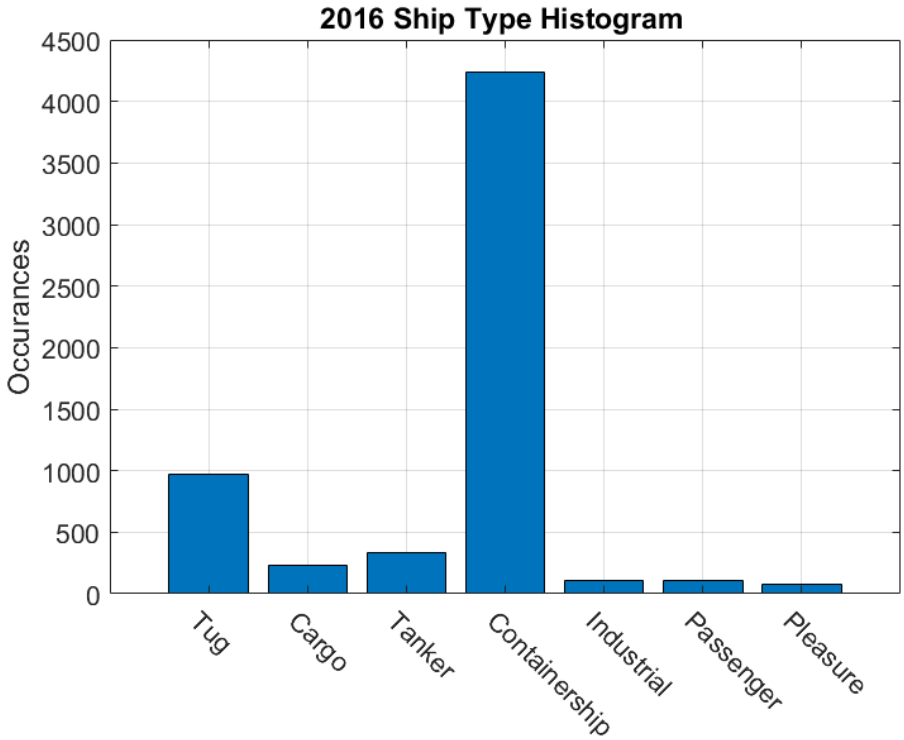

Figure 40: Histogram of vessel types in the 2016 AIS data for types individually accounting for greater than 0.5% of total traffic.

The mean, median, and range of the vessel lengths by ship are given in Figure 41. Cargo vessels, tankers, and containerships comprise the largest vessels, with mean and median lengths all greater than 150 m. In consideration of the size and passage frequency of the vessel types, cargo vessels, tankers, and containerships are considered for further analysis, with a particular emphasis placed on containerships. Collectively these vessels will be referred to as "large vessels."

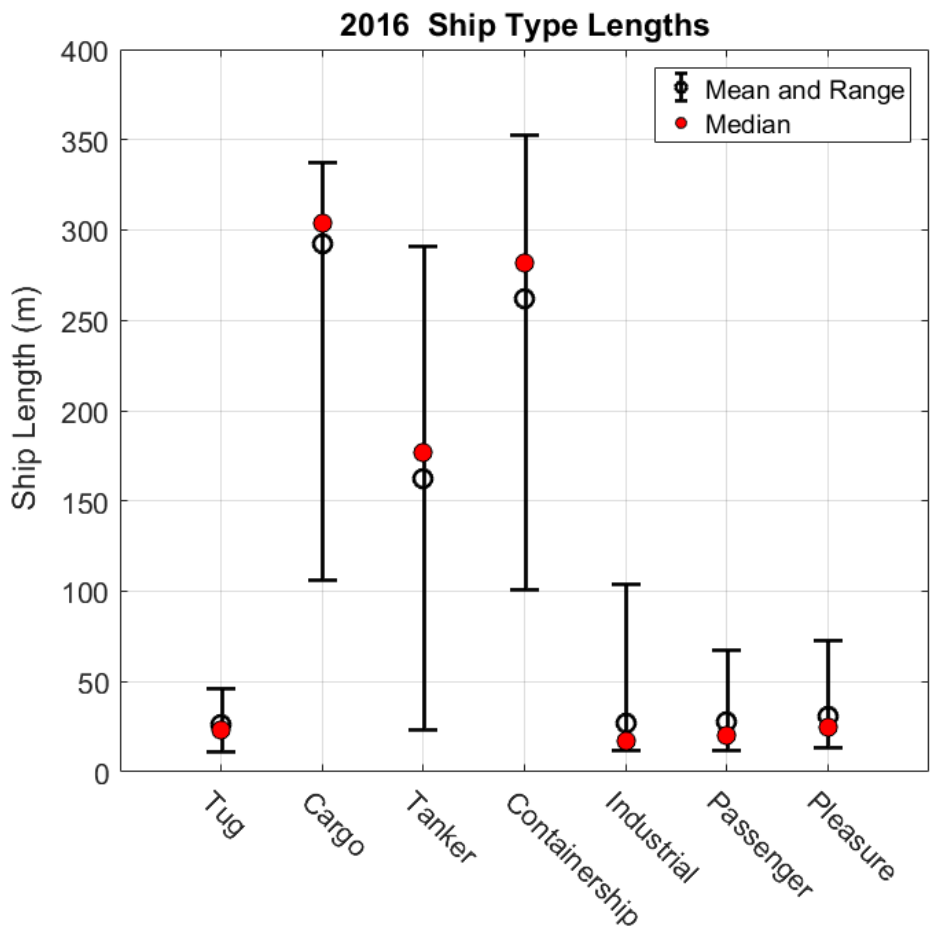

Figure 41: Mean (open black circle), median (solid red circle), and range (vertical lines) of vessel lengths for the vessels types in the 2016 AIS data individually accounting for greater than 0.5% of total traffic.

The speed of vessels varies significantly between vessel passages and along the length of the shipping channel. Histograms of large vessel speed in October 2017, which included 394 large vessel passages, for three sites are shown in Figure 42. At Main Channel West, the mean speed is 6.18 m/s, and the standard deviation is 0.83 m/s. Speeds are slightly slower at Main Channel East, where the mean speed is 5.9 m/s, and the standard deviation is 0.77 m/s. At Cockspur Island, mean speed is further reduced to 5.3 m/s, and the standard deviation is 0.75 m/s.

Figure 43 shows additional spatial information about the mean speed of large vessels along the shipping channel; this data was also obtained from the October 2017 AIS data. The speeds are analyzed separately for inbound ships, which travel northwest towards the port, and outbound ships, which travel southeast towards the Atlantic Ocean. For a given ship, AIS data is typically recorded every 5 minutes. To obtain the average speed along the channel, the channel length is divided into small discrete segments, and the speeds of large vessels recorded at locations within a small radius of a particular segment are averaged to determine a representative speed for that segment.

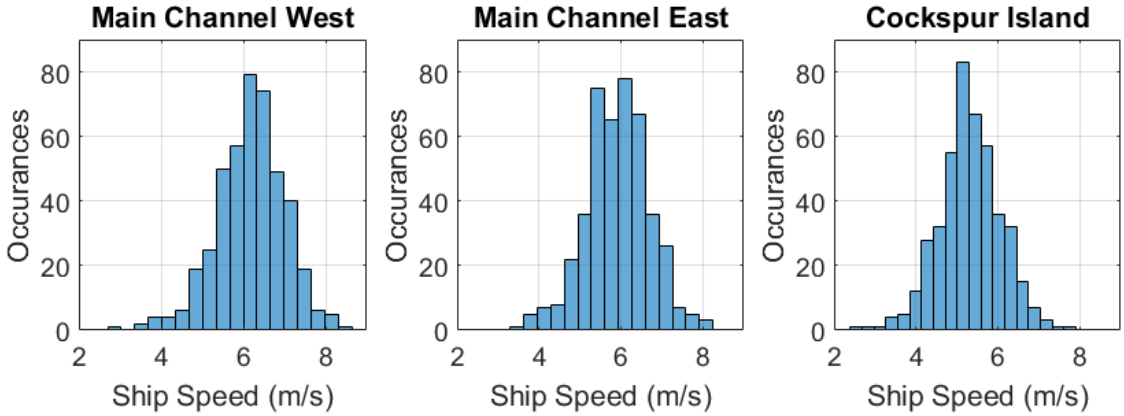

Figure 42: Vessel speed histograms at Main Channel West, Main East, and Cockspur Island.

Several features observed in Figure 43 are of note. For both inbound and outbound vessels, speeds are greatly reduced in the vicinity of Cockspur Island, which was also reflected in the histogram in Figure 43. This slowdown likely associated with the presence of a US Coast Guard Station with docks located on Cockspur Island, directly onshore from the center of the slowdown region. It is also observed that this slowdown extends into the region surrounding Main Channel East. For both inbound and outbound ships, mean speeds are increased as ships transit past Bird-Long Island. North of Bird-Long Island, outbound vessels coming out of the bend at 32.09° latitude and -80.99° longitude have the fastest mean speeds observed in the region of the Savannah River for which data has been collected. This increase is not observed for inbound vessels entering the bend.

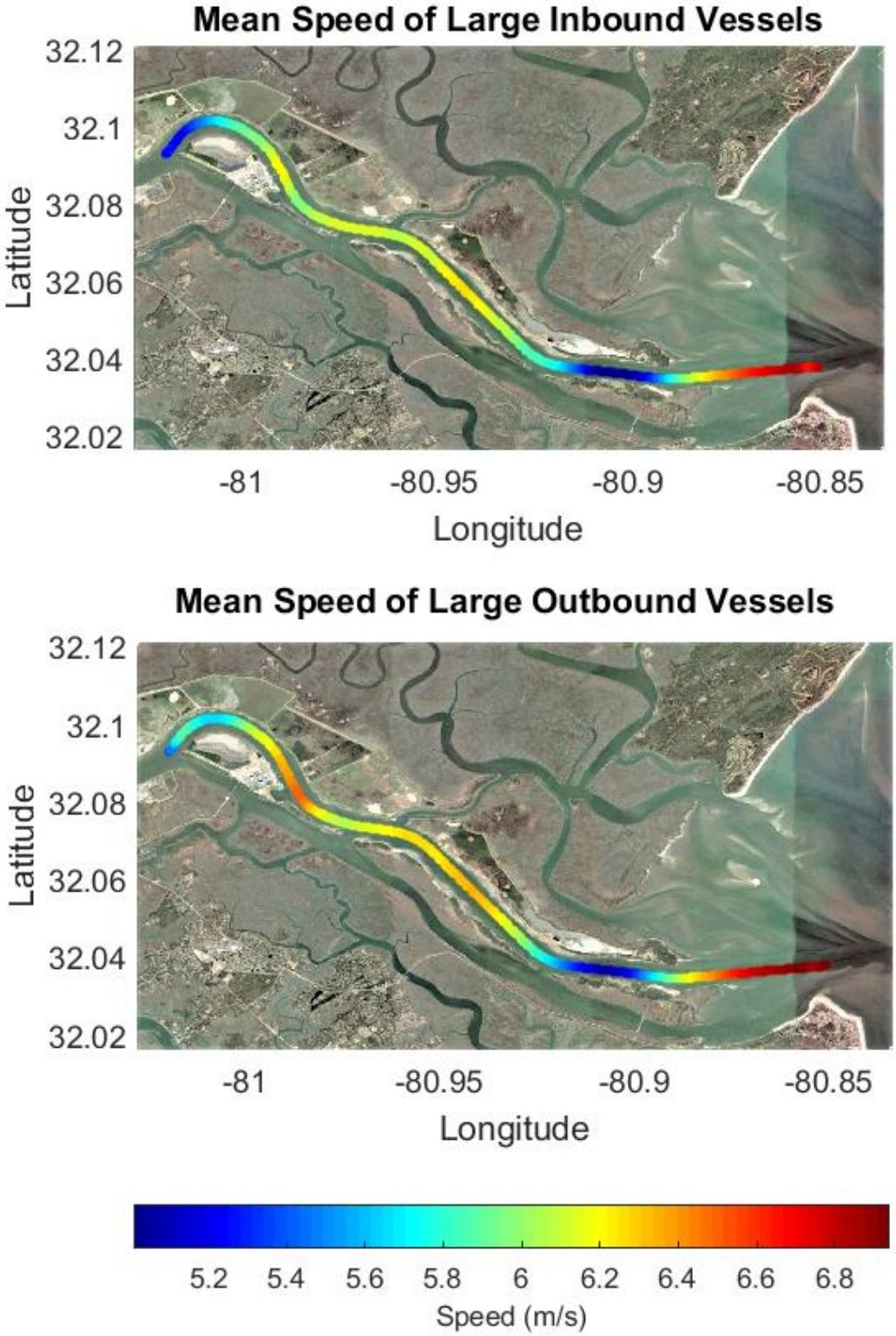

Figure 43: Mean speeds of large vessels along the shipping channel for (upper) inbound and (lower) outbound vessels.

3.6.1 Large Vessel Wake in the Main Channel

Figure 44 provides an example of a ship wake event at Main Channel West and its effect on the detided and low-pass filtered water level. The water level data was obtained from the wave burst data of the Aquadopp at Main Channel West, and the photographs were taken by the GoPro mounted at the shoreline of Main Channel West. As the ship initially approaches from downriver, there is a slow, steady rise in water level. As the ship gets nearer, the water level drops drastically before surging back onto the beach as the ship passes. The height of the surge often, but not always, exceeds the undisturbed mean water level. After the surge, additional waves of wake and seiching occur; these may persist for over an hour after the ship passes.

Large vessel wake events were identified in the Aquadopp and pressure transducer data sets using the photographs taken by the mounted camera. The pressure transducer and camera deployments ranged in duration from 23 to 48 hours and coincided with the beginning or end of the long term Aquadopp deployments. Since the Aquadopps are only able to capture wake events while in burst mode, which was not continuous, pressure transducer data was used to provide a continuous time series of the water level, capturing all wake events that occurred during the pressure transducer deployments. By pairing each photograph with a ship in the frame to the corresponding pressure transducer water level fluctuations, key defining characteristics of ship wake, such as those labeled in Figure 44, were identified. The direction of the ship was also noted from the photographs. When available, the Aquadopp data corresponding to a known ship passage was also analyzed; the characteristics were highly consistent in both instruments.

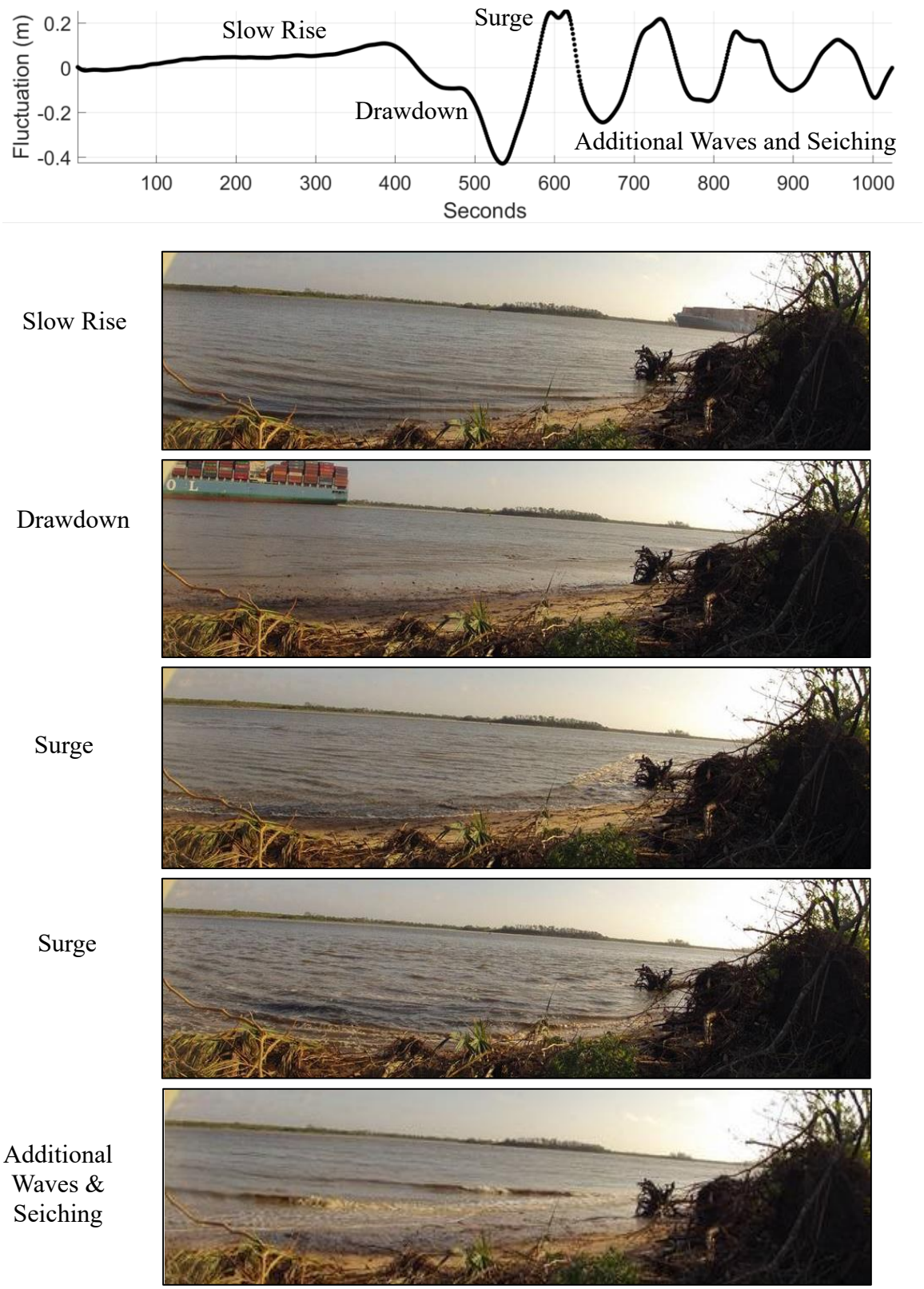

Figure 44: Wake event at Main Channel West with photographs of wake characteristics**.**

Figures 45 to 47 provide the water level time series data from the three pressure deployment periods in the Main Channel, with ship passage events identified in the camera images marked on the time series with vertical lines. In the August deployment, the camera was located at Main Channel East, so the August Main Channel East water level time series is plotted in Figure 45. Similarly, the camera was mounted at Main Channel West in the October and November pressure transducer deployments, so the October and November Main Channel West data are plotted in Figures 46 and 47, respectively. Camera battery failures affected the verification of ship events in the August and November data sets, but the deployment in October captured an unusually large number of large vessel wake events resulting from the weather-related closure of the port for several days prior to the deployment.

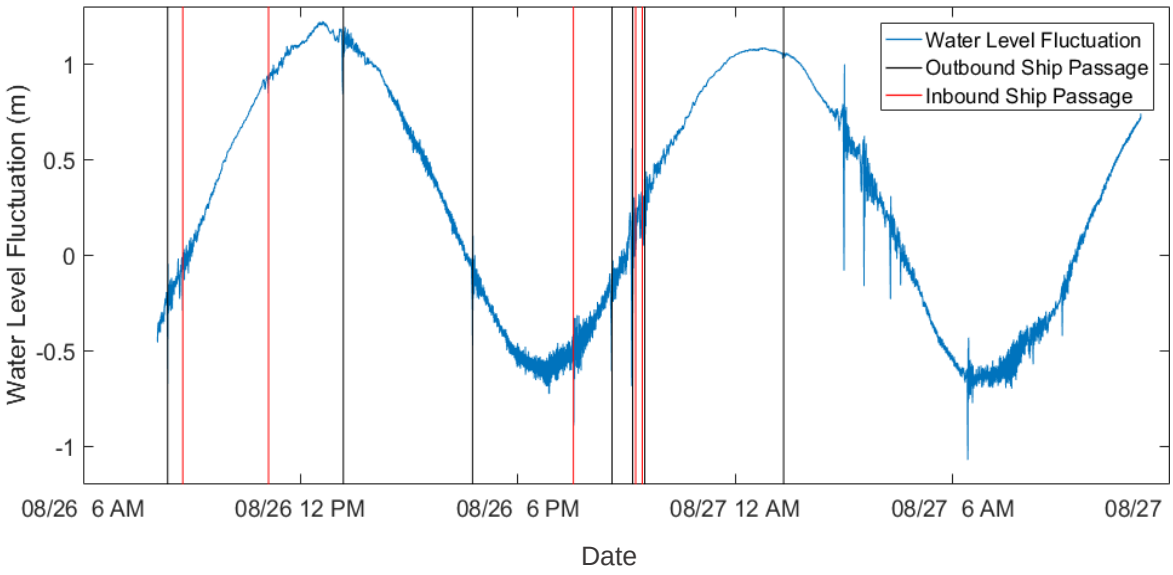

Figure 45: August Main Channel East pressure transducer water level data with times of photographed ship passage events. The lack of photograph-verified ship events after 08/27 2 AM is due to battery failure of the camera.

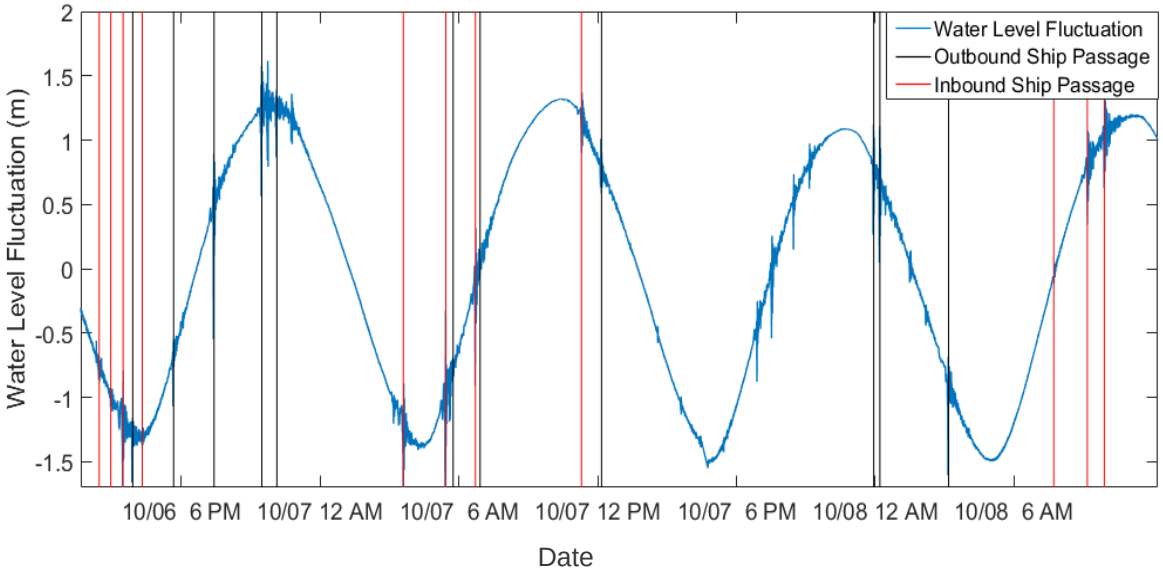

Figure 46: October Main Channel West pressure transducer water level data with times of photographed ship passage events. The abundance of ship passages is attributed to the closure of the port due to poor weather for several days prior to this deployment.

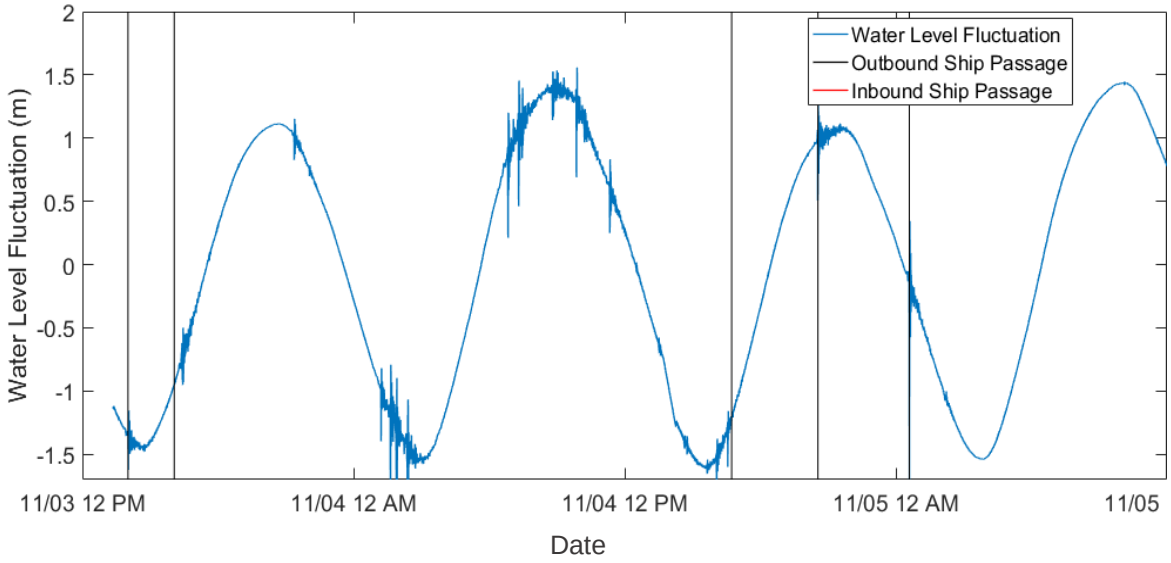

Figure 47: November Main Channel West pressure transducer water level data with times of photographed ship passage events. The lack of photograph-verified ship events between 11/03 6 PM and 11/04 12 PM is due to battery failure of the camera; the battery was replaced on 11/04 at 12 PM.

The identification of key large vessel wake characteristics, primarily the drawdown and surge, permitted the pairing of 217 wake events in the fall Main Channel West Aquadopp burst data with known ship passages in the AIS data. The fall Main Channel West data set was utilized because it is the most complete. For each passage event at this site identified in the AIS data, the surrounding 60 minutes of detided and low-pass filtered Aquadopp burst data were manually examined to find the burst data corresponding to the wake event from the beginning of the drawdown to the end of the surge. When the signature could be confidently attributed to a specific ship passage event, the ship characteristics available in the AIS data were paired with that particular wake event. Events where the signature could not be clearly identified were not analyzed at this time. These included cases when there were multiple large vessels near the site simultaneously, as occurs when an inbound and outbound ship pass in the channel, and the wakes could not be confidently attributed to the two ships, as well as cases when the ship wake signature was masked by persistent seiching from the previous wake event.

For the 217 paired events in the fall Main Channel West data set, the corresponding burst data is analyzed to ultimately attribute an energy value to the wake. Raw velocity is rotated into a downriver and cross-shore coordinate system; downriver velocity is positive in the seaward direction of the river, to the southeast, and cross-shore velocity is positive in the onshore direction, to the southwest. The velocity and pressure data of a burst is detided with a one-hour polynomial curve fit; this separates the data into tidal and fluctuating components. The tidal velocity component is the tidal current velocity $\vec{V}$, and the fluctuating velocity is $\vec{v}'$. The fluctuating component of the pressure is the dynamic pressure, P_D, and both components of pressure are retained to determine the

instantaneous water depth, h. The effects of wind waves and high frequency wake components are removed from the fluctuating velocity and pressure data using a low-pass filter with a 20-second cutoff period. With this applied, the retained fluctuating values are due to "mid-band frequencies," as they occur at higher frequencies than tidal components, but lower frequencies than wind waves. Finally, from the time series of these mid-band processed parameters, a time series of the instantaneous energy flux per meter shoreline for the burst due to mid-band frequencies, $E_{f,MB}$, is calculated by

$$E_{f,MB} = (\vec{V} + \vec{v}')(P_D + \frac{1}{2}\rho|\vec{v}'|^2)(h)$$

The energy flux magnitude $|E_{f,MB}|$ is obtained by taking the magnitude of the downriver and onshore components of $E_{f,MB}$. Figure 48 shows the water level during a wake event with data points colored by the magnitude of $E_{f,MB}$. This exemplifies the persistent trend that the peak energy flux values are attained in the drawdown and surge. For this reason, further analysis examines only the "initial wave," which is defined from the water fluctuation zero-downcrossing at the beginning of the drawdown to the zero-downcrossing following the end of the surge. This allows for more consistent analysis of the wake data, as the burst data captures only 17 of every 20 minutes, and wake events

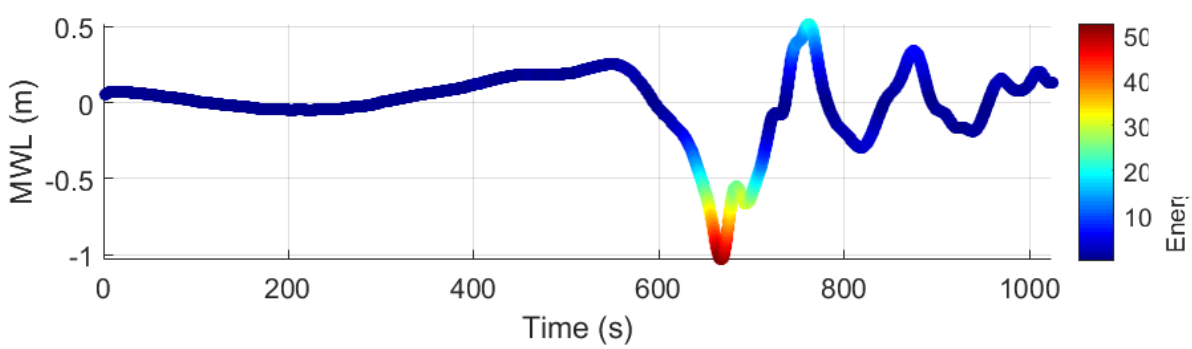

Figure 48: The energy flux time series over a typical large vessel wake event.

are rarely fully captured in one burst. Thus, by analyzing a relatively short but energetic portion of the time series, more events are able to be fully described and compared. Figure 49 shows an example burst time series of detided and low-pass filtered water level, velocity, and energy flux data with the initial wave identified.

The initial wave is first determined with a general zero-downcrossing method applied to the full burst containing the time of ship passage, but all events are manually inspected such that the wave may be redefined if necessary, such as in the case of multiple wakes occurring in a single burst. From the initial wave, then, several values are computed to characterize the wake. The peak energy flux is the maximum value of the energy flux magnitude, and the total energy of the initial is determined by time-integrating $|E_{f,MB}|$ over the wave period, and the peak energy flux magnitude is the maximum instantaneous value of $|E_{f,MB}|$ during the initial wave. The maximum fluctuations in the downriver velocity magnitude, onshore velocity, offshore velocity, and full fluctuating velocity magnitude are also determined. The wave period, wave height, lowest water level, and highest water level are recorded as well. These characteristics are labeled in a demonstrative time series in Figure 50, which spans the duration of the initial wave in the burst of Figure 49. The maximum wave height recorded in the Main Channel is 2.01 m, and histograms of key characteristics for large vessel passages, which comprise 176 of the 217 analyzed events, are shown in Figure 51.

When paired with ship characteristics from the AIS data and numerical model data, a wide variety characteristics are available for the initial wave event of each wake; these are listed in Table 14.

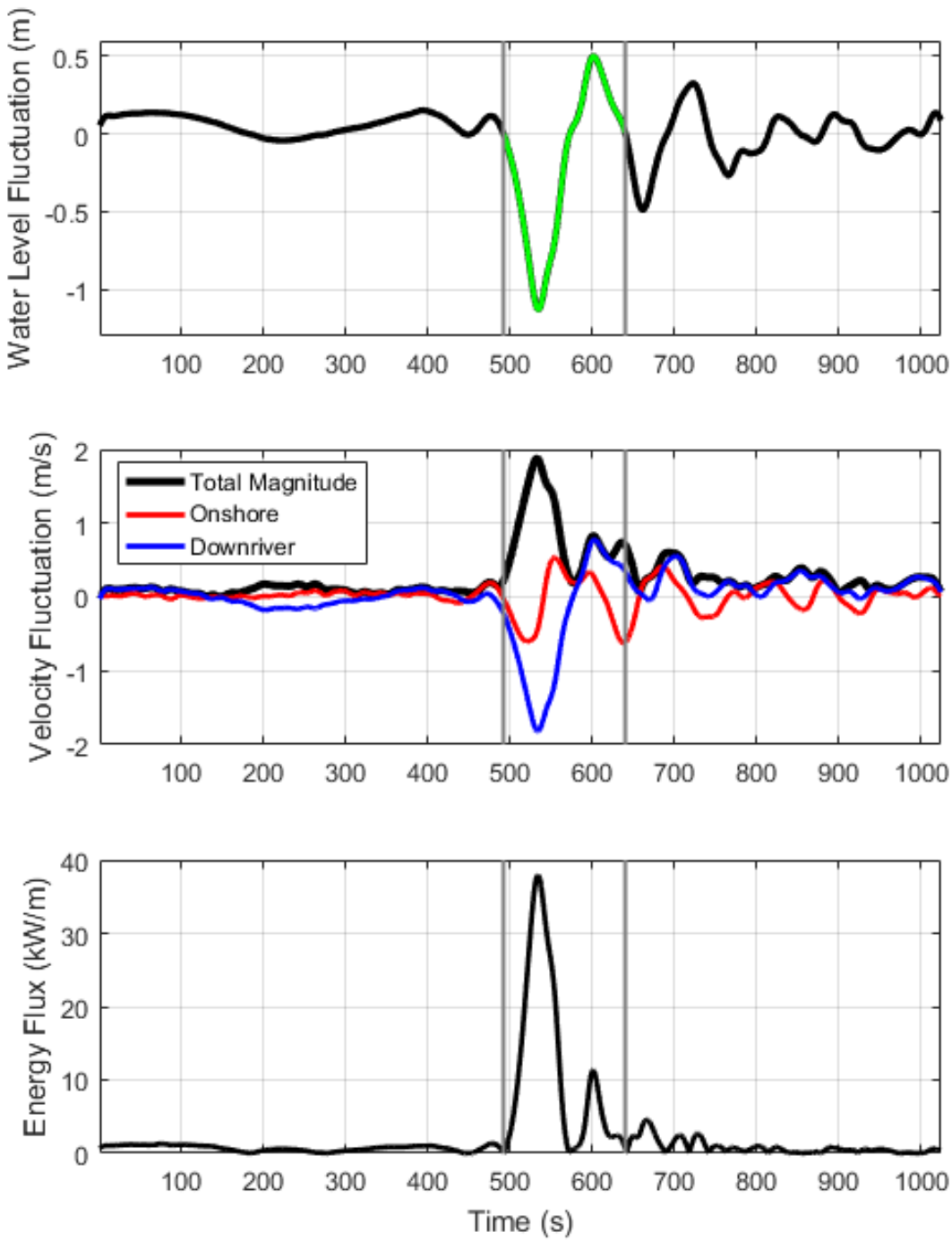

Figure 49: Time series data for a sample burst containing a wake event: the detided and low-pass filtered (upper) water level and (middle) velocity, and the (lower) energy flux calculated from these parameters. The initial wave is bounded by the vertical gray lines and examined further in Figure 50.

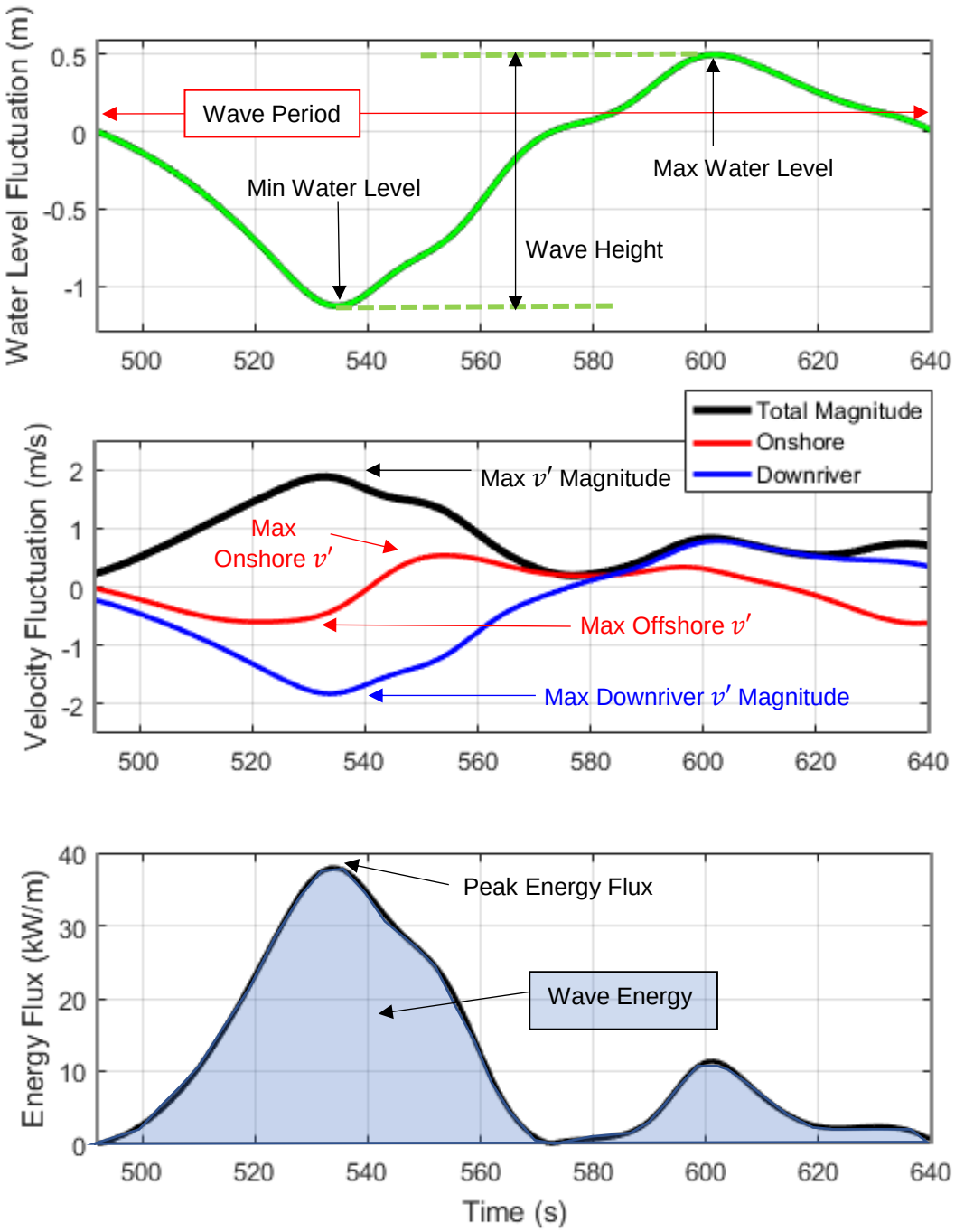

Figure 50: Time series data for a sample initial wave from the burst in Figure 49: the detided and low-pass filtered (upper) water level and (middle) velocity, and the (lower) energy flux calculated from these parameters. Key characteristics are labeled.

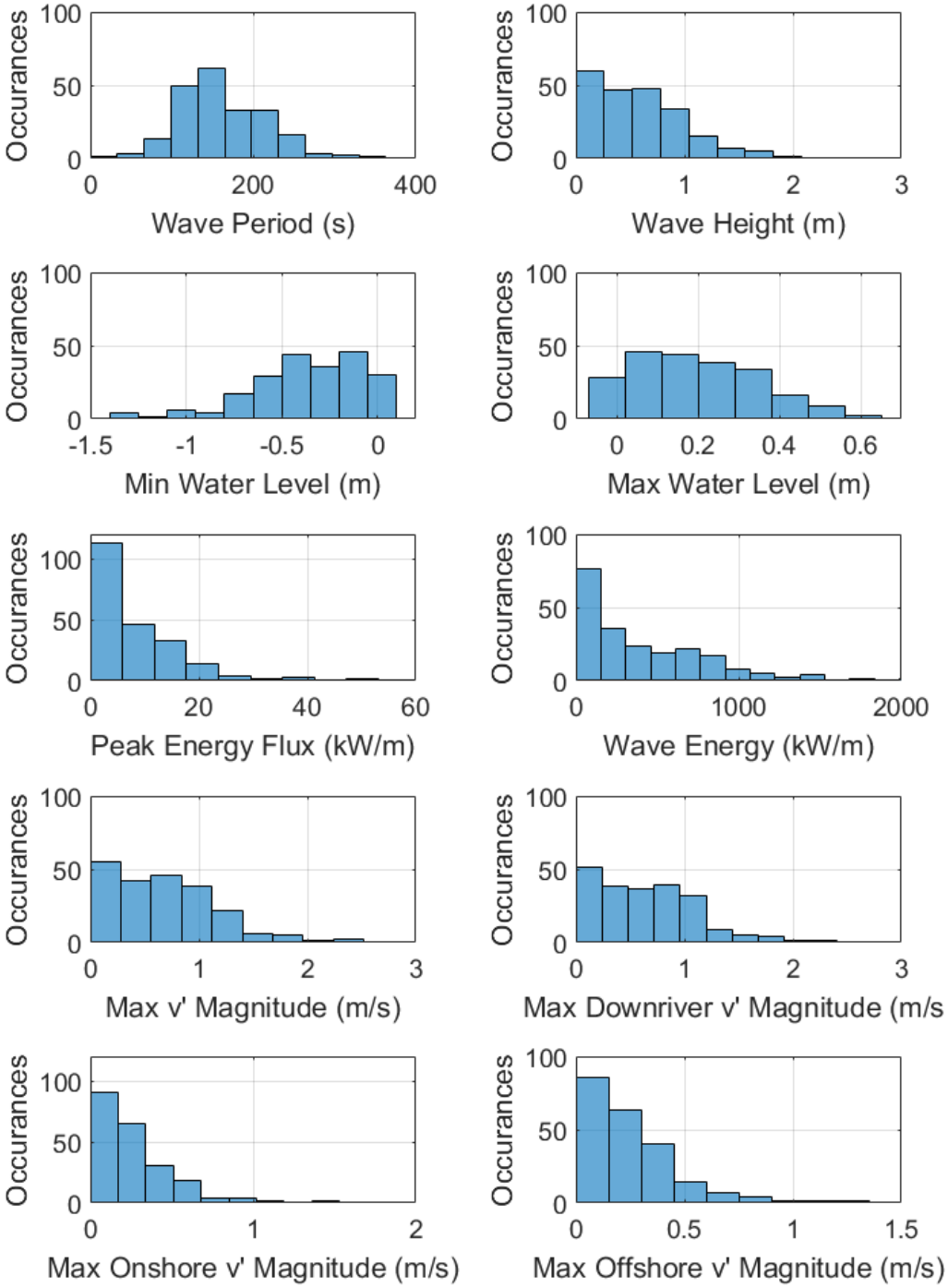

Figure 51: Measured initial wave characteristic for 176 large vessel wake events measured at the Main Channel West site in the fall Aquadopp deployment. Energy flux and Energy flux values are given per meter shoreline.

Table 14: Ship Wake Event Characteristics by Source

Ship Characteristics (source: AIS data)	**Wake Initial Wave Hydrodynamic Characteristics (source: Aquadopp burst data)**	**River Hydrodynamics (source: model data)**
Cargo Type	Wave Height	Downriver Current Velocity in the Shipping Channel
Heading	Wave Period	Onshore Current Velocity in the Shipping Channel
Call Sign	Initial Wave Energy	Velocity Magnitude in the Shipping Channel
Draft	Peak Energy Flux Magnitude	Tidal Water Level in the Shipping Channel
IMO Number	Maximum Downriver Velocity Fluctuation	
Direction (Inbound/Outbound/Other)	Maximum Crosss-shore Velocity Fluctuation	
Latitude	Maximum Velocity Magnitude Fluctuation	
Longitude	Lowest Water Level Fluctuation	
Length	Highest Water Level Fluctuation	
MMSI		
Vessel Name		
Absolute Ship Speed		
Relative Ship Speed		
Vessel Type		
Vessel Width		

Theoretical relationships have been established between vessel properties and their wake characteristics for idealized scenarios, but observations do not have significant correlations with these relationships. This indicates that complexities in the bathymetry and hydrodynamics of this site have significant impacts on the size and energy of ship wake which are not currently understood.

3.6.2 Large Vessel Wake in the South Channel

Ship wake propagates from the Main Channel into the South Channel, where it may be identified by low frequency fluctuations in the water level, velocity, and/or energy flux time series; the energy flux for the South Channel is calculated by the method described in Section 3.6.1. However, the fluctuations in these time series do not produce a recognizable signature response as was observed in the Main Channel, shown in Figure 48. In the South Channel, a single ship passage event may excite a response in the South Channel that presents as an increased energy flux for up to an hour, but this response is not as reliably periodic as the seiching observed in the Main Channel.

To aid interpretation of the South Channel's complicated response to ship wake, an additional field study was conducted in November, 2018 to measure the propagation of ship wake into the South Channel. Pressure transducers and an Aquadopp were deployed at sites A, B, C, and D (Figure 52), spanning the length of the South Channel along Bird-Long Island. Site B is also the South Aquadopp site of previous deployments. AIS records for the deployment period were obtained from an online database.

Pressure data time series from these instruments are compared with AIS records of ship traffic during the deployment to examine the water level response to ship wake at the multiple sites. It is assumed that, regardless of vessel direction, ship wake propagates into the South Channel from two entrances at the ends of Bird-Long Island: the West Entrance, which lies along the Intracoastal Waterway, and the East Entrance, which is the blowout between Bird-Long Island and Cockspur Island. The time at which the wave entering from either entrance reaches one of the instrumented sites is predicted using the

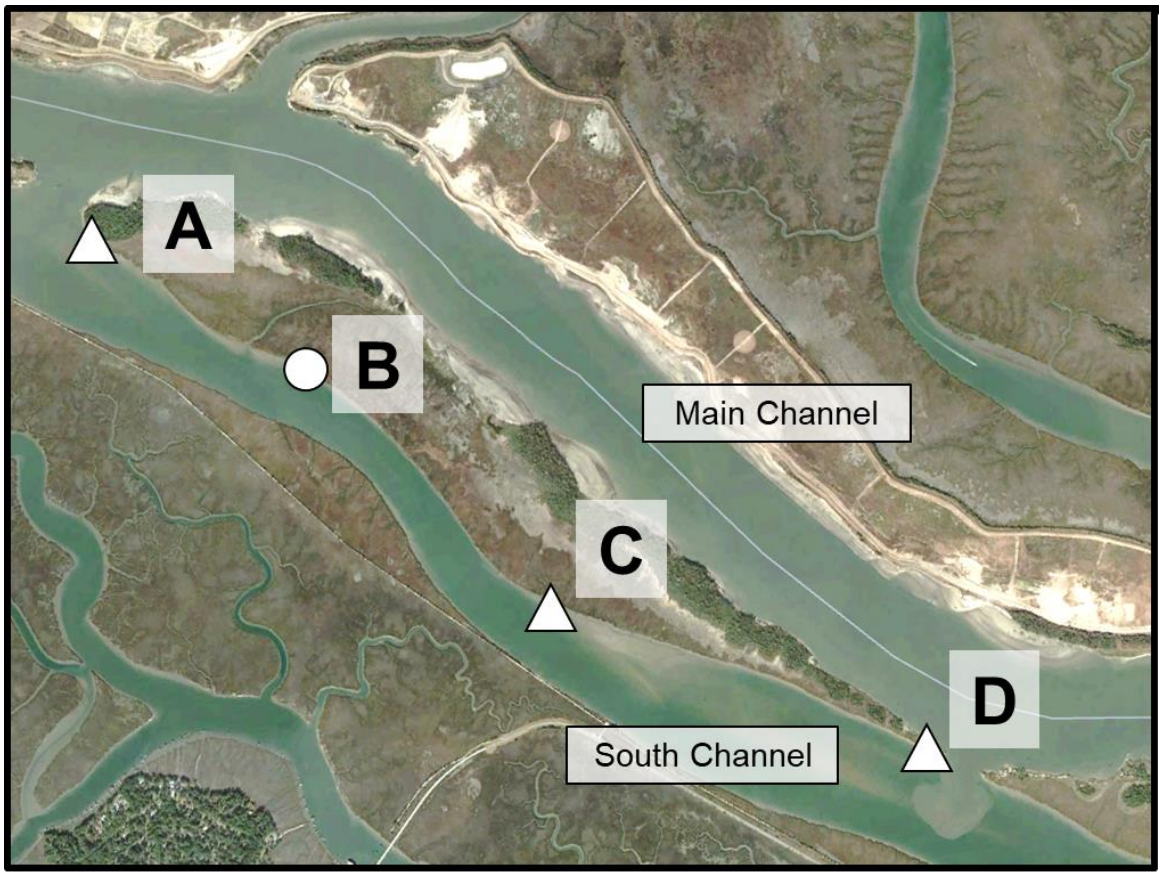

Figure 52: Instrument deployment locations for the November 2018 fieldwork measuring the propagation of ship wake in the South Channel. Pressure transducers were deployed at sites A, C, and D, and an Aquadopp was deployed at Site B.

AIS data and linear shallow water wave theory. Specifically, the time and location AIS data points of a particular ship passage are linearly interpolated to the line of the shipping channel, providing an estimate of the time at which the vessel transits any point along the channel. The times at which the vessel passes the East and West entrances are obtained from this data and utilized as the "start" times of the two waves; the first wave to enter the South Channel is referred to as the "first wave," while the second is referred to as the "second wave." For an inbound ship, the first wave is produced near the East Entrance, and the second wave is produced at the West entrance. The reverse is true for an outbound ship. Based on the Main Channel ship wake data, it is assumed that the wake

propagates into shallow water one minute after the ship passes directly offshore. From this point in time, it is modeled as a shallow water wave, as the South Channel has a mean depth of approximately 6 m, and the periods of the waves propagating the South are several minutes. Taking into account the tidally-varying water level and current, shallow water linear wave theory is used to estimate the celerity of the wave. The celerity is paired with estimated distances from the entrance where the wave enters the South Channel to the instrumented sites to predict the arrival time of the wave at each site.

Figure 53 provides the water level time series from the four sites with the predicted arrival times of the waves produced by an outbound containership with a length of 323 m, the GSL Ningbo. The predicted wave arrival times correspond sufficiently well to fluctuations in the water for this hydrodynamic response to be attributed to the vessel. Because this ship is outbound, its first wave enters the South Channel at the West Entrance, nearest Site A. It then propagates to sites B, C, and then D. At Site D though, it interacts with the second wave entering through the East Entrance. The resulting response form cannot be distinguished into two distinct waves and instead represents the interaction of both the first and second wave. This interaction at the East Entrance is a common feature for the wake response of outbound ships, and is a result of the coincidence that the first wave propagates the South Channel at roughly the same speed as the vessel transits the length of Bird-Long Island.

Figures 54 shows an example of the predicted arrival times and the measured water level time series for all four sites for the wake of an inbound vessel, Cosco Development, a containership with a length of 366 m. It is of note that this class of vessel, the Ultra Large Container Vessel (ULCV), is presently the largest class transiting

the channel. The figures shows that the predicted arrival times of the wake produced by the ship correspond well to fluctuations in the water levels. Because the ship is inbound, the first wave enters near at the East Entrance, nearest Site D, and then propagates up the channel. However, at Site A, it is met by the second wave, and the responses from the two waves cannot be distinguished. This is a common features of the inbound wakes at Site A, and it is also frequently the case at Site B.

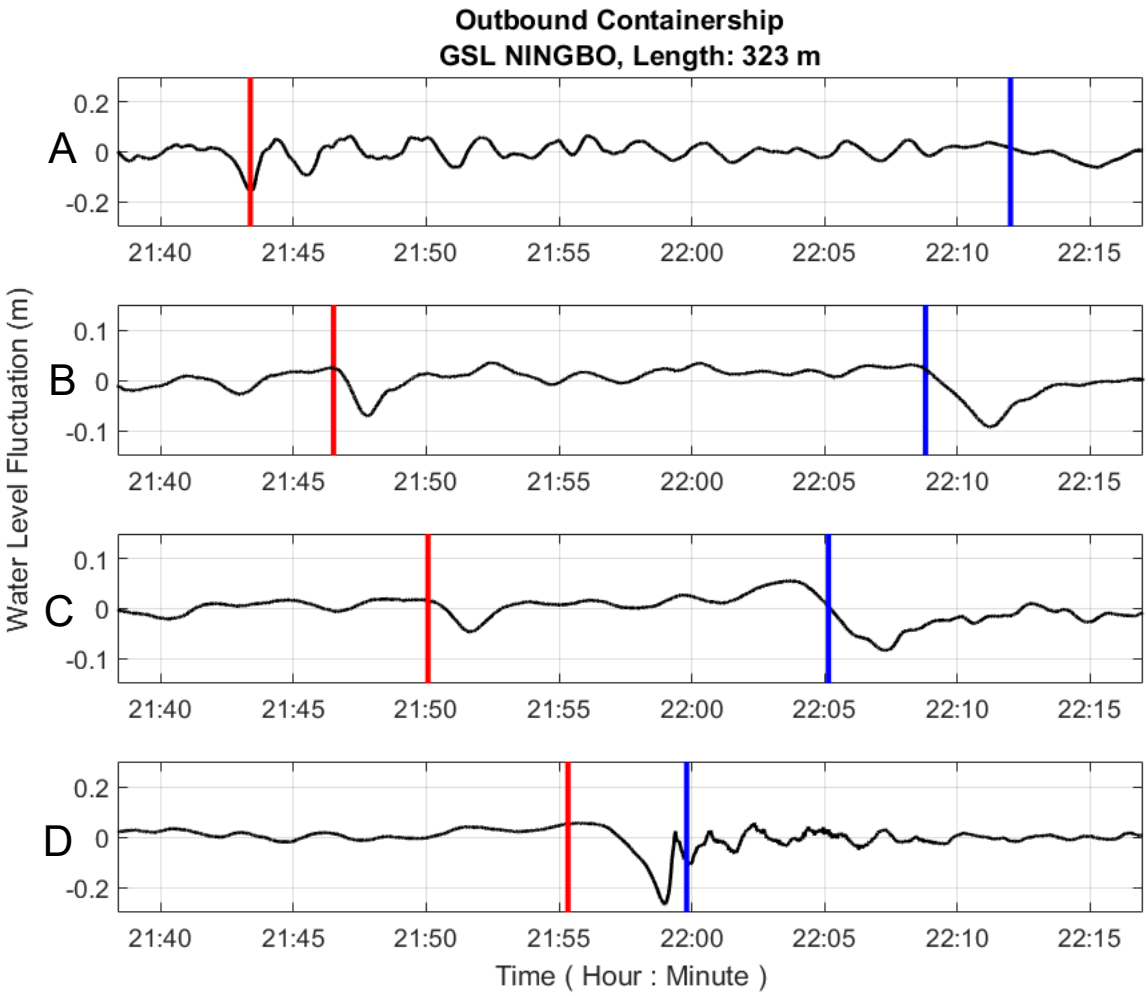

Figure 53: Water level time series of Sites A, B, C, and D with predicted arrival times of the first wave (red) and the second wave (blue) for the outbound passage of GSL Ningbo.

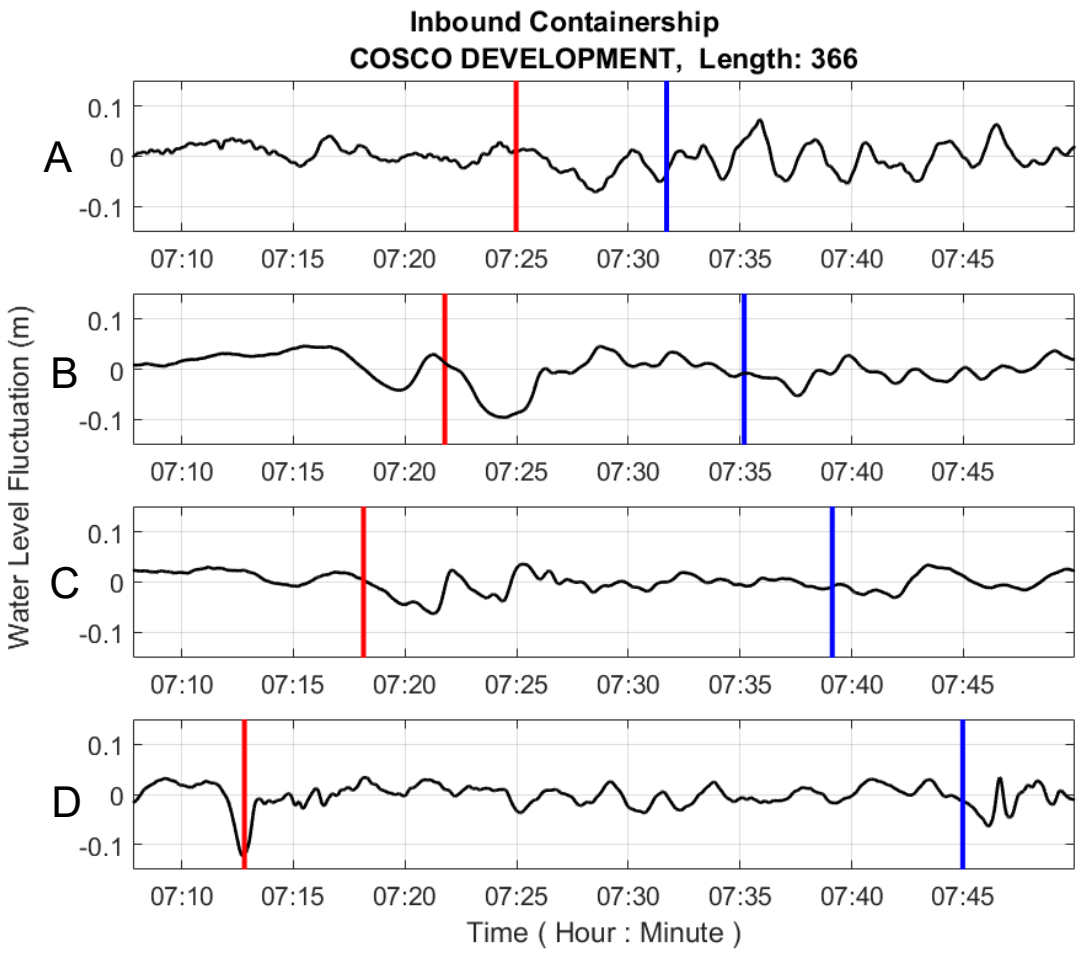

Figure 54: Water level time series of Sites A, B, C, and D with predicted arrival times of the first wave (red) and the second wave (blue) for the inbound passage of Cosco Development.

This study of wave propagation produced several conclusions which influence the analysis of the 2017 South Channel Aquadopp data. First, both inbound and outbound ships may produce two wakes that propagate the full length of the South Channel along Bird-Long Island. This implies that each site along the southern shore of the island may be affected by two waves produced by a single ship passage. It was also recognized that the two waves produced by an outbound shop should be distinguishable at Site B, but the two waves produced by an inbound ship may not be distinguishable at this site.

These conclusions were used to pair ship passages from AIS data to wake

responses in the South Channel Fall 2017 Aquadopp data, located near Site B. Aquadopp data was processed by the same procedure used for the analysis of Main Channel ship wake. AIS data was used in conjunction with tidal water level and current data to estimate the arrival times of the two waves produced by each large vessel passage at the Aquadopp site. A histogram of the delay between the two waves (Figure 55) demonstrates a clear distinction between inbound and outbound vessels. For outbound vessels, the second wave is predicted to arrive 18 to 34 minutes after the first wave, but for inbound vessels, the second wave arrives within 15 minutes of the first. In some cases, the second wave may reach the Aquadopp first, if an inbound ship is traveling particularly fast on a flood current. For this reason, only responses for outbound ships are distinguished into two waves. The response for inbound ships is determined for the "combined waves."

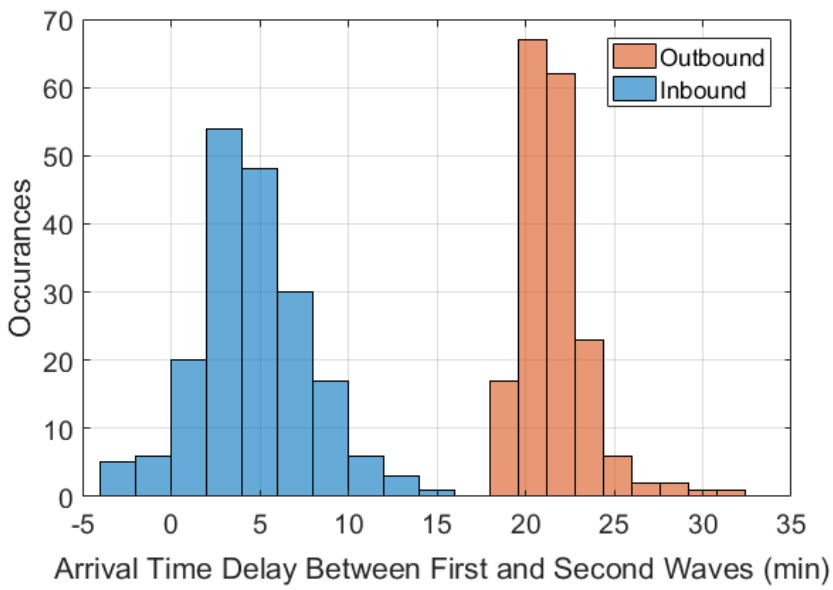

Figure 55: Histogram of the arrival time delay at the South Channel Aquadopp between the first and second waves for inbound (blue) and outbound (orange) ships. Negative delays indicate that the second wave is predicted to arrive before the first wave.

Figure 56 shows an example of the distinction between the first and second waves of an outbound ship in the Aquadopp burst data. The predicted arrival time is used to find a sharp decrease in water level; this is used to identify the wave. A five minute buffer is applied on either side of this low point. Within the resulting ten-minute window, the following characteristics are recorded for the wave: highest water level, lowest water level, peak energy flux, peak velocity magnitude fluctuation. The Aquadopp data is processed by the same procedure used for the Main Channel ship wake. The procedure is repeated for the second wave, and its characteristics are recorded separately.

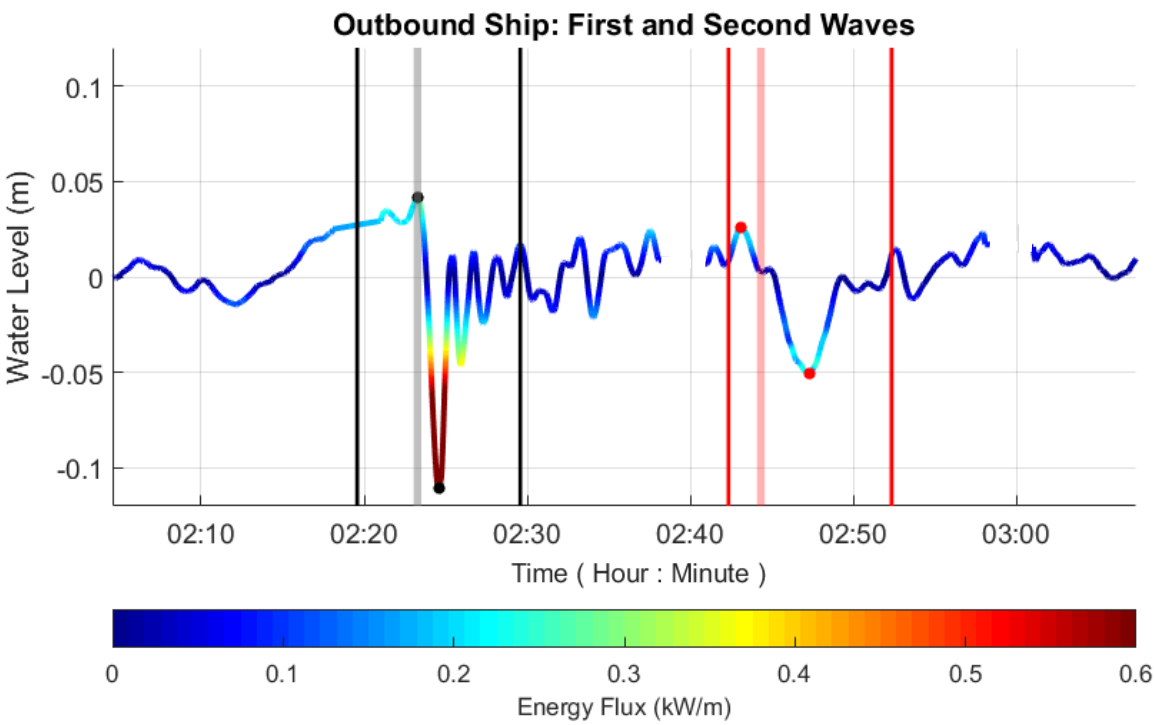

Figure 56: Water level and energy flux time series capturing the arrival at the South Channel Aquadopp site of the first and second waves from an outbound ship. The thick grey line indicates the predicted arrival time of the first wave, while the two thin black lines bordering it mark the bounds between which characteristics of the first wave are measured. Similarly, the thick pale red line marks the predicted arrival time of the second wave, and the thin red lines bordering it mark the bounds between which its characteristics are measured. Solid dots mark the extreme water levels for each wave.

Figure 57 demonstrates the method for determining characteristics of the combined waves produced by an inbound ship. The arrival time predictions of the two waves, indicated by thick vertical lines, show that the waves are expected to arrive within ten minutes of each other, and their responses interact such that they cannot be easily distinguished. Thus, the region in which wave characteristics will be recorded is extended five minutes before the predicted arrival of the first wave, and five minutes beyond the predicted arrival of the second wave. The characteristics recorded are the same as those described for the outbound ship.

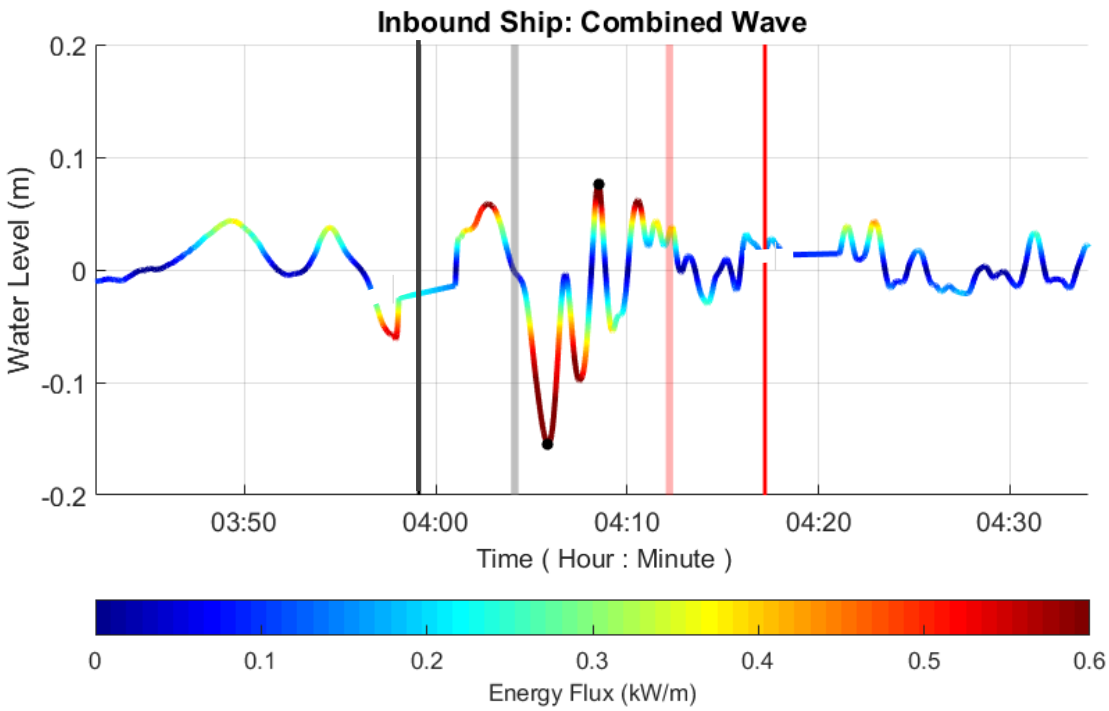

Figure 57: Water level and energy flux time series capturing the arrival at the South Channel Aquadopp site of the combined first and second waves from an inbound ship. The thick grey line indicates the predicted arrival time of the first wave, and the thick pale red line indicates the predicted arrival time of the second wave. The thin black and red lines bordering these two predictions mark the bounds between which the combined wave characteristics are measured. Solid dots mark the extreme water levels for the wave.

Figure 58 provides the histograms of the difference between the maximum and minimum water levels, (ΔZ) the maximum velocity magnitude fluctuation (v'), and the peak energy flux magnitude ($|E_f|$) for the first and second waves of outbound vessels, and the combined waves of inbound vessels. Comparing only the first and second waves of outbound vessels, it is observed that all three characteristics have very similar histograms. This is also reflected in the maximum water level difference, similar to a wave height, for the waves; the maximum difference for the first wave of an outbound ship is 0.25 m, the maximum difference for the second wave of an outbound ship is 0.28 m. Thus, because the second wave may be just as energetic as the first, the "doubling" effect of the South Channel being impacted by two similarly energetic waves from a single ship is significant.

A comparison of the water level change between the outbound and inbound histograms suggests that the fluctuation of the combined waves from an inbound ship tends to be slightly larger than the fluctuations of the individual waves produced by an outbound ship. Similarly, the velocity magnitude and peak energy flux histograms of the combined waves are shifted to slightly larger values compared to the individual waves of the outbound ships, meaning that the velocity fluctuations and energy flux also tend to be more significant for the combined waves. This is similarly reflected in the maximum difference for the combined waves of an inbound ship, 0.32 m, which is greater than the maximum values for the individual waves of the outbound ship waves.

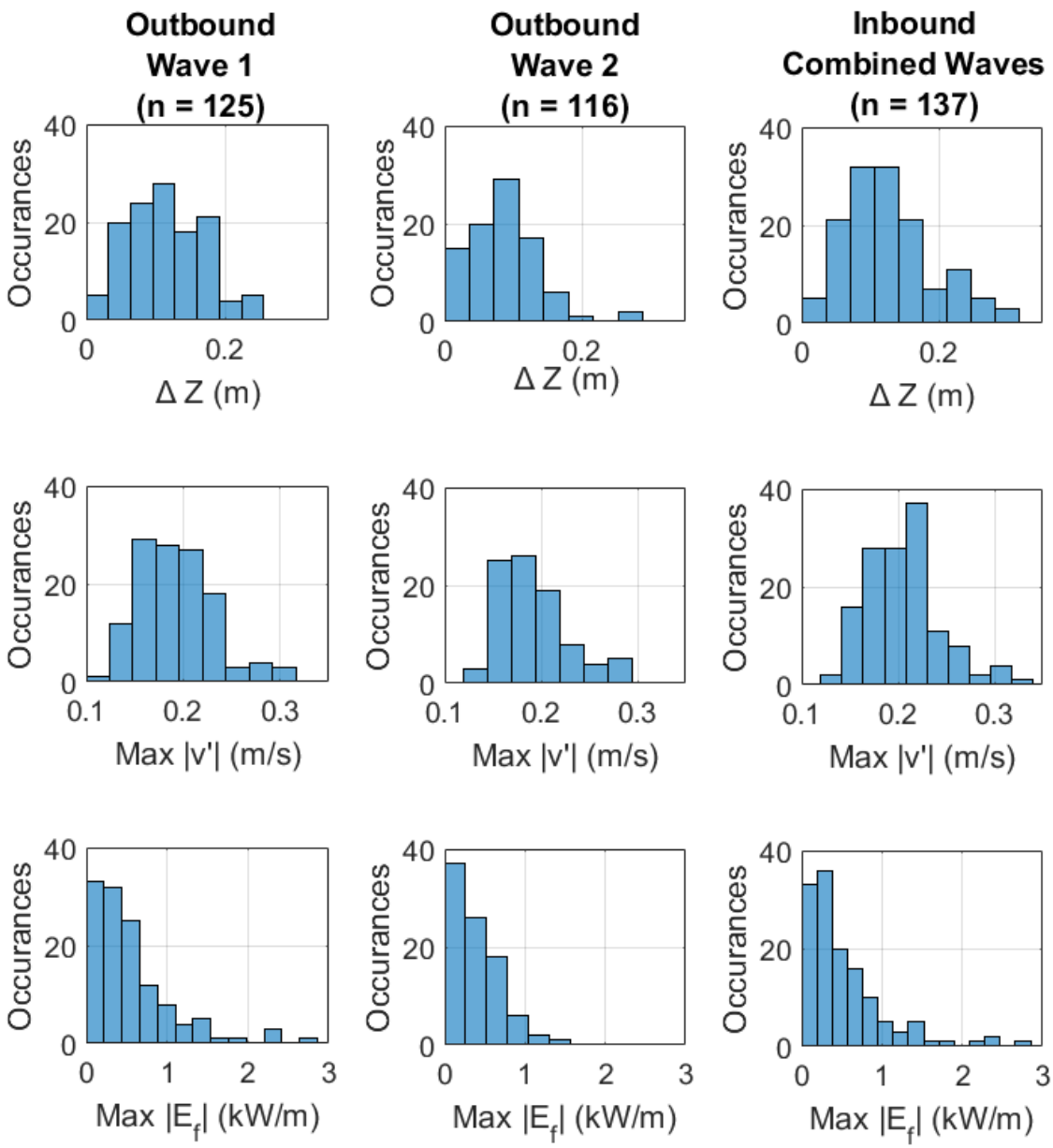

Figure 58: Histograms of (top) the difference between the maximum and minimum water levels, (middle) the maximum velocity magnitude fluctuation, and (bottom) the peak energy flux for the first and second waves of outbound ships (first and second columns) and the combined waves of inbound ships (third column) for ship wake measured in the Fall 2017 South Channel Aquadopp burst data.

3.7 Relative Shoreline Impact of Hydrodynamic Processes

Tidal currents, wind waves, and ship wake have been identified as significant characteristics of the hydrodynamics surrounding Bird-Long Island. Since the motivation of this study is the threat that erosion poses to the island, the following section estimates the potential of the three characteristics to cause erosion.

To do this, the mean energy flux contribution of currents, wind waves, and mid-band frequencies are calculated from the fall Aquadopp data at the Main Channel West and South Channel sites. Mid-band frequencies include hydrodynamic properties with lower frequencies than wind waves, but higher frequencies than tidal currents. This encompasses the energy from ship wake effects, as well as energy of similar frequencies that has been measured in the absence of ships; this energy is readily observed in the South Channel. The source of this additional mid-band energy has not been identified, but possible sources include seiching, wake interactions, and ship events not documented in the AIS data.

The daily rate is used to account for the different durations of the Aquadopp data collection at Main Channel West and South Channel. Due to battery failure, the Main Channel West deployment collected quality data for only three weeks of the four-week deployment.

The energy contributions are calculated at the Aquadopp and are reported as the energy per meter shoreline. The ratios of the contributions from currents, wind waves, and mid-band frequencies are assumed similar at the shoreline and instruments, but the values calculated at the instrument do not represent the actual energy at the shoreline. Thus, the energy at the instrument is used as a proxy for the energy at the shoreline,

which in turn indicates the potential for erosion.

A scarp impact threshold is used to reduce the total energy contributions to only that which may directly erode the scarp undergoing erosion. This threshold is simply the water level, as measured by the instruments, at which the water at the shoreline reaches the eroding scarp. The threshold for Main Channel West is 1.2 m mean tidal level, which typically corresponds to a spring tide. The eroding scarp at the South Channel is continuously exposed to the water; thus, there is no scarp impact threshold at the South Channel. At Main Channel West, processes that occur in water levels below the threshold, such as ship wake dissipating on the sandy beach, do not contribute to the erosive potential of that particular process or event. Conversely, processes occurring above this threshold are considered to have "scarp impact."

3.7.1 Energy Contribution from Currents

The energy of tidal currents is calculated from the profiling velocity and water level data measured by the Aquadopps. The profiling deployment parameters are provided in Table 2 of *METHODS.* The velocities are depth-averaged and low-pass filtered with a three hour cutoff to eliminate the effects of wind waves and ship wake. The current energy flux, $E_{f,c}$, is calculated by

$$E_{f,c} = \frac{1}{2}\rho V^3 h$$

where ρ is water density, V is depth-averaged velocity, and h is depth. The magnitude of the energy flux time series is integrated over the duration of the deployment to give the total energy contribution of currents during the deployment. For calculations pertaining to the Main Channel West site, this integration is performed only when the water level

exceeds the scarp impact threshold. Finally, the total is divided by the duration of the deployment to give a mean daily rate, $\bar{E}_{f,c}$. The total energy contribution of currents at Main Channel West is 6.40 MJ/m/day with 0.0560 MJ/m/day of this impacting the scarp, and the contribution at the South Channel is 3.17 MJ/m/day.

Figure 59 illustrates the reason for the disparity in the current contributions with scarp impact at the two sites. The scarp impact threshold for erosive potential at Main Channel West is only reached at spring tides. The water level peaks of neap tides are less than one meter, eliminating the effect of tidal currents on the Main Channel West scarp for much of the tidal cycle. In contrast, the eroding scarp at the South Channel is exposed to the effect of currents continuously.

The relative phasing of the peak water level and peak current velocities is also highly relevant. This phasing is shown in the tidal stage-velocity diagrams provided in Figure 28 in subsection 3.1.2. At Main Channel West, the maximum currents occur well below high tide, and the currents at high tide are very weak, as indicated by the low energy flux values; during the limited periods of the tidal cycle when the current reaches the scarp, the current is weak, and thus its energy flux is low. In the South Channel, tidal currents peak at high and low tide. While there is no scarp impact threshold here to consider, energy flux scales with depth, so at high tide, strong currents are combined with high water levels to produce comparatively high energy flux values in the South Channel. At low tide, the effect of the stronger currents is dominated by the low water level, resulting in a low energy flux.

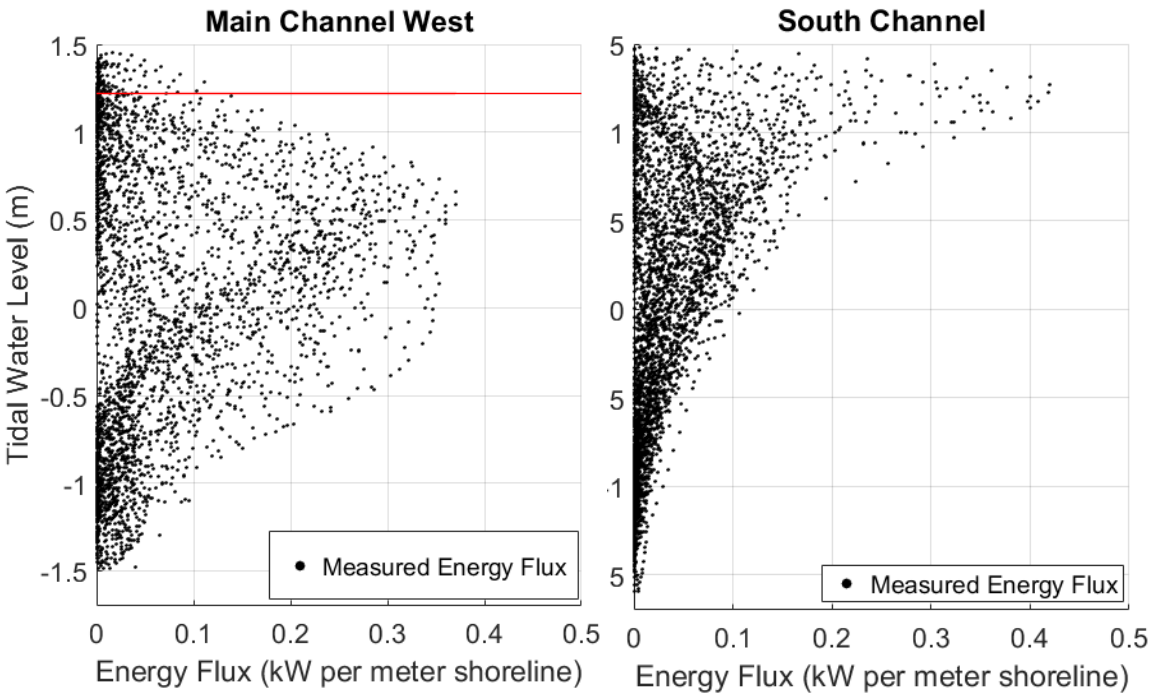

Figure 59: Comparison of measured current energy flux values over the tidal cycle at the (left) Main Channel West and (right) South Channel Aquadopp deployment sites.

3.7.2 Energy Contribution from Wind Waves

Wind waves are evaluated using the 17-minute Aquadopp wave bursts, which are measured at 1 Hz. For each burst, the peak frequency and significant wave height are calculated from the portion of the wave frequency spectrum above 1/6 Hz. The 1/6 Hz frequency limits the analysis to the range of frequencies in which wind waves are observed. From this data, the wave energy flux per meter shoreline, $E_{f,w}$, is approximated by representing the wave field by a single wave frequency calculated as

$$E_{f,w} = (\frac{1}{8}\rho g {H_{mo}}^2)(C_g)$$

where ρ is water density, g is gravitational acceleration, H_{mo} is significant wave height, and C_g is wave group velocity for the peak frequency. The energy flux time series is

integrated over time to get the total energy; at Main Channel West, the integration is performed only over times when water levels exceed the Scarp Impact Threshold. Finally, the daily rate, $\bar{E}_{f,w}$ is calculated by dividing the total energy by the duration of each deployment. The energy contribution of wind waves with scarp impact is 0.24 MJ/m/day at the Main Channel West site and 0.070 MJ/m/day at the South Channel site. For reference, the total energy contribution at Main Channel West from the wind waves, disregarding the Scarp Impact Threshold, is 1.9 MJ/m/day.

As with the current energy contributions, the scarp impact threshold significantly limits the impact of wind waves on the eroding scarp at Main Channel West, as demonstrated by the time series in Figure 60. Again, the energy flux with scarp impact is constrained to time periods at the peak of spring tides. Figure 61 provides the time series of energy flux in the South Channel, where there is no scarp impact threshold.

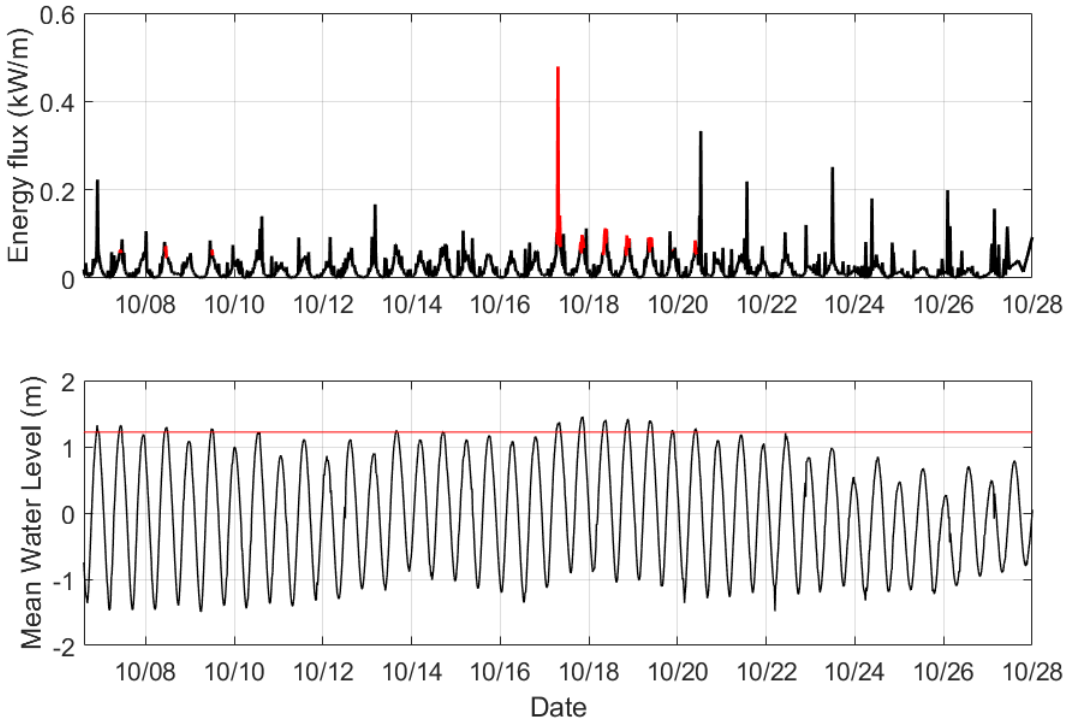

Figure 60: (Upper) Time series of the fall Main Channel West wind wave energy flux and (lower) mean water level with the 1.2 m Scarp Impact Threshold. The region surrounding Bird-Long Island is largely sheltered from waves

propagating from the open ocean, and the fetch of the river over which waves may grow is too short for the development of very large waves. Because waves tend to be smaller in the South Channel than in the Main Channel (Figures 34 and 35), the South Channel wind wave energy flux is smaller than the Main Channel wind wave energy flux. Note that the vertical axes in Figure 60 and 61 differ by about a factor of ten.

It is important to note that no major storm events occurred during the deployment, and the impact of wind waves would be much larger in storm conditions than in those measured. Storm surge raises the water level such that the scarp impact threshold is more likely to be exceeded, and stronger winds produce larger waves.

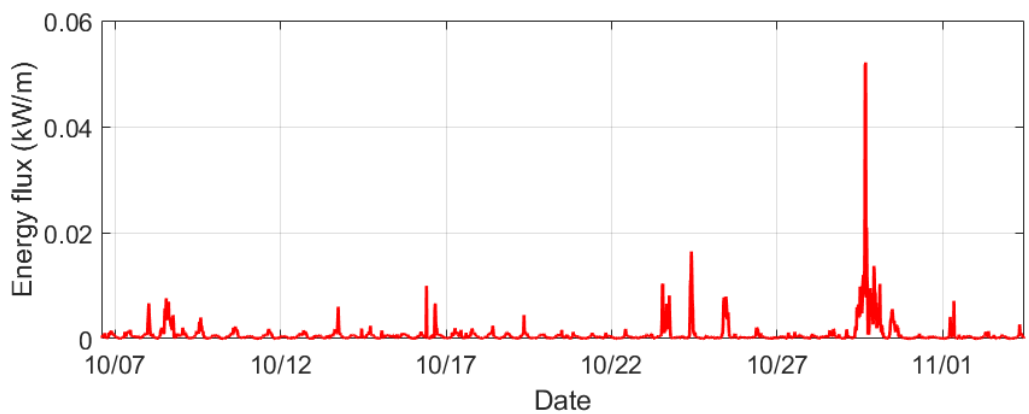

Figure 61: Time series of the fall South Channel wind wave energy flux.

3.7.3 Energy Contribution from Mid-Band Frequencies

Energy in the mid-band frequencies is calculated from the Aquadopp burst data in the same manner as that described in the *Ship Wake* section above. However, here, analysis is performed for the entirety of all bursts rather than only the initial wave of known wake events. Thus, a time series of $E_{f,MB}$ is determined for all burst data from the Aquadopp deployment.

As with the other processes, this energy flux is integrated over time to get the total

energy in the duration of the deployment. For the Main Channel West site, the scarp impact threshold is applied such that energy flux when instantaneous water levels are below 1.22 m does not contribute to the energy with scarp impact. This does not require that the mean water level exceed the scarp impact threshold; many events observed in the mid-band frequencies temporarily raise water levels significantly above the mean water level.

The energy contribution of the mid-band frequencies with scarp impact is 0.628 MJ/m/day at the Main Channel West site and 5.049 MJ/m/day at the South Channel site. For reference, the total energy contribution at Main Channel West from the mid band frequencies, disregarding the Scarp Impact Threshold, is 15.883 MJ/m/day. Because the energy flux is integrated over each burst, these values represent only 85% of the deployment duration, and are thus underestimating the total mid-band frequency energy.

Figure 62 shows the time series of the mid-band frequency energy flux for both the Main Channel West site and the South Channel site. Note that the vertical axes have different scales; the peaks in mid-band frequency energy flux at Main Channel West are much greater than those at the South Channel site. This is because the dominant contributor to mid-band frequency energy is ship wake, and the Main Channel West site is directly exposed to the shipping channel, whereas the South Channel site is sheltered by Bird-Long Island.

Figure 62 also demonstrates that the energy flux with scarp impact at Main Channel West is less dependent on high spring tide conditions than is the energy flux of the currents and wind waves. This is because ship wake events can significantly raise water levels temporarily, particularly in the surge, so the Scarp Impact Threshold may be

crossed even when mean water levels are below it.

Figure 63 (upper) also demonstrates that the increase in water level at the Main Channel West site during ship wake events. The data points which fall along lines or looping paths are the result of ship wake events, and lines with an upward trend indicate an increasing water level during the event. Figure 63 (lower) shows that the South Channel site does not experience as significant a change in water level in mid-band frequency events, as indicated by the more horizontal patterning of the data points.

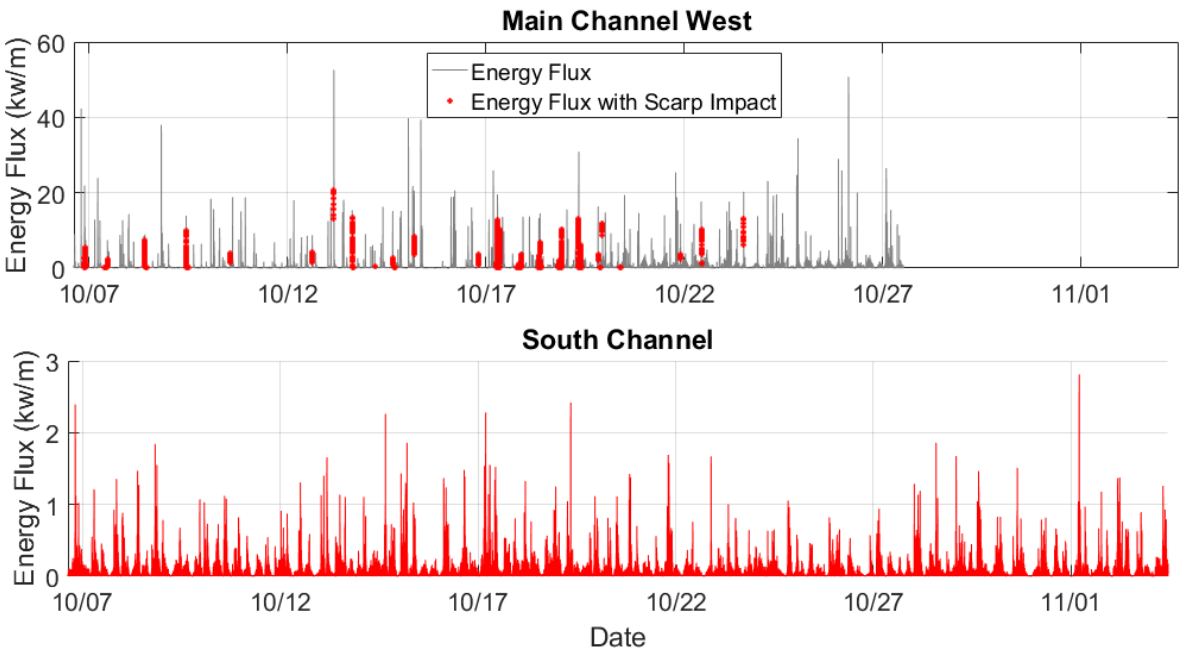

Figure 62: Time series of the fall (upper) Main Channel West and (lower) South Channel mid-band frequency energy flux with red data points indicating energy flux with scarp impact. Note the different scales of the vertical axes.

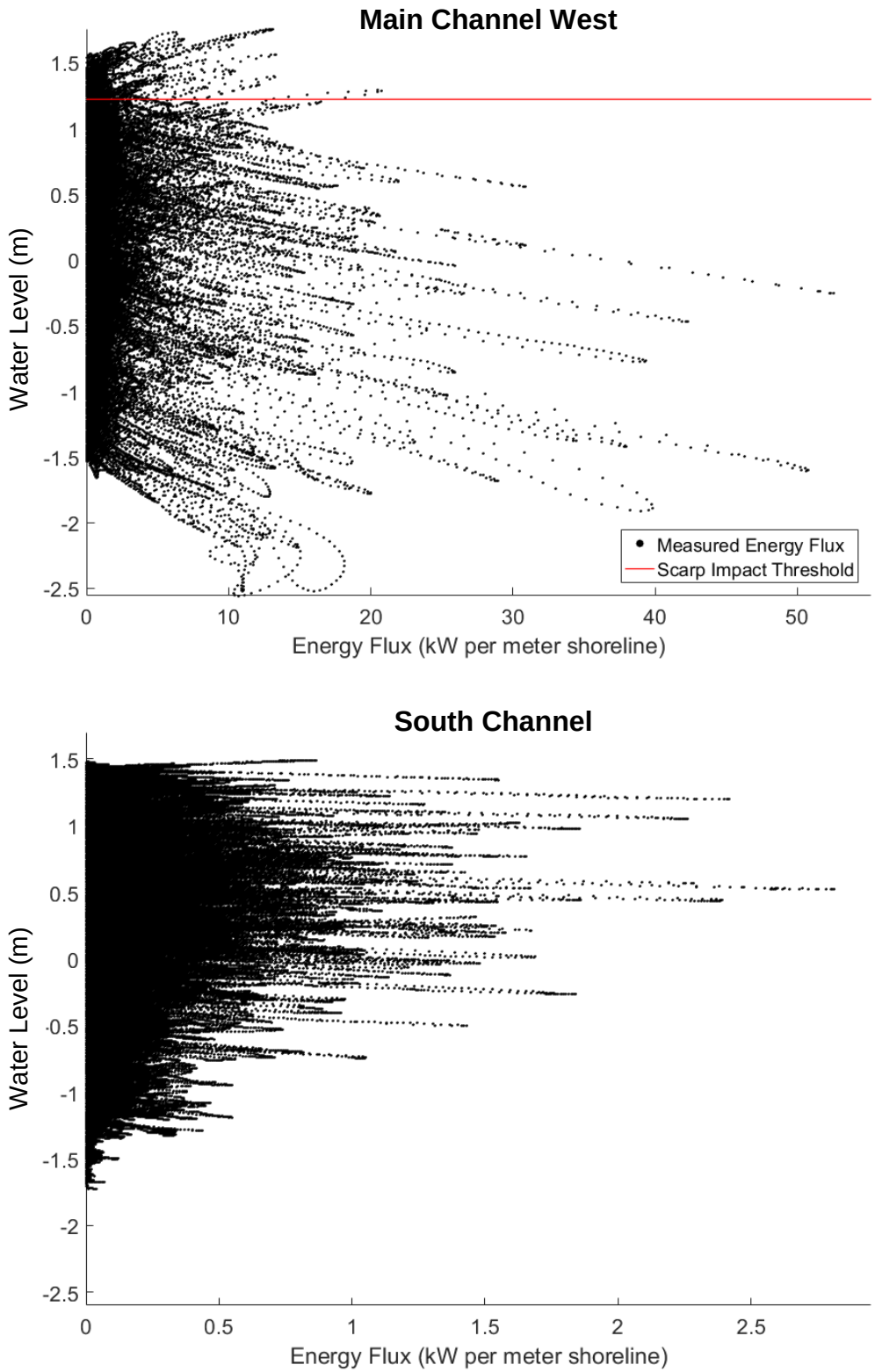

Figure 63: Comparison of measured mid-band frequency energy flux values over the tidal cycle at the (upper) Main Channel West and (lower) South Channel sites.

3.7.4 Summary of Energy Contributions

Figure 64 demonstrates the relative energy contributions of currents, wind waves, and mid-band frequencies at the two sites. At the Main Channel West site, mid-band frequencies are the dominant contributor to total energy, accounting for about 66% of the total energy. They are also significant in the distribution of energy with impact, accounting for an estimated 68% of the energy impacting the scarp. This is because the significant of currents lessens when the scarp impact threshold is applied due to the weak currents at high tide. At the South Channel site, where the scarp is continuously exposed such that all energy has a potential impact on the scarp, mid-band frequencies are the dominant contributor at an estimated 61%. Currents are also significant given the presence of strong currents at high tide, contributing about 38% of the energy at the site. As the energy measured at the Aquadopp is only a proxy for impacts at the scarp, the estimated relative contributions are more important than the actual energy values.

The dominance of mid-band frequencies in the energy contributions suggests that this energy source is greatly contributing to the observed erosion. It may be an even greater contributor than this analysis suggests due to the fact that the mid-band frequency energy source was the only source for which the estimate it known to be underestimated; the Aquadopp was in burst mode for 85% of the deployment, so no mid-band frequency energy estimates are available for 15% of the deployment duration.

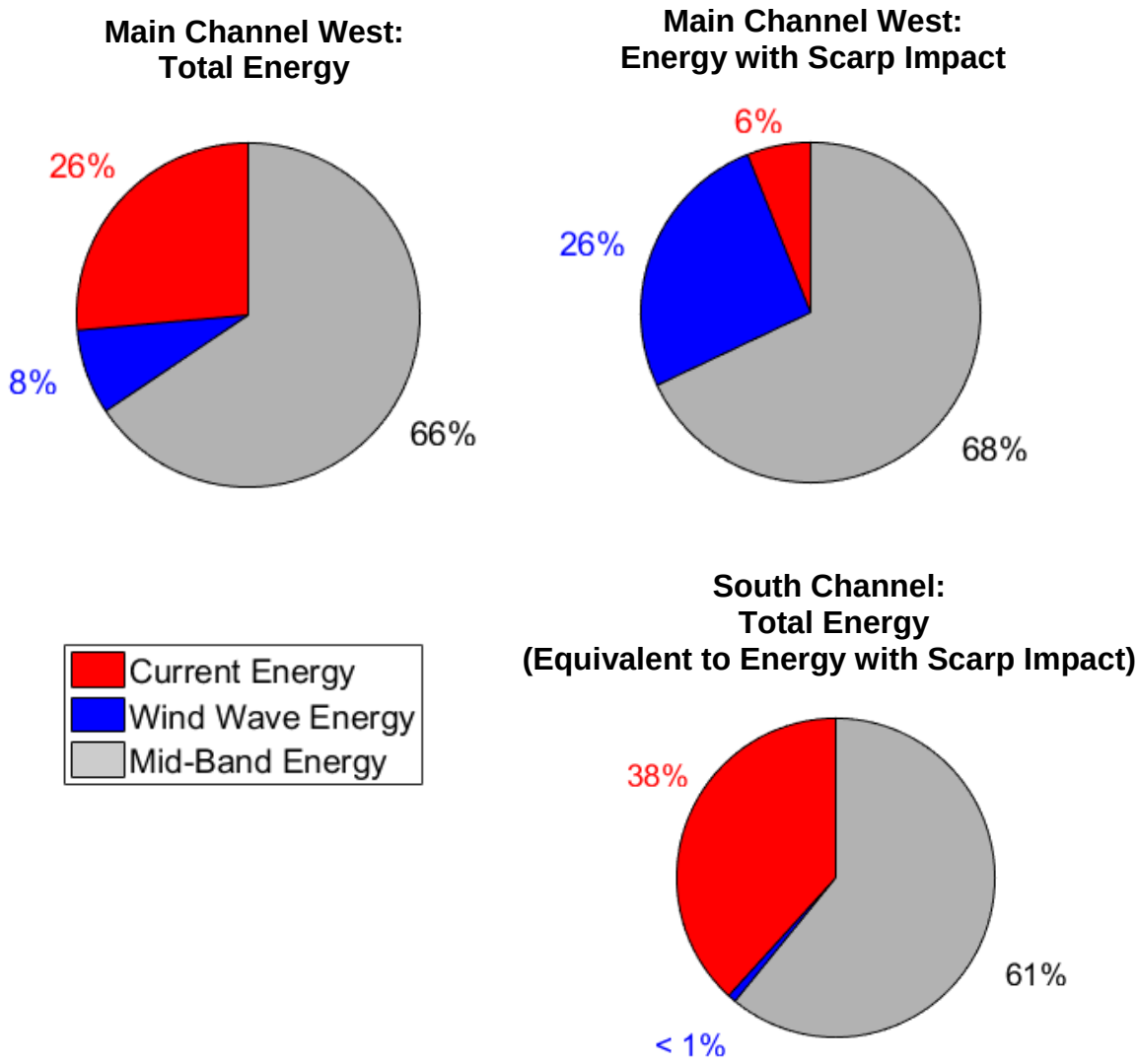

Figure 64: Relative contributions from currents, wind waves, and mid-band frequencies to (upper left) the total energy at Main Channel West, (upper right) the energy with scarp impacts at Main Channel West, and (lower right) the energy with scarp impacts at the South Channel Site. Because the scarp at the South Channel site is continuously exposed to hydrodynamic processes, all energy at that site has potential scarp impact.

3.7.5 Comparison of Mid-Band Energy to Large Vessel Initial Wave Energy

Ship wake is the primary contributor to energy in the mid-band frequencies, and the energy contribution of the initial wave in large vessel wake at the Main Channel West can be estimated from wake events that were well-captured in the Aquadopp bursts. The mean energy in the initial wave of the 176 large vessel wakes analyzed is 511.6 kJ per meter shoreline. According to the AIS data, there were 281 containership passages during the fall Aquadopp deployment at Main Channel West, prior to battery failure. Multiplying the mean initial wave energy by the 281 containership passages, it is estimated that the initial wave of containerships contributed 143.8 MJ/m of energy, or 6.65 MJ/m/day, from the initial wave alone. This is less than the estimate of 15.9 MJ/m/day from the full Aquadopp time series analysis of mid-band frequencies, but there are several factors contributing to this. First, the estimate based on the initial wave energy value only represents the first wave in a series of many waves in the wake, and it does not account for seiching, which may persist for over an hour. Also, through comparison with other sources of AIS data, it has been recognized that occasionally vessel passages, including containerships, are missing from the Marine Cadastre dataset. In addition, other vessels including fast moving recreational boats may also contribute to the energy. Lastly, the initial wave analysis was limited to events that were clearly identifiable in the water level time series and well separated from the wake of previous ships; interactions between the wakes of different ships are nonlinear, and interactions may increase the total energy in the wakes. For these reasons, the AIS-based initial wave energy analysis supports results of the mid-band Aquadopp data analysis.

4. CONCLUSIONS

Field measurements of hydrodynamic conditions in the vicinity of Bird-Long Island were obtained and analyzed to characterize the hydrodynamic processes which may be contributing to erosion. In addition, numerical models for the tidal and wind driven circulation and wind waves were applied for the region.

Numerical model simulations of both tidal effects and wind waves generally agreed with measurements. In both measurements and the model, wind waves are smaller in the South Channel than in the Main Channel, and wind events are associated with increases in wind waves that matched observations reasonably well. Spikes in water level and velocities that were not captured are largely attributed to ship wake, which is not included in the model. Large storm events were neither measured nor modeled.

Ship wake was found to be an important aspect of the hydrodynamics, and additional field data beyond that originally planned was collected to develop a better understanding of its potential significance to erosion along both the Main Channel and South Channel shores of Bird-Long Island. From this additional data, it was determined the ship wake from containerships, cargo ships, and tankers propagates into the South Channel behind Bird-Long Island from both the eastern and western ends of the island. Thus, for every vessel passing by the island, two waves are produced in the South Channel; they propagate in opposite directions and carry comparable energy.

The energy corresponding to the currents, wind waves, and mid band frequencies was calculated at two deployment sites, one along the Main Channel and one along the South Channel, to serve as a proxy for the potential of these processes to contribute to erosion at the shoreline. A vertical scarp impact threshold was used to isolate the energy

contributions measured when the water level is sufficiently high to impact the eroding scarp. At both sites, mid band frequencies were the dominant energy contribution, and much of the energy in these frequencies originates from ship wake and the seiching it induces. Wind waves are not negligible, but the island is well-sheltered from large waves propagating from the open ocean, and the small fetch surrounding the island prevents the local generation of large waves which directly impact the shoreline. The wind waves are more significant to the overall energy in the Main Channel than in the South Channel; this is in part due to their larger size in the Main Channel, but it is also a result of the relative role of tidal currents. In the Main Channel, tidal currents are slow at high tide, when water levels reach the scarp, so their impact on the scarp is minimal. However, in the South Channel, the scarp is vulnerable at all tidal stages, and currents are fast at high tide, so currents are proportionally more important in the South Channel than in the Main Channel.

It is important to note that storm events can have significant impacts on the shoreline. Storm surge raises water levels while winds increase wave height such that the scarp is more vulnerable to wave attack. Unfortunately, the observational time periods were calmer than historical norms and no significant storm events were captured; therefore, large wave events are not directly accounted for in this study. In addition, the measurements of the wave field with a seabed mounted pressure transducer tend to under estimate the wave field due to wave attenuation. However, this is somewhat mitigated by the single wave approximation for the computation of the energy flux, which can overestimate the total energy flux by a factor of two. Therefore, the overall estimate of the relative importance of the wave energy contribution is reasonable, and the

approximations made do not change the conclusions of the energy analysis.

AIS data was utilized to confirm ship wake events and ultimately pair measured ship wakes with characteristics of vessels from which they were generated. This permitted analysis of known ship wake features, but theoretical relationships for idealized scenarios between these features and ship characteristics did not correlate significantly with the observed data. This implies that the complexities of the site, such as bathymetric features and tidal behavior, likely play a role dictating the size and energy of ship wake that is not yet well understood. Additional observations and high level computational fluid dynamic modeling of the ship wake will be required to determine the relationship between the ship characteristics, the hydrodynamic conditions, and the resulting wake.

Ship wake is a persistent source of energy along the shoreline of Bird-Long Island, and the energy contribution proxy suggests it is a source of erosion for both the Main Channel shoreline and the South Channel shoreline. Because two waves propagate into the South Channel from each ship passage, it is expected that closing the blowout at the eastern end of the island would prevent one of the waves from reaching the South Channel shoreline. This could eliminate a portion of the energy associated with the wake from reaching that shoreline, and thus lessen the impact of ship wake on the eroding scarp along the South Channel shoreline, including that near the archaeological site. However, this would not necessarily decrease the erosion capacity of the currents and the impacts of this scenario on the general circulation would need to be further evaluated.

REFERENCES

Booij, N., Ris, R., and Holthuijsen, L. H. “A third-generation wave model for coastal regions: 1. model description and validation.” Journal of Geophysical Research: Oceans (1978-2012), 104(C4):7649-7666, 1999.

Houser, C. "Relative importance of vessel-generated and wind waves to salt marsh erosion in a restricted fetch environment." Journal of Coastal Research (2010): 230-240.

Pawlowicz, R., Beardsley, B., and Lentz, S. "Classical tidal harmonic analysis including error estimates in MATLAB using T_TIDE", Computers and Geosciences 28 (2002), 929-937.